Syracuse University

SURFACE

Dissertations - ALL   SURFACE

August 2018

MOLECULAR DYNAMICS STUDY ON THE STRUCTURE, DYNAMICS AND STRESS RESPONSE OF DILUTE MICELLAR SYSTEMS IN UNIAXIAL EXTENSIONAL DEFORMATION

Kelechi Okoroafor
Syracuse University

Follow this and additional works at: https://surface.syr.edu/etd

 Part of the Engineering Commons

ABSTRACT

Micellar structures have been proposed for potential application in hydrotropy, biomimetics, dispersion and emulsification, enhanced oil recovery, detergency, templating, drug delivery, personal care products, drag reduction, nanoscale reaction vessels, therapeutic gene delivery, bio-catalysis and so on. Though several studies exist, there still remains a gap in the current knowledge on structural response of single micelles in solution to uniaxial extensional flow deformation. These knowledge gaps are possibly due to the inability of traditional experimental studies to investigate micellar properties at the time- and length-scale pertinent to self-assembly and micellar dynamics. To this end, this work aims to utilise coarse-grained molecular dynamics simulations to investigate the dynamics and structural response of various infinitely dilute micellar solutions under the influence of uniaxial extensional flow.

Spherical vesicles formed from hexacosanoate anion and octyltrimethylammonium cation; rod-like and worm-like micelles formed from hexacosanoate and palmitate anions; and branched worm-like micelles formed from cetyltrimethylammonium cation and sodium salicylate anion have been parametrised according to the Martini force field formalism. These structures were simulated in equilibrium; under uniaxial extensional flow; and in cessation of uniaxial

extensional flow. Changes in micellar structure in uniaxial extensional flow and subsequent stress responses are presented for each micellar system at varying deformation rates. It is observed that structural changes and stress response are dependent on micellar stress relaxation ability whilst undergoing uniaxial deformation. The nature and varying influence of stress relaxation as a function of deformation rate is studied for each structure. Deformation of these structures in a direction normal to their principal orientation is also investigated. It is shown that orientation has a short-term effect on the dynamics and structural evolution of non-isotropic micellar structures. Finally, structural and stress responses following cessation of uniaxial extensional flow are presented.

MOLECULAR DYNAMICS STUDY ON THE STRUCTURE, DYNAMICS AND STRESS RESPONSE OF DILUTE MICELLAR SYSTEMS IN UNIAXIAL EXTENSIONAL DEFORMATION

By

Kelechi Okoroafor

B.S., Federal Unitech, 2010

M.S., University of Pennsylvania, 2014

DISSERTATION

Submitted in partial fulfillment of the requirements for the

degree of Doctor of Philosophy in Chemical Engineering

Syracuse University

August 2018

ACKNOWLEDGEMENTS

Contents

List of Figures

List of Tables

Chapter 1

Introduction

1.1 Micellar Formation

Surfactants are surface active molecules that promote miscibility and reduce excess energy at interfaces of otherwise immiscible fluids.[1–11] They are characterised by solvophilic and solvophobic moieties that spontaneously self-assemble at a surfactant-specific concentration, called the critical micellar concentration, into structures that are generally called micelles. This self-assembly process is entropically driven and aimed at mitigating unfavourable solvent-solvophobic interactions, while simultaneously minimizing steric and/or electrostatic intra-micellar repulsions.

Micellar structures consist of a solvophobic core and a solvophilic crown that encompasses the core. In aqueous/polar solutions, micellar structures are typically characterised by non-ionic, cationic, anionic, or zwitterionic hydrophilic/lipophobic crowns and hydrophobic/lipophilic cores. In apolar solutions, micellar structures, typically called reverse micelles, consist of lipophilic crowns and lipophobic cores. Micellar structures have found applications in hydrotropy, biomimetics, dispersion and emulsification, enhanced

oil recovery,[12] detergency, templating, drug delivery, personal care products, drag reduction,[13] nanoscale reaction vessels, therapeutic gene delivery, biocatalysis and so on.

Owing to their vast potential applications, self-assembled structures have been extensively studied to gain better understanding of their underlying physics and mechanisms. Based on these studies, it has been observed that aqueous solutions of micelles exist in dynamic equilibrium of constant surfactant exchange between the bulk solvent and the self-assembled structure. Furthermore, micellar morphology has been found to be particularly susceptible to the chemical characteristics of the bulk fluid. Conditions such as pH, presence of electrolytes, temperature, pressure, concentration, presence of counter-ion surfactants, presence of nano-particles have been seen to affect the formation, and transition of micellar structures. Interestingly, geometric arguments have resulted in a concept called the critical molecular packing parameter[14–16]

$$S = \frac{v}{a_0 l_c},$$ (1.1)

where a_0 is the equilibrium head group area that is obtained from thermodynamic considerations, while v, l_c are the volume and length of solvophobic core respectively. They are empirically estimated to be a function of the number of carbon atoms n_c in the most common surfactants in aqueous

solution:

$$l_c \approx \left(1.54 + 1.265 n_c \right) \text{Å}, \tag{1.2}$$

$$v \approx \left(27.4 + 26.9 n_c \right) \text{Å}. \tag{1.3}$$

Consider a spherical aggregate of radius R made up of g molecules. The volume V and surface area S of the core are:

$$V = gv = \frac{4}{3}\pi R^3, \tag{1.4}$$

$$A = ga_0 = 4\pi R^2. \tag{1.5}$$

Dividing the aggregate volume by its surface area gives:

$$\frac{V}{A} = \frac{gv}{ga_0} = \frac{\frac{4}{3}\pi R^3}{4\pi R^2} = \frac{R}{3}. \tag{1.6}$$

This implies that $R = \frac{3v}{a_0}$. \tag{1.7}

Since the radius of the spherical core cannot exceed the length of the surfactant solvophobic group, this implies that:

$$l_c \leq \frac{3v}{a_0}, \tag{1.8}$$

$$\text{and } \frac{1}{3} \leq \frac{v}{a_0 l_c}. \tag{1.9}$$

Thus the range of critical packing parameter values where spherical aggregates are physically possible are

$$0 \le \frac{v}{a_0 l_c} \le \frac{1}{3}.$$

(1.10)

Consider a cylindrical aggregate of radius R and length L made up of g molecules. The volume V and surface area A of the core are:

$$V = gv = \pi R^2 L,$$

(1.11)

$$A = ga_0 = 2\pi RL.$$

(1.12)

Dividing the aggregate volume by its surface area gives:

$$\frac{V}{A} = \frac{gv}{ga_0} = \frac{\pi R^2 L}{2\pi RL} = \frac{R}{2}.$$

(1.13)

This implies that $R = \frac{2v}{a_0}$.

(1.14)

Since the radius of the cylindrical core cannot exceed the length of the surfactant solvophobic group, this implies that:

$$l_c \le \frac{2v}{a_0},$$

(1.15)

$$\text{and } \frac{1}{2} \le \frac{v}{a_0 l_c},$$

(1.16)

4

Thus the range of critical packing parameter values where cylindrical aggregates are physically possible are

$$\frac{1}{3} \leq \frac{v}{a_0 l_c} \leq \frac{1}{2}.$$ (1.17)

Using similar geometric considerations, the range of critical packing parameter values where bilayer aggregates are physically possible are

$$\frac{1}{2} \leq \frac{v}{a_0 l_c} \leq 1.$$ (1.18)

These findings are summarised in fig1.1.

Equilibrium head group area can be obtained from thermodynamic consideration of the free energy associated with transferring a surfactant molecule into a self-assembled structure from an infinitely dilute state[14–16]

$$\left(\frac{\Delta \mu_g^o}{k_b T}\right) = \left(\frac{\Delta \mu_g^o}{k_b T}\right)_{Transfer} + \left(\frac{\Delta \mu_g^o}{k_b T}\right)_{Interface} + \left(\frac{\Delta \mu_g^o}{k_b T}\right)_{Head}.$$ (1.19)

The first term on the RHS of eqn 1.19 represents a negative contribution to free energy resulting from the transfer of a solvophobic group from unfavourable interactions with the solvent. It is responsible for the micellization process and is a function of the surfactant solvophobic group but not a function of the self-assembled aggregate size. The second term on the RHS of
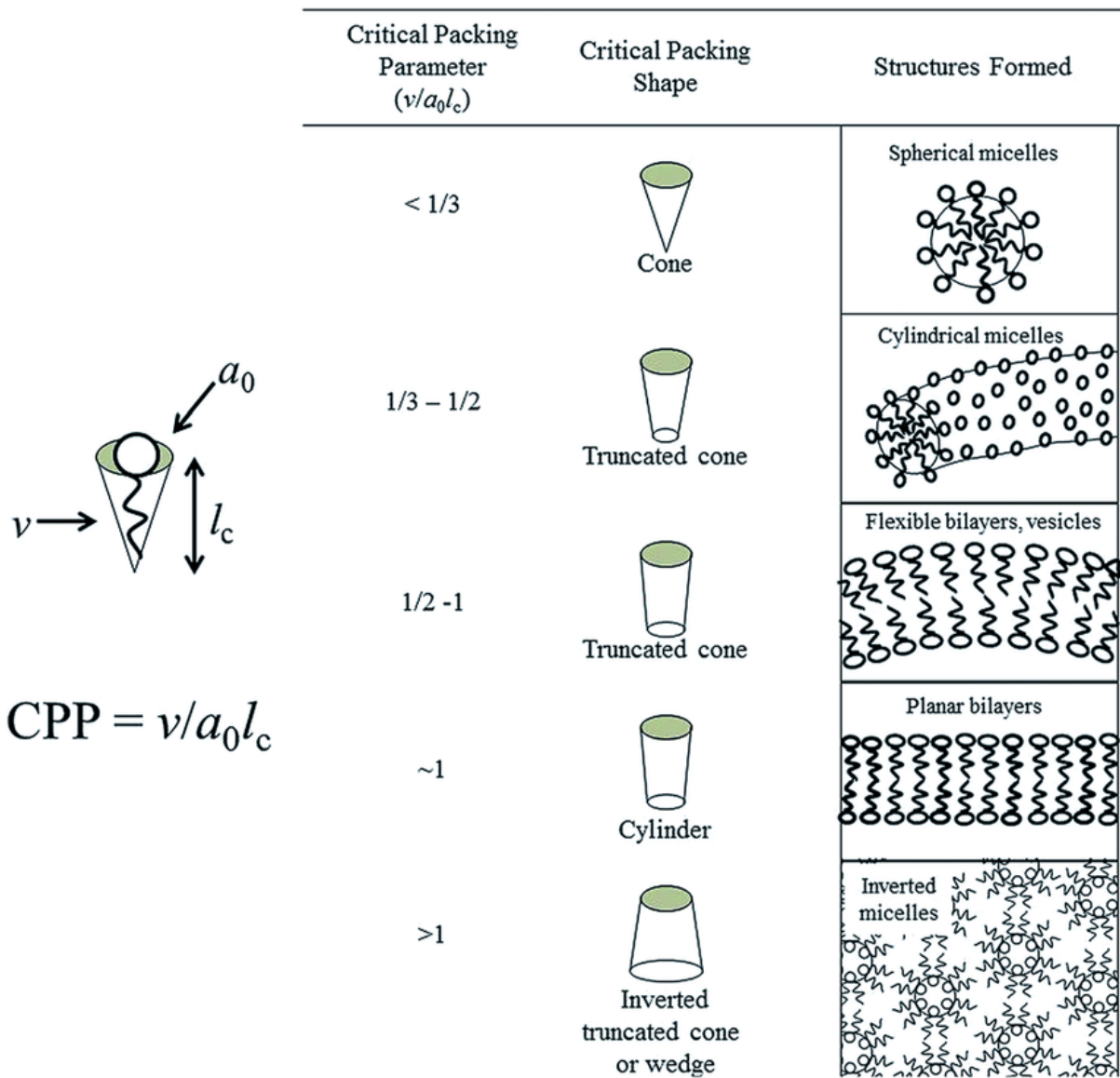
Figure 1.1: Packing parameter, molecular architecture, and predicted micellar morphology[1]

eqn 1.19 is a positive contribution to free energy resulting from residual interactions between solvophobic groups and the solvent. It is a function of the surface tension σ and the interfacial area per molecule a of the self-assembled aggregate. Thus it increases with the aggregate size. The third term on the RHS of eqn 1.19 is a positive contribution to the free energy that results from repulsive solvophilic groups at the crown of the self-assembled structure. It depends on the solvophilic group interaction parameter α and the inverse of interfacial area per molecule a of the self-assembled aggregate. Thus, this term increases as the aggregation number increases. This free energy model can be written as:

$$\left(\frac{\Delta\mu_g^o}{k_bT}\right) = \left(\frac{\Delta\mu_g^o}{k_bT}\right)_{Transfer} + \left(\frac{\sigma}{k_bT}\right)a + \left(\frac{\alpha}{k_bT}\right)\frac{1}{a}. \qquad (1.20)$$

Minimizing the free energy with respect to a gives:

$$\frac{\partial}{\partial a}\left(\frac{\Delta\mu_g^o}{k_bT}\right) = 0, \qquad (1.21)$$

$$\Rightarrow \left(\frac{\sigma}{k_bT}\right) - \left(\frac{\alpha}{k_bT}\right)\frac{1}{a^2} = 0, \qquad (1.22)$$

$$\Rightarrow a_0 = \left(\frac{\alpha}{\sigma}\right)^{\frac{1}{2}}. \qquad (1.23)$$

Based on this thermodynamic consideration, certain conclusions can be drawn about the micellization process. In aqueous solution of non-ionic surfactants,

small-sized hydrophilic group relative to hydrophobic group result in smaller α, smaller a_0, bigger S, which favours bilayer structures. On the other hand, larger hydrophilic group relative to hydrophobic group cause larger α, larger a_0, smaller S, and bias towards cylindrical or spherical structures. Furthermore, when ionic and non-ionic surfactants are compared, the interaction parameter α of ionic surfactants are expected to be larger because head groups of ionic surfactants have additional repulsion from electrostatic interactions. Thus, for the same chemical architecture, ionic surfactants may have smaller packing parameter and different micellar morphology than non-ionic surfactants. However, the addition of counter-ions to the bulk solution can screen the head-group electrostatic repulsion and result in smaller α, smaller a_0, and higher S. By so doing, the addition of counter-ions can cause structural transition from spherical to cylindrical micellar structures. Similar to counter-ions, the presence of organic solvents in the aqueous solutions results in lower interfacial tension σ, lower a_0, and lower S. Double-tailed surfactants will have higher S and favour bilayer structures compared with their single-tailed analogue.

1.2 Micellar Transition

At the onset, surfactant molecules exist as monomers in aqueous solution until the critical micellization concentration (CMC) is reached. At the CMC, surfactant molecules spontaneously self-assemble into micellar structures. For most common surfactants, the structures formed at CMC are globular. These globular structures exchange surfactant monomers with the bulk solution and can grow with increase in concentration and other such changes in the bulk solution.

However, globular micellar growth is limited by the physical constraint that the radius of the sphere must be less than or equal to the length of the hydrophobic tail. As such lateral micellar growth and consequent transition into cylindrical micelles occurs. Initially, cylindrical micelles tend to be short and rigid and these structures are typically called rod-like micelles (RLM). As the micelle grows and increases in length, the micellar contour length can exceed its persistence length; resulting in more flexible structures typically called worm-like micelles (WLMs).

WLMs bear close structural resemblance to polymer molecules. However, unlike polymer molecules, WLM exist in a dynamic equilibrium of scission and recombination, hence the name "living polymers". Due to their analogy to polymer molecules, several theories relating polymer kinetic, dynamics

and relaxation have been adapted for WLMs. One such example is the mean-field theory that has been adapted to proposed an exponential dependence of average length of WLM to the scission energy for non-ionic surfactants[17] and a log-normal dependence for ionic surfactants.[18] These results have also been replicated in molecular dynamics simulations.[11]

Micellar structures are particularly sensitive to the presence of counter-ions and electrolytes. As a result of adding electrolytes and/or counter-ions, spherical micelles can undergo transition to WLM, and WLM can undergo transition to branched worm-like micelles (BWLM) and other higher order structures. Additionally, the chemical architecture of the counter-ion also has significant impact on the resulting micellar morphology. For instance, between halide salts, Iodide was seen to promote more micellar growth than Bromine, which was itself similarly observed to promote more micellar growth than Chloride. This is due to the differing tendencies for these halide ions to hydrate in aqueous solution. Chloride has the highest tendency to hydrate and Iodide has the least tendency to hydrate amongst the three mentioned halide salts.[19] As a result of their relatively higher hydration tendency, Chloride ions tend to be located at the Stern layer of the micelles; making it less effective at intra-micellar charge screening. Iodide, on the other hand, tends to be located closer to the micellar crown, making it more effective at intra-micellar charge screening. The better intra-micellar

charge screening encourages micellar closer-packing that in turn encourages further micellar growth.

Organic salts have been observed to have a more drastic effect on micellar growth than halide salts. This has been attributed to the ability of aromatic salts to inter-digitate within the ionic surfactant micellar structure, enabling its interactions with interfacial water, the charged head group, and the apolar micellar core.[9,20] This inter-digitation results in more efficient charge screening, closer packing of the surfactants in the micelle, more significant micellar growth, and transition to higher order structures than are possible in halide salts.[19]

Beyond the formation of WLM, further micellar growth can occur through increase in the lateral length of the micelle or micellar branching. Given a concentration of ionic surfactant, as the concentration of the binding counter-ion is increased, micellar branching becomes more energetically favourable. This is because the end-caps of a WLM has higher energy than the contours. So the system can reduce the excess energy in the end-caps by fusing with another micelle in the system. The concentration beyond which branching occurs depends on the chemical architecture and concentration of the ionic surfactant, as well as the chemical architecture and concentration of the binding counter-ions in the systems. Surfactants with longer hydrophobic tails tend to form higher order structures more rapidly than others with

Figure 7. Zero shear viscosity $\eta(\infty,0)$ as a function of the NaSal concentration and as a function of the CPyCl concentration at $T = 20$ °C.

Figure 13. Stress relaxation time τ as a function of the surfactant concentration c_{CPyCl} and the salt concentration c_{NaSal} at $T = 20$ °C.
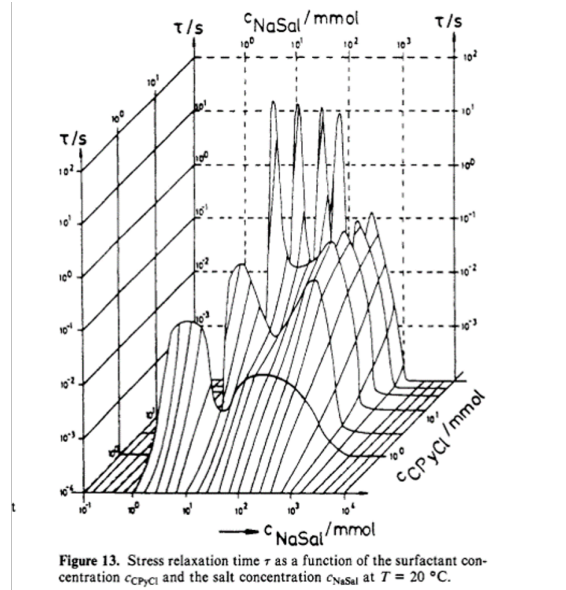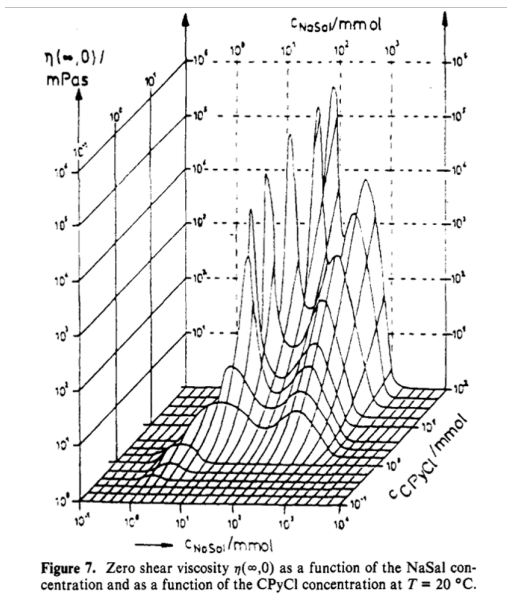
Figure 1.2: Viscosity and relaxation time cationic surfactant as a function of binding counter-ion[2]

shorter hydrophobic tail. Similarly, binding counter-ions with longer hydrophobic tails tend to form higher order structures than other with shorter or no hydrophobic tail.

These changes in structure have been known to cause drastic changes in rheological properties of the micellar solution. For instance, a non-monotonic dependence of viscosity and relaxation time on molar ratio of binding counter-ion has been experimentally observed as seen in fig1.2.[2,21] At the onset of the curve, the growth of viscosity with counter-ion concentration has been theorised to be due to micellar growth and transition from spherical micelles to worm-like micelles that causes up to 6 orders of magnitude increase in viscosity. After the first peak, the viscosity is seen to decrease and this has been related to the formation of branches along the micellar contour. This branch points have been found to slide along the contour length, thus intro-

ducing an addition stress release mechanism to the solution, unlike entangled worm-like micelles that relax via reptation and micellar scission.[22–25] As the counter-ion concentration is further increased, the branching in the solution increases and viscosity decreases until a second maximum in viscosity is observed. This second viscosity maximum is related to the formation of multi-connected network of micelles in the systems. These multi-connected networks of worm-like micelles are more fluid than worm-like micelles because the branches can still slide, but not as fluid as branched worm-like micelles. As concentration of counter-ions are further increases, the micelle becomes over-saturated with counter-ions such that it becomes entropically favourable for the micellar structure to disintegrate as the counter-ions act as a hydrotope that increases the solubility of the surfactant. This causes the eventual decrease in viscosity and relaxation time seen in fig1.2.

1.3 Modelling and Simulation of Soft Matter

Despite the tremendous progress in understanding the underlying mechanisms behind micellar dynamics and kinetics, experimental methods can be limited by their inability to probe, observe and quantify interactions in molecular systems with accuracy at the length and time scale of molecular processes. To this effect, several molecular dynamics simulation methods

have been developed to complement the insight obtained from experimental studies on molecular systems as shown in fig1.3.

Currently, the lowest level method of molecular modelling is the Ab Initio method where the chemical detail of each molecule is specified at the quantum level and sub-atomic particles are explicitly modelled. This model has the advantage of higher accuracy as fewer assumptions are made about the molecule. However, it has the disadvantage of high degree of freedom. Consequently, this method is typically used to model sub-atomic phenomena that happen on the length scale of angstroms and the time-scale of femtoseconds. All-Atom molecular modelling makes credible assumptions about the subatomic configuration and represents molecules with atomic specificity. Essentially, All-Atom model sacrifices subatomic specificity for increased simulation time- and length-scale as they can be used to model molecular systems on the order of nanometre and picoseconds. Further assumptions can be made about the atomic, and molecular details of systems such that modelling and simulation of even higher length- and time-scales are possible. These are achieved in coarse-grained, meso-scale and continuum dynamics.

Coarse-grained molecular modelling has been very useful in studying micellar structure and interactions. In particular, the Martini Forcefield formalism[76] has been particularly useful in modelling surfactant solutions. In this particle

14
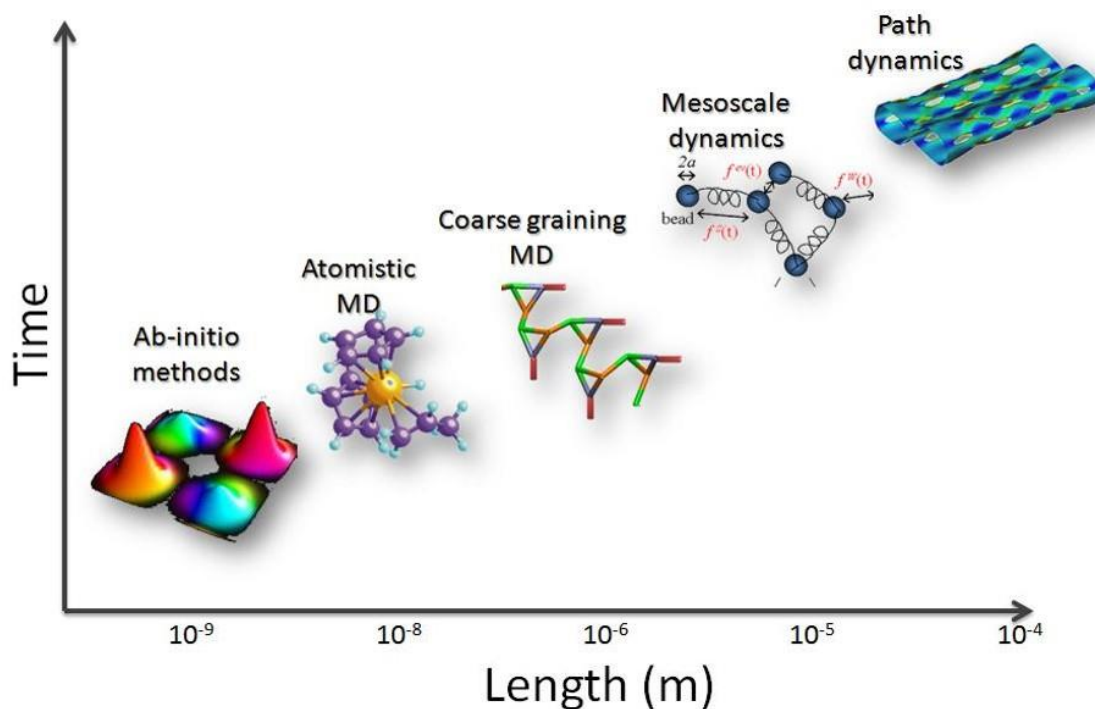
Figure 1.3: Hierarchy of molecular modelling and simulation methods

description, 4 big atoms are lumped together to form a particle that may or may not be bonded to other particles in the system. Under the Martini formalism, particles are generally categorised into 4 types: polar P, apolar C, intermediate N, and charged Q and each type is categorised into subtypes as shown in table 1.1.

Table 1.1: Martini particle definitions.

Type	Sub-type	Description
P	1, 2, 3, 4, 5	Polar beads. 1 is least polar, 5 is most polar

Type	Sub-type	Description
		Continuation of Table 1.1
C	1, 2, 3, 4, 5	Apolar beads. 1 is least polar, 5 is most polar
N	0, d, a, ad	Intermediate beads. 0 has no hydrogen bond forming capacity, d is hydrogen donor, a is hydrogen acceptor, da is hydrogen donor or acceptor
Q	0, d, a, ad	Charged beads. 0 has no hydrogen bond forming capacity, d is hydrogen donor, a is hydrogen acceptor, da is hydrogen donor or acceptor

In the Martini formalism, bonds are modelled using harmonic potential as in eqn 1.24; angles are modelled using harmonic potential as in eqn 1.25; pairwise interactions are modelled using Lennard Jones potential as in eqn 1.26; and electrostatic interactions are modelled using Coulombic interactions as

in eqn 1.27. Specifically,

$$V_{bond}(b) = \frac{1}{2}K_b\left(b - b_0\right)^2, \tag{1.24}$$

$$V_{angle}(\theta) = \frac{1}{2}K_\theta\left(\cos(\theta) - \cos(\theta_0)\right)^2, \tag{1.25}$$

$$V_{LJ}(r_{ij}) = 4\epsilon_{ij}\left[\left(\frac{\sigma_{ij}}{r_{ij}}\right)^{12} - \left(\frac{\sigma_{ij}}{r_{ij}}\right)^6\right], \tag{1.26}$$

$$\text{and } V_{Coulomb}(b) = \frac{q_i q_j}{4\pi\epsilon_0 r}, \tag{1.27}$$

where b is bond distance; b_0 is the equilibrium bond distance; K_b is the equilibrium bond force constant; θ is bond angle; θ_0 is equilibrium bond angle; K_θ is equilibrium angle force constant; ϵ_{ij} is the energy minima of interacting pair i and j; σ_{ij} is the spatial separation distance of the energy minima of interacting pair i and j; r_{ij} is the separation distance between interacting pair i and j; $q_{i,j}$ is the charge of interacting particle i or j.

1.4 Uniaxial Extensional Deformation

In uniaxial extensional deformation, a simulation box is stretched at predefined deformation rate in one direction and compressed in the other orthogonal directions, while keeping the simulation box orthogonal. The applied

deformation tensor $\underline{\underline{S}}$ is

$$\underline{\underline{S}} = \frac{1}{2}\left[\underline{\nabla}\,\underline{v} + \left(\underline{\nabla}\,\underline{v}\right)^t\right] = \begin{bmatrix} \dot{\varepsilon} & 0 & 0 \\ 0 & -\frac{\dot{\varepsilon}}{2} & 0 \\ 0 & 0 & -\frac{\dot{\varepsilon}}{2} \end{bmatrix}. \tag{1.28}$$

The resulting flow field is:

$$v_i = \dot{\varepsilon}t, \tag{1.29}$$

$$v_j = -\frac{\dot{\varepsilon}}{2}t, \tag{1.30}$$

$$v_k = -\frac{\dot{\varepsilon}}{2}t. \tag{1.31}$$

where v_i is the velocity in the direction of extension, while v_j and v_k are the velocities in the direction of compression. These simulations are conducted such that the divergence of velocity is zero, i.e. $\nabla \cdot v = 0$, and the mass in the system is conserved.

Rheological studies typically quantify deformation rate with respect to the non-dimensional Weissenberg number (Wi)

$$Wi \equiv \lambda\dot{\epsilon}, \tag{1.32}$$

where $\lambda =$ longest relaxation time; $\dot{\epsilon} =$ deformation rate. The longest relax-

ation time of a self-assembled structure can be calculated using the autocor-relation function of an intrinsic structural property e.g. orientation, centre of mass etc..

Interesting results obtained from these simulations include pair, bond, angle, and total potential energy and coordinates. Bond and angle potential energy are the potential energy stored in the bonds of the particles due to the bond distance and bond angle respectively. Pair potential energy is the potential energy resulting from the interaction of non-bonded pairs. The total potential energy is the sum of the pair, bond and pair potential energies. From these results, other important characteristics can be computed. Stress can be computed from the total potential energy per unit volume. Elastic modulus can be calculated as the stress per unit strain within the elastic deformation regime. The radial distribution function $g(r)$ can be calculated by normalising the frequency of interacting pairs separated by a radius with the surface area formed by that radius.

Specifically,

$$Pair_{PE} = \frac{1}{2} \sum_{i=1}^{N} \sum_{j=1}^{N} p_{i,j}, \tag{1.33}$$

$$Bond_{PE} = \frac{1}{2} \sum_{i=1}^{N} \sum_{j=1}^{N} b_{i,j}, \tag{1.34}$$

$$Angle_{PE} = \frac{1}{2} \sum_{i=1}^{N} \sum_{j=1}^{N} a_{i,j}, \tag{1.35}$$

$$Total_{PE} = Pair_{PE} + Bond_{PE} + Angle_{PE}, \qquad (1.36)$$

$$Stress = \frac{Total\ potenial\ energy}{Volume}, \qquad (1.37)$$

$$Elastic\ Modulus = \frac{Stress}{Strain}, \qquad (1.38)$$

$$g(r) = \frac{1}{2\pi r^2} Freq_{i,j}, \qquad (1.39)$$

where $p_{i,j}$, $b_{i,j}$ and $a_{i,j}$ are the pair, bond distance and bond angle potential energy of interacting pairs i and j respectively. $Freq_{i,j}$ is the total number of particle j found within a separation distance r of reference particle i.

1.5   Scope and Objective

This study utilises software packages that perform coarse-grained molecular dynamics to simulate different micellar systems with the aim of understanding the dynamics, as well as stress and structural responses to uniaxial extensional flow field. Chapter 2 focuses on spherical vesicles. Here, the response of spherical micelles to uniaxial extensional flow is investigated. Micellar dynamics in low, moderate and high deformation rate is discussed. Structural response of the spherical micelles after exposure to specific deformation rate and accumulated strain are investigated and presented. The stress relaxation function is investigated. The hysteresis in loading and unloading stress is

presented.

In Chapter 3, the response of rod-like and worm-like micelles in uniaxial extensional flow is presented. Dynamics of the micelles at various deformation rates are discussed, and the stress relaxation mechanisms is discussed. Structural response of rod-like and worm-like micelles to relaxation following accumulated strain values at specific deformation rate is discussed. The stress relaxation function, and hysteresis in loading and unloading stress are presented.

Similarly, Chapter 4 focuses on the response of branched worm-like micelles in uniaxial extensional flow. As before, the dynamics of the micelles at various deformation rates are discussed, and the stress relaxation mechanism is analysed. Micellar stress and structural response after cessation of uniaxial extensional flow is presented. In Chapter 5, this work is summarised and future recommendations for research are presented.

Chapter 2

Dynamics of a Spherical Vesicle

2.1   Introduction

Structures formed by the spontaneous self-assembly of surfactant molecules[26–29] have garnered significant interest in the scientific community because of their vast potential industrial and commercial applications. These micellar structures have been extensively studied to understand their characteristics and underlying dynamics in viscoelastic solutions.[30–42, 42–49] Though the impartation of viscoelasticity is critical to most applications of micellar structures, there exist other emerging applications for micellar structures where viscoelasticity is not critical. For instance, micellar structures have been proposed as nano-carriers for cancer drug therapy.[50–64] Though blood vessels have length scales on the order of micrometers to millimetres,[65] plaque deposition can severely constrict the flow channel of these micellar nano-carriers. Since constriction in a flow channel can induce an extensional flow field that may result in significant irreversible deformation of micellar structures,[66] it is of considerable importance to understand the dynamics of spherical structures in extensional field.

Experimental methods can be limited by their inability to observe and quantify interactions between atoms at significant length- and time-scale that can bring clarity to the structure and consequent dynamics of micellar systems. To this effect, molecular dynamics simulation methods have been developed to take a closer look and complement the insight obtained from experimental studies on molecular systems. Recently, coarse-grained molecular dynamics (CGMD) simulations have been used to model aqueous solutions of cetyl trimethyl ammonium chloride (CTAC) and sodium salicylate (NaSal) and it has quite reliably modelled: the phenomenon of micellization;[4] micellar growth, transition, scission, and recombination;[9] changes in CTAC micellar structure with increase in NaSal concentration and the consequent non-monotonic dependence of solution zero-shear viscosity on mole ratio of NaSal to CTAC;[11] relationship between shear rate, tumbling frequency and orientation dynamics in simple shear flow that is in good agreement with mesoscopic theories;[67] and micellar mid-plane thinning and scission in solutions of rod-like micelles that are in good agreement with elastocapillary thinning of a viscoelastic fluid.[68] Using the insightful CGMD tool, this work investigates the dynamics and stress relaxation response of spherical vesicle in uniaxial extensional flow.

2.2 Simulation Details

In this study, self-assembled solutions were formed by solvating previously formed spherical vesicle in water.[69–75] The pre-formed spherical vesicle were molecular models of hexacosanoate anion and octyltrimethylammonium cation according to the Martini forcefield formalism.[76] In line with the Martini force field formalism, water was modelled as bead type P4; with additional 10% of bead type BP4 to prevent unnatural freezing of water at room temperature and pressure. BP4 and P4 bead types have same interaction parameter values, save the P4-BP4 interaction. Sodium ion was modelled as bead type Qd, chloride ion was modelled as bead type Qa; hexacosanoate anion was modelled as a chain with 1 hydrophilic bead and 6 hydrophobic beads, making a total of 7 beads. The hydrophilic bead was modelled as Martini bead type Qd, while the hydrophobes were modelled as bead type C1. Octyltrimethylammonium cation was modelled as a 3-bead chain with 1 hydrophilic bead and 2 hydrophobic beads. The hydrophilic bead was modelled as Martini bead type Q0, while the hydrophobic beads where modelled as bead type C2. Other details of the particle definition are presented in tables 2.1 to 2.5.

Table 2.1: Spherical vesicle particle types.

Index	Martini Bead Type	Atoms	Charge
Octyltrimethylammonium cation			
1	Q0	CH_2-CH_2-N^+-C_3H_9	1
2	C2	C_3H_6	0
3	C2	C_3H_7	0
Hexacosanoate anion			
1	Qa	C-OO^-	-1
2	C1	C_4H_8	0
3	C1	C_4H_8	0
4	C1	C_4H_8	0
5	C1	C_4H_8	0
6	C1	C_4H_8	0
7	C1	$C_5H_1 1$	0
Sodium ion			
1	Qd	Na^+	1
Chloride ion			

Continuation of Table 2.1			
Index	Martini Bead Type	Atoms	Charge
1	Qa	Cl^-	-1
Water			
1	P4	$4H_2O$	0
Anti-freeze water			
1	BP4	$4H_2O$	0

Table 2.2: Spherical vesicle angle interaction parameters.

i	j	k	Angle(degrees)	Force Constant$(kJ/mol \cdot nm^2)$
Octyltrimethylammonium cation				
1	2	3	180	25
Hexacosanoate anion				
1	2	3	180	25
2	3	4	180	25
3	4	5	180	25
4	5	6	180	25

i	j	k	Angle(degrees)	Force Constant($kJ/mol \cdot nm^2$)
5	6	7	180	25

Continuation of Table 2.2

Table 2.3: Spherical vesicle bond interaction parameters.

i	j	Bond length(nm)	Force Constant(kJ/mol)
Octyltrimethylammonium cation			
1	2	0.47	1250
2	3	0.47	1250
Hexacosanoate anion			
1	2	0.47	1250
2	3	0.47	1250
3	4	0.47	1250
4	5	0.47	1250
5	6	0.47	1250
6	7	0.47	1250

Table 2.4: Spherical vesicle Lennard Jones pair-wise interaction parameters.

Interacting pair	$\epsilon_{ij}(kJ/mol)$	$\sigma_{ij}(nm)$
P4 - BP4	5.6	0.57
P4 - P4	5.0	0.47
P4 - Qa	5.6	0.47
P4 - Q0	5.6	0.47
P4 - Qd	5.6	0.47
P4 - C1	2.0	0.47
P4 - C2	2.3	0.47
Qa - Qa	5.0	0.47
Qa - Q0	4.5	0.47
Qa - Qd	5.6	0.47
Qa - C1	2.0	0.62
Qa - C2	2.0	0.62
Q0 - Q0	3.5	0.47
Q0 - Qd	4.5	0.47
Q0 - C1	2.0	0.62

Continuation of Table 2.4		
Interacting pair	$\epsilon_{ij}(kJ/mol)$	$\sigma_{ij}(nm)$
Q0 - C2	2.0	0.62
Qd - Qd	5.0	0.47
Qd - C1	2.0	0.62
Qd - C2	2.0	0.62
C1 - C1	3.5	0.47
C1 - C2	3.5	0.47
C2 - C2	3.5	0.47

Table 2.5: Spherical vesicle simulation box details.

System Information	Value
Water beads	600000
Anti-freeze water beads	60000
Hexacosanoate beads	612
Sodium beads	612
Octyltrimethylammonium beads	99
Chloride beads	99

Continuation of Table 2.5	
System Information	Value
vesicle dimension	11.7nm × 10.5nm × 9.7nm
Box size	20nm × 63.2nm × 58.3nm

Equilibrium and extensional molecular dynamics simulations were carried out using the LAMMPS[77–79] package. During equilibrium simulations, NPT ensemble at 300K and 1 atm was obtained using the Nose Hoover thermostat and barostat. The gyration tensor $\underline{\underline{G}}$ was calculated from the coordinates obtained during equilibrium simulations, such that

$$G_{i,j} = \frac{1}{N} \sum_{k=1}^{N} (r_i^k - r_i^{cm})(r_j^k - r_j^{cm}), \tag{2.1}$$

where N is the number of particles in the self-assembled structures, r_i is the x, y, or z coordinate of a particle in the self-assembled structures, and r_i^{cm} is the centre of mass of the x, y or z coordinate. A characteristic time-scale for this structure is obtained from the autocorrelation of the eigen vector of the largest eigen value of the gyration tensor. This characteristic time was estimated to be 1ns as seen in figure 2.1.

In non-equilibrium simulations, the system was kept at 300K. The flow direc-

(a)
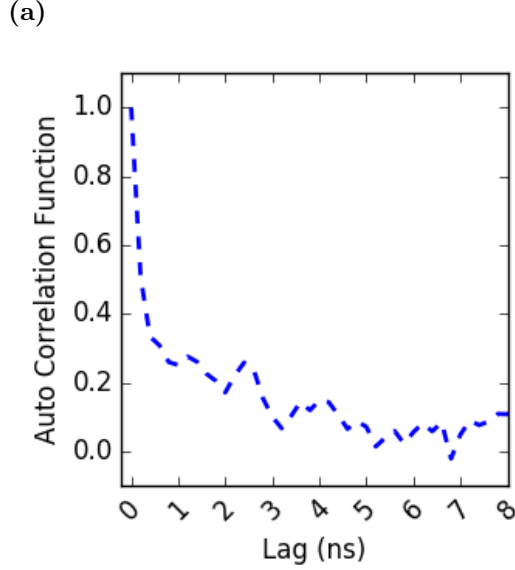
Figure 2.1: Autocorrelation function of (a)Spherical vesicle orientation.

tion underwent uniaxial extension at predefined extensional rates while the compression directions were maintained at 1 atm. In constructing the simulation system, the principal orientation axis of the self-assembled structure was the X direction such that uniaxial extension applied in the X and Y directions will be parallel and normal to the principal orientation axis of the structure. Extensional deformations were carried out in X and Y directions at $Wi \sim 0.3, 0.9, 3, 9, 30, 90$ until an accumulated strain of 10 units. Care was specifically taken to ensure the box dimensions were large enough to prevent interactions between particles and their periodic image during the course of the simulation. After accumulated strains values of 1, 3, and 5; the coordinates of the particles in these systems were extracted and equilibrium simulations were performed to observe stress and structural relaxation following uniaxial extensional deformation.

2.3 Results and Discussion

2.3.1 Effect of Deformation Rate on Dynamics

Vesicular dynamics was found to be a function of the deformation rate. At $Wi \sim 0.3$, the spherical vesicle under-went flow induced translation/diffusion like a rigid body. That is, there was no observable distortion to the aspect ratio as the centre of mass translated in the direction of flow.

This can be explained by the deformation time-scale being much longer than the relaxation time-scale, thus enabling effective energy dissipation and stress relaxation during deformation as shown in figs. 2.2 to 2.3. This effective stress energy dissipation/stress relaxation implies insignificant deformation on vesicular micro structure, which in turn implies less significant development of unfavourable interactions between polar and apolar moieties as seen in figs 2.4 and 2.5.

The consequence of mitigated development of unfavourable interactions in the solution is less significant changes in the entropy of the system that results in less significant changes in the stress response of the self-assembled structure as seen in fig 2.2.

At deformation rate such that $Wi \sim 3$, the time-scale of deformation becomes comparable to that of relaxation. This causes less effective energy dissipation and stress relaxation during deformation, as shown in figs. 2.2
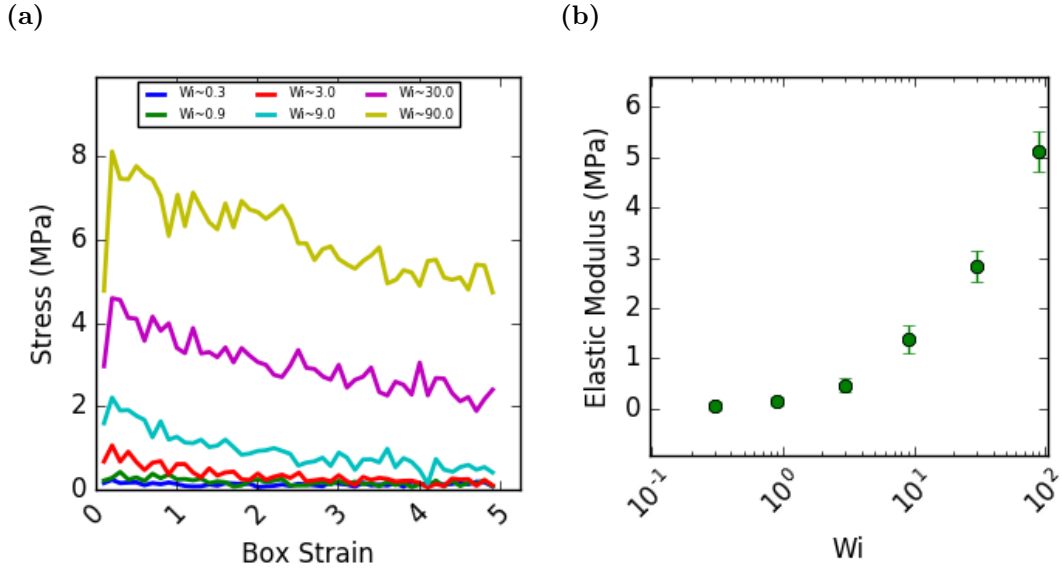
Figure 2.2: Effect of Wi on (a)stress and (b)elastic modulus of spherical vesicle.

to 2.3, and the flow begins to have significant impact on the micro-structure. These changes in micro-structure imply the development of unfavourable polar-apolar interactions, seen in fig 2.4, and corresponding increase in the system stress response.

When the deformation rate is such that $Wi \sim 30$, the time-scale for deformation becomes much shorter that of relaxation. This implies vesicular relaxation ability whilst undergoing deformation is severely diminished. In this case, flow-induced translational diffusion continues to occur. However, it is ineffective in dissipating the energy and relieving the stress being applied to the system at this deformation rate. Consequently, the excess energy stretches the vesicle in the direction of flow and its aspect ratio is sharply distorted. This distortion of the micro-structure, shown in fig 2.5, causes development of polar-apolar interactions, decrease in entropy and significant
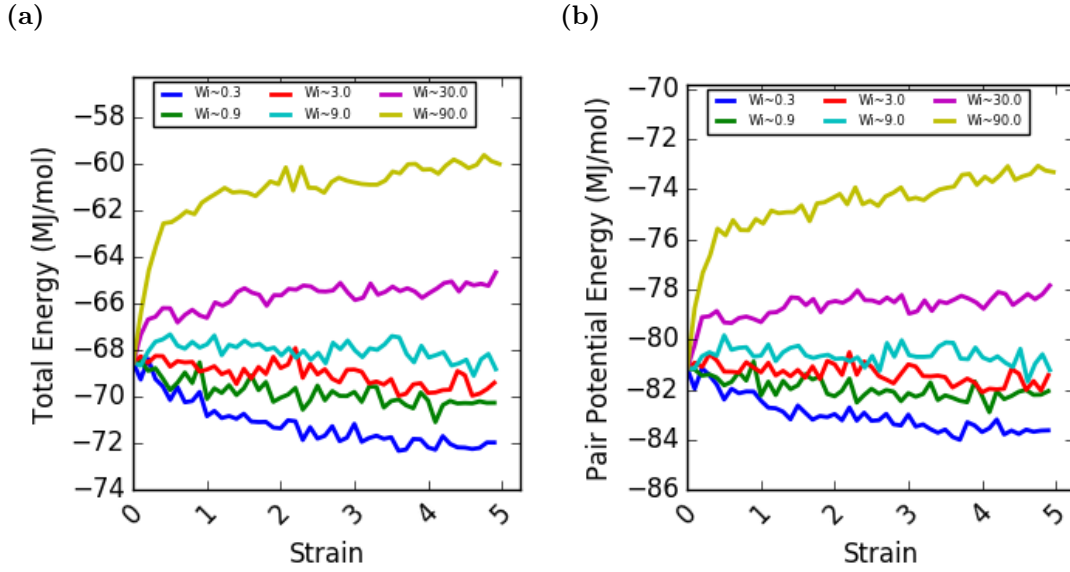
Figure 2.3: Effect of Wi on (a)total and (b)pair-wise potential energy of spherical vesicle.

stress response observed in fig 2.2.

The analysis of the elastic modulus, shown in fig 2.2, typifies the trend of stress response as a function of deformation rate. When the deformation rate was low and the vesicle had sufficient time to relax during the deformation, a more solid-like response was observed. However, increasing deformation rate till its time-scale becomes comparable with the time-scale of relaxation caused a more liquid response from these vesicular systems.

It was interesting to observe that despite subjecting this system to an accumulated strain value of 10 and a deformation rate of $Wi \sim 300$, the spherical vesicle did not undergo scission though it sustained severe distortions to its micro-structure. This "resistance" to scission is proposed to be due to its shape isotropy that promotes uniform distribution of stress across the surface of the vesicular structure thereby discouraging the development of local high
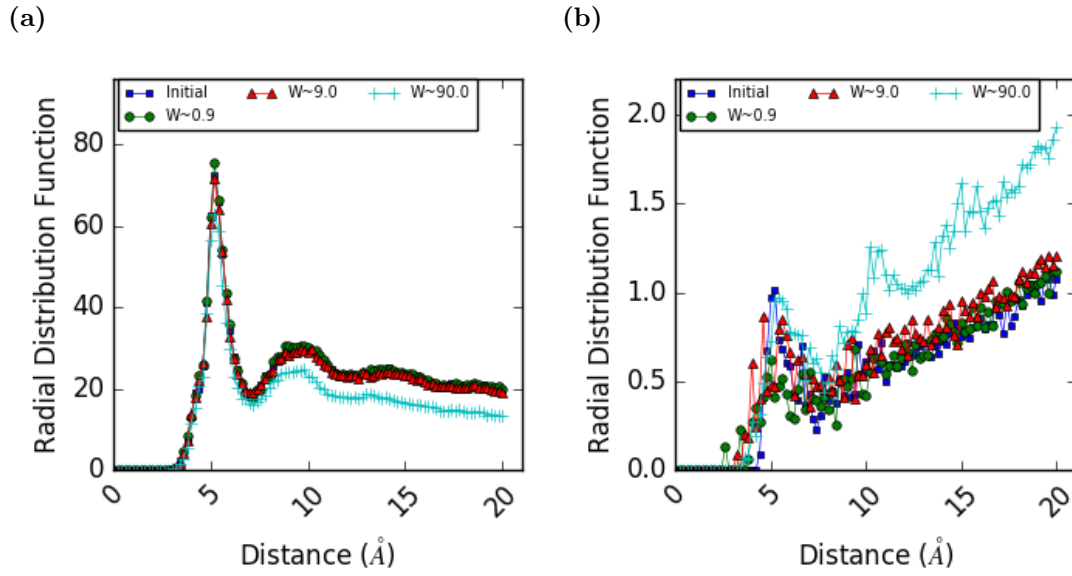
Figure 2.4: Effect of Wi on g(r) of (a)apolar-apolar and (b)apolar-polar spherical vesicle moieties after accumulated strain of 5 at equilibrium ($\square$), $Wi \sim 0.9$ (O), $Wi \sim 9$ ($\triangle$), and $Wi \sim 90$ (+).

energy regions that typically result in vesicular scission. This characteristic

of spherical vesicles makes it an ideal candidate for nano-carrier applications.
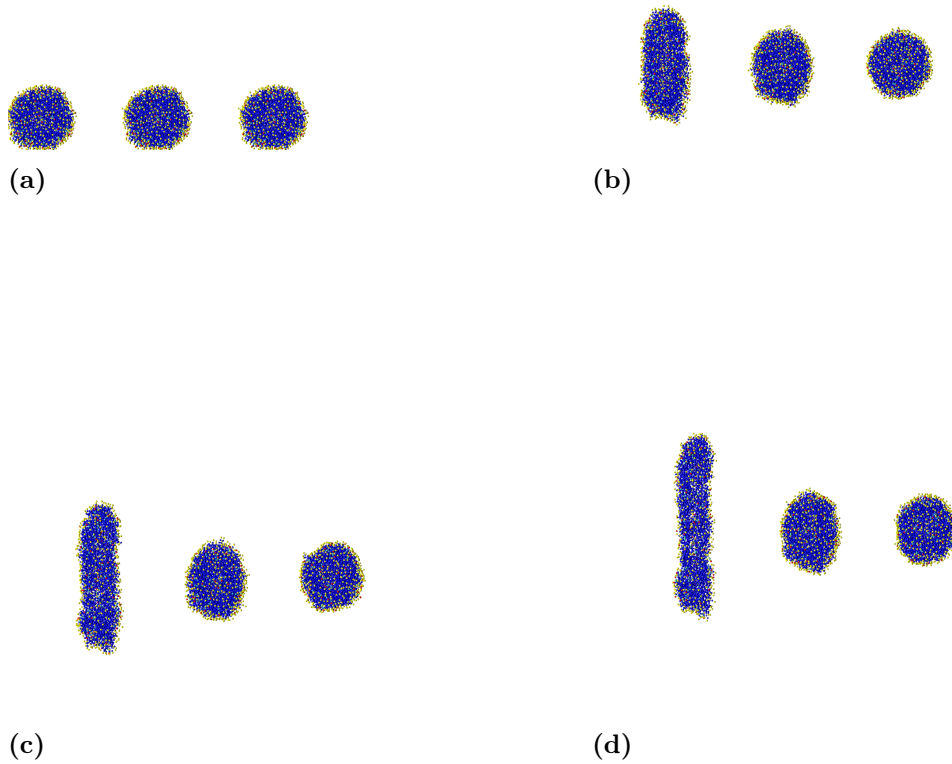
Figure 2.5: Spherical vesicle structures at accumulated strain of (a)0, (b)3, (c)6, and (d)9. In each image, the structure at $Wi \sim 30$ is depicted at the left; $Wi \sim 3$ in the middle; $Wi \sim 0.3$ at the right.

2.3.2 Effect of Orientation on Dynamics

Spherical structures, by nature, are isotropic with nearly equal aspect ratio and radii of gyration. Consequently, spherical structures were not expected to have significant difference in spatial distribution, energy, stress, and structural response with respect to the direction of deformation. The results of this experiment was in agreement with our assumptions as seen in figs. 2.6 to 2.8. Similar to the response in the previous discussion, spherical structures showed insignificant deformation at $Wi \sim 0.3$; noticeable deformation at $Wi \sim 3$; and significant micro-structure distortion at $Wi \sim 30$.
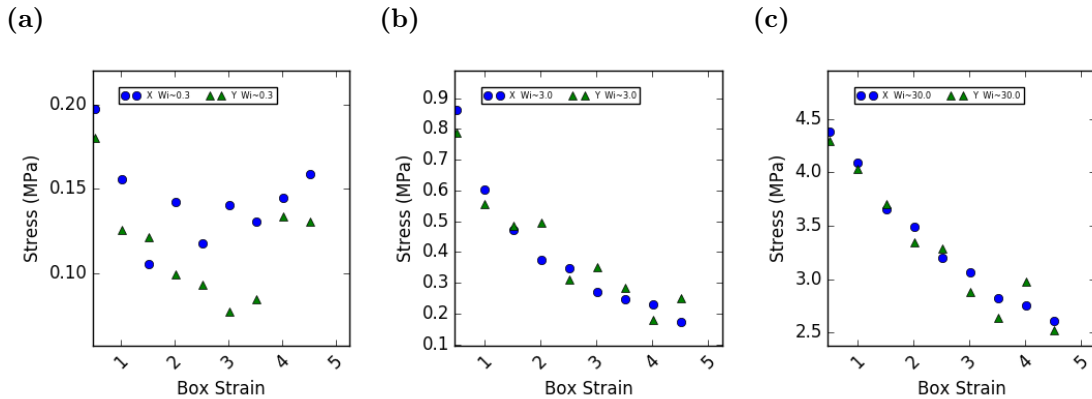
Figure 2.6: Stress response to deformation at (a)$Wi \sim 0.3$, (b)$Wi \sim 3$, and (c)$Wi \sim 30$ in X (O) and Y ($\triangle$) directions.

2.3.3 Stress and Structural Relaxation

When vesicular structure was removed from uniaxial extensional deformation, patterns of structural recovery were observed at investigated deformation rates and accumulated strains. At $Wi \sim 0.3$, vesicular structure did
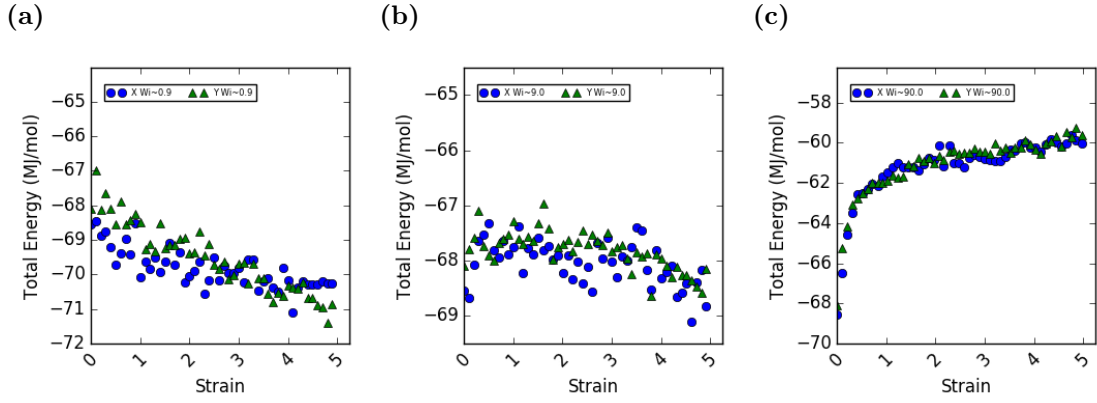
Figure 2.7: Total vesicular potential energy at (a)$Wi \sim 0.3$, (b)$Wi \sim 3$, and (c)$Wi \sim 30$ in X (O) and Y ($\triangle$) directions.
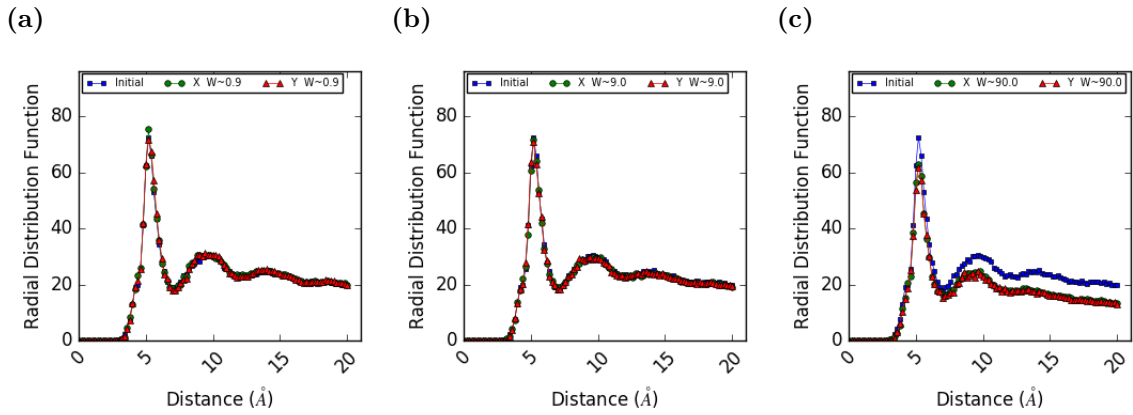
Figure 2.8: Apolar-apolar spatial distribution at (a)$Wi \sim 0.3$, (b)$Wi \sim 3$, and (c)$Wi \sim 30$ in equilibrium ($\square$), X (O), and Y ($\triangle$) direction deformation field.

not undergo significant distortions, so structural recovery was not observable. At $Wi \geq O(1)$, the vesicular structure promptly re-oriented itself to shield hydrophobic beads from unfavourable interactions with water.

When $Wi \sim 3$, structural recovery was observed within 2λ, 5λ, and 10λ for accumulated strain values of 1, 3, and 5 respectively. When $Wi \sim 30$, structures were recovered within 15λ, 35λ, 100λ at accumulated strains of 1, 3 and 5 respectively.

Stress relaxation following uniaxial extensional flow was found to be abrupt and closely matching an exponential decay function, seen in fig 2.10. This
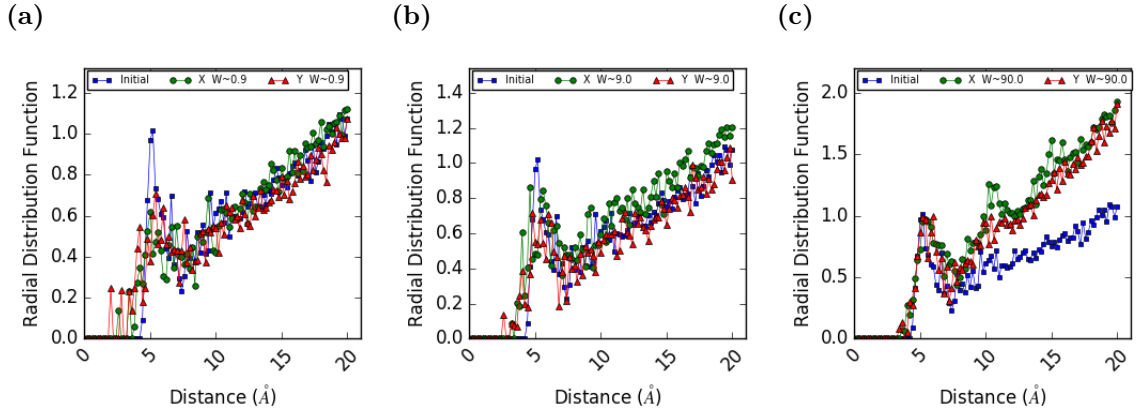
Figure 2.9: Polar-apolar spatial distribution at (a)$Wi \sim 0.3$, (b)$Wi \sim 3$, and (c)$Wi \sim 30$ in equilibrium ($\square$), X (O), and Y ($\triangle$) direction deformation field.

finding is congruent with experimental and Brownian dynamics simulations conducted in dilute polymer solutions.[80–83] The exponential decay rate was found to $\sim 10\lambda$, resulting in complete stress relaxation in fractions of the longest relaxation time. This observation of stress decay time that differed from the longest relaxation time is in line with multi-mode relaxation models of viscoelasticity. Thus, one of the faster relaxation modes is thought to be responsible for the immediate re-alignment of deformed vesicular structure to shield hydrophobic beads from solvent interactions.

Hysteresis in the loading stress (i.e. the stress response when uniaxial extensional deformation was applied) and the unloading stress (i.e. the stress response in relaxation following uniaxial deformation) was observed as seen in fig 2.11. This is analogous to the stress-birefringence hysteresis observed in dilute polymer solutions.[80–83] In viscoelastic fluids, hysteresis in the loading and unloading stress is thought to be a measure of the energy absorbed by the complex fluid. However, in micellar structures, this hysteresis is thought
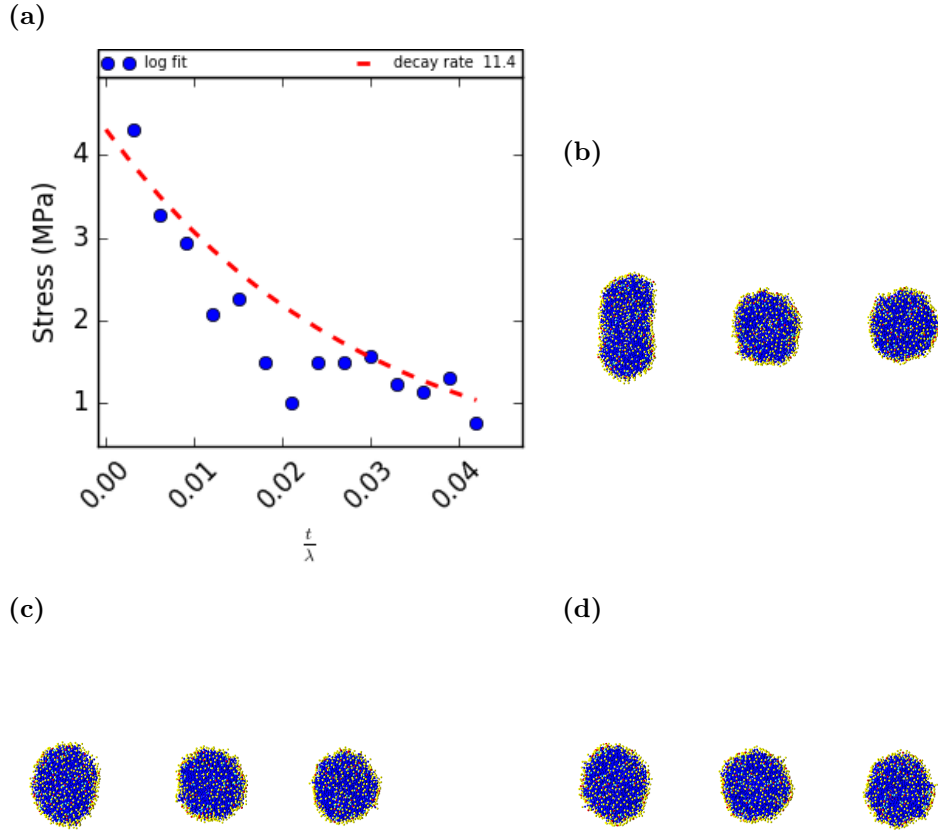
Figure 2.10: Spherical vesicle (a)stress and structure at (b)1λ (c)3λ (d)5λ upon cessation of uniaxial extensional deformation. In each image, the structure at $Wi \sim 30$ is depicted at the left; $Wi \sim 3$ in the middle; $Wi \sim 0.3$ at the right.

to be a result of the unfavourable interactions between moieties in the solution. This hypothesis is supported by the fact that abrupt stress relaxation occurs long before the self-assembled structure completed structural recovery, suggesting that structural evolution is not primarily responsible for the hysteresis in these systems as seen in fig 2.10.

Congruent with the finite extensible nonlinear elastic (FENE) model, stress hysteresis was observed to grow with accumulated strain and deformation rate as seen in fig 2.11. This observation is in-line with the current theory of stress hysteresis. That is, a larger value of accumulated strain implies a

40

greater time window for the addition of excess energy into the system via uniaxial extension. Thus, it is logical that a measure of the absorbed energy in the system will increase with accumulated strain. In the same way, the increase of stress hysteresis with deformation rate can also be explained. As mentioned earlier, during the course of deformation, the vesicular structure is able to effectively relax when the deformation rate is low. This follows that a significant fraction of the imparted excess energy can be dissipated in tandem with the added energy during the addition of excess energy via deformation. On the other hand, as the deformation rate increases, the vesicle is less effective at relaxing the added energy, causing greater hysteresis, a measure of the absorbed energy, to increase.

2.4 Conclusion

Uniaxial extension deformation was imposed on a system consisting of solvated spherical vesicle. At certain predefined deformation rates and accumulated strain, the structures were extracted, analysed and subjected to equilibrium simulation for the observation of stress and structural relaxation. At low deformation rate, this vesicle was observed to undergo flow-induced translation (with no observable perturbations to its aspect ratio) as its predominant stress release mechanism. At deformation occurring at a time-scale

comparable to the relaxation time, distortions to the aspect ratio were observed. At deformation rates with time-scale much shorter than relaxation time, significant distortions were observed in the vesicular micro-structure. The vesicle was observed to be particularly "resistant" to scission and it was suggested that its shape isotropy aided in the distribution of stress across the vesicular surface area, making it easy to neutralise local build up of stress that has been known to cause vesicular scission. The orientation of deformation was observed to have insignificant impact to vesicular stress, dynamics and structural response to uniaxial deformation. This is proposed to be due to the uniformity of its aspect ratio.

Spherical vesicles were also found to readily relax with the initial decay matching an exponential function. The exponential decay rate was found to be greater than the longest relaxation time of the vesicle, resulting in stress relaxation in fractions of the longest relaxation time. Hysteresis in the loading and unloading stress was observed to increase with the rate of deformation and total accumulated strain.

In all investigated deformation rates and accumulated strain, elastic structural recovery in relaxation following uniaxial extensional deformation was achieved. These characteristics of spherical vesicles make them particularly suited for nano-carrier applications, such as in drug delivery.
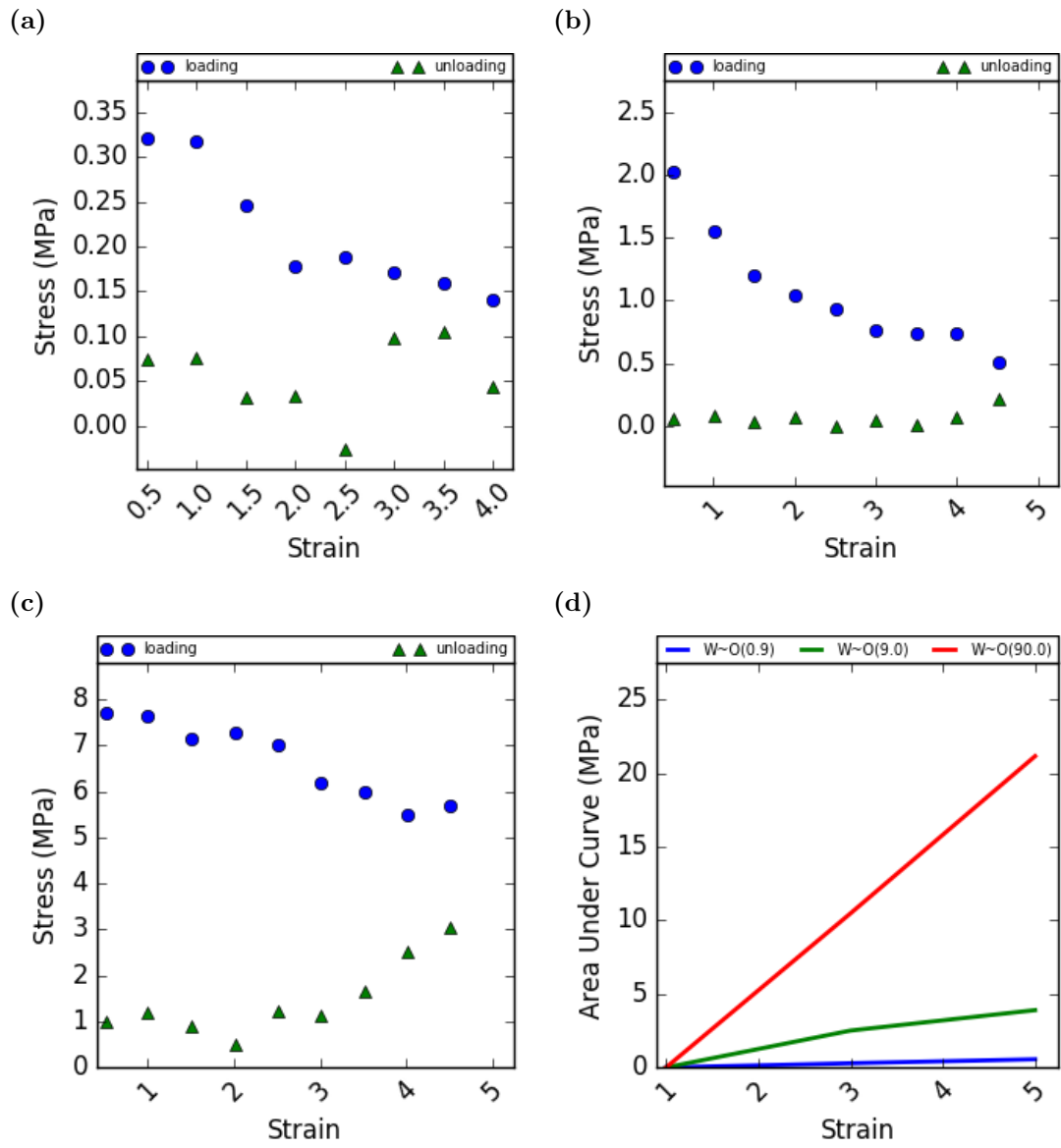
Figure 2.11: Loading (O) and unloading ($\triangle$) stress hysteresis at (a)$Wi \sim 0.9$, (b)$Wi \sim 9$, and (c)$Wi \sim 90$. (d)Area under the loading-unloading curve of spherical vesicle as a function of accumulated strain.

43

Chapter 3

Dynamics of Cylindrical Micelles

3.1 Introduction

Surfactant molecules are characterised by chemical moieties that enable them spontaneously self-assemble in solution. When the concentration of these surfactants is dilute, globular structures tend to be preferred. Increasing the concentration of these surfactants typically causes micellar growth, and in some cases, structural transition to cylindrical micelles. Initially, these cylindrical micelles are rigid (rod-like micelles) until further lateral growth beyond its persistence length. When micelles achieve contour lengths above their persistence lengths (worm-like micelles), their structure and dynamics start to closely resemble that of polymer solutions. Unlike polymer molecules that are quenched during synthesis, worm-like micelles typically exist in a dynamic equilibrium of scission and recombination, earning them the name "equilibrium/living polymer". Similar to polymer systems, micellar solutions can entangle when their volume fraction exceeds a critical value. Since worm-like micelles undergo similar dynamics and stress relaxation as polymer solutions, reptation has been theorised to be the predominant stress

release mechanism in entangled, and concentration micellar solutions.

In reptation theory,[84–87] micelles are theorised to undergo stress relaxation via one-dimensional diffusion along a primitive path mapped by the topological constraints on the micellar contours. Micellar structures, unlike polymers that are chemically bonded, can undergo scission and recombination, which provides an additional stress release mechanism. In these systems, the dominant stress release mechanism depends on the time-scale of the scission and reptation. When the time for reptation is short compared with scission, the micelle undergoes reptation as its dominant relaxation mechanism. When the time-scale for scission is short, the micelle undergoes scission as its dominant stress release mechanism. In this regime, worm-like micellar linear viscoelastic response had been described as Maxwell fluids with a single relaxation time that is the geometric mean of the time-scales of scission and reptation.[17,88] Temporary branching of entangled worm-like micelles, called ghost-like crossings, have also been theorised as an additional stress release mechanism.

Differences in stress relaxation of different micellar structures is succinctly depicted in solutions of ionic surfactants with binding counter-ion salts where non-monotonic dependence and double viscosity peaks were observed as salt concentration was changed.[2,19,21] The first viscosity peak was associated with worm-like micellar growth, the first trough was associated with branch-

ing of the worm-like micelles that introduced additional fluidity to the system, and the second peak was associated with the formation of entangled multi-connected networks of worm-like micelles. These results have also been confirmed using coarse-grained molecular dynamics simulations.[68]

Under the influence of shear flow, worm-like micelles have been observed to undergo flow alignment, and shear thinning. In these systems, it is understood that the rotational component of the flow causes coiled, stretched, and tumbling dynamics with a frequency that increases with the deformation rate.[67] In some instances, shear-bands caused by shear-induced structuring can occur in micellar solutions as a result of shear-induced transition from disordered to ordered states. Upon exposure to elongational deformation, these structures have been observed to strain-harden in some experiments and this strain-hardening was theorised to be due to flow-induced micellar growth. In other experiments, micellar growth was not observed. Though stress hysteresis has been observed in polymer solutions due to differing stress evolution in relaxation after deformation,[89] the existence of stress hysteresis in micellar solutions is still debatable.[90]

Though extensive work has been done in understanding micellar dynamics,[91–103,103–110] there exists a gap in the understanding of micellar dynamics and relaxation in dilute systems. To this end, this work investigates the dynamics and stress relaxation mechanisms of systems consisting of a single

rod-like, and worm-like micelle in aqueous solution under uniaxial exten-
sional flow field.

3.2   Simulation Details

In this study, self-assembled solutions were formed by solvating previously
formed rod-like and worm-like micelle in water. The pre-formed rod-like
and worm-like micelle[111–117] were molecular models of hexacosanoate anion
and palmitate anion according to the Martini forcefield formalism. In line
with the Martini force field formalism, water was modelled as bead type
P4; with additional 10% of bead type BP4 to prevent unnatural freezing
of water at room temperature and pressure. BP4 and P4 bead types have
same interaction parameter values, save the P4-BP4 interaction. Sodium
ion was modelled as bead type Qd; hexacosanoate anion was modelled as
a chain with 1 hydrophilic bead and 6 hydrophobic beads, making a total
of 7 beads. The hydrophilic bead was modelled as Martini bead type Qd,
while the hydrophobes were modelled as bead type C1. Palmitate anion
was modelled as a 5-bead chain with 1 hydrophilic bead and 4 hydrophobic
beads. The hydrophilic bead was modelled as Martini bead type Qa, while
the hydrophobic beads where modelled as bead type C1. Other details of
the particle definition are presented in tables 3.1 to 3.6.

Table 3.1: Cylindrical micelle particle types.

Index	Martini Bead Type	Atoms	Charge
Palmitate anion			
1	Qa	$C\text{-}OO^-$	-1
2	C1	C_3H_6	0
3	C1	C_4H_8	0
4	C1	C_4H_8	0
5	C1	C_4H_9	0
Hexacosanoate anion			
1	Qa	$C\text{-}OO^-$	-1
2	C1	C_4H_8	0
3	C1	C_4H_8	0
4	C1	C_4H_8	0
5	C1	C_4H_8	0
6	C1	C_4H_8	0
7	C1	C_5H_11	0
Sodium ion			

Continuation of Table 3.1			
Index	Martini Bead Type	Atoms	Charge
1	Qd	Na$^+$	1
Chloride ion			
1	Qa	Cl$^-$	-1
Water			
1	P4	4H$_2$0	0
Anti-freeze water			
1	BP4	4H$_2$0	0

Table 3.2: Cylindrical micelle angle interaction parameters.

i	j	k	Angle(degrees)	Force Constant($^{kJ}/_{mol \cdot nm^2}$)
Palmitate anion				
1	2	3	180	25
2	3	4	180	25
3	4	5	180	25
Hexacosanoate anion				

			Continuation of Table 3.2	
i	j	k	Angle(degrees)	Force Constant$(kJ/mol \cdot nm^2)$
1	2	3	180	25
2	3	4	180	25
3	4	5	180	25
4	5	6	180	25
5	6	7	180	25

Table 3.3: Cylindrical micelle bond interaction parameters.

i	j	Bond length(nm)	Force Constant(kJ/mol)
		Palmitate anion	
1	2	0.47	1250
2	3	0.47	1250
3	4	0.47	1250
4	5	0.47	1250
		Hexacosanoate anion	
1	2	0.47	1250

		Continuation of Table 3.3	
i	j	Bond length(nm)	Force Constant($^{kJ}/_{mol}$)
2	3	0.47	1250
3	4	0.47	1250
4	5	0.47	1250
5	6	0.47	1250
6	7	0.47	1250

Table 3.4: Cylindrical micelle Lennard Jones pair-wise interaction parameters.

Interacting pair	$\epsilon_{ij}(^{kJ}/_{mol})$	$\sigma_{ij}(nm)$
P4 - BP4	5.6	0.57
P4 - P4	5.0	0.47
P4 - Qa	5.6	0.47
P4 - Qd	5.6	0.47
P4 - C1	2.0	0.47
Qa - Qa	5.0	0.47
Qa - Qd	5.6	0.47
Qa - C1	2.0	0.62

Continuation of Table 3.4		
Interacting pair	$\epsilon_{ij}(kJ/mol)$	$\sigma_{ij}(nm)$
Qd - Qd	5.0	0.47
Qd - C1	2.0	0.62
C1 - C1	3.5	0.47

Table 3.5: Rod-like micelle simulation box details.

System Information	Value
Water beads	430000
Anti-freeze water beads	43000
Palmitate beads	64
Sodium beads	64
Hexacosanoate beads	471
Sodium beads	471
Micelle dimension	17.9nm × 8.2nm × 7.3nm
Box size	25.0nm × 59.1nm × 54.6nm

Table 3.6: Worm-like simulation box details.

System Information	Value
Water beads	605000
Anti-freeze water beads	60500
Palmitate beads	837
Sodium beads	837
Hexacosanoate beads	124
Sodium beads	124
Micelle dimension	23.5nm × 13.9nm × 14.0nm
Box size	25.8nm × 62.6nm × 63.1nm

Equilibrium and extensional molecular dynamics simulations were carried out using the LAMMPS[77–79] package. During equilibrium simulations, NPT ensemble at 300K and 1 atm was obtained using the Nose Hoover thermostat and barostat. The gyration tensor $\underline{\underline{G}}$ was calculated from the coordinates obtained during equilibrium simulations, such that

$$G_{i,j} = \frac{1}{N} \sum_{k=1}^{N} (r_i^k - r_i^{cm})(r_j^k - r_j^{cm}), \qquad (3.1)$$

where N is the number of particles in the self-assembled structures, r_i is the x, y, or z coordinate of a particle in the self-assembled structures, and r_i^{cm} is the centre of mass of the x, y or z coordinate. A characteristic time-scale for this structure is obtained from the autocorrelation of the eigen vector of the largest eigen value of the gyration tensor. This characteristic time was estimated to be 3ns for the rod-like and worm-like micelle as seen in figure 3.1.

(a) **(b)**
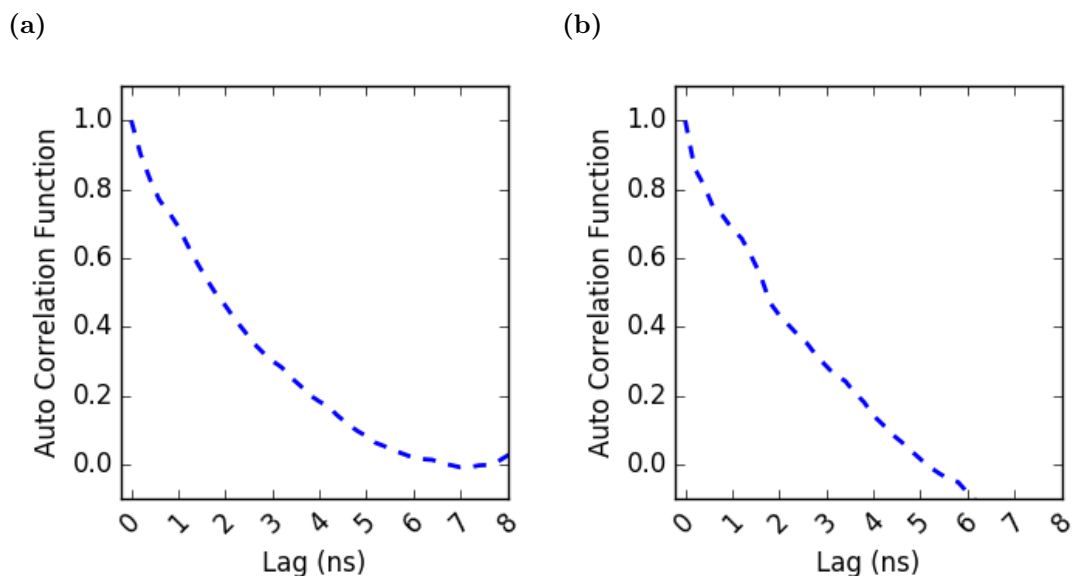
Figure 3.1: Autocorrelation function of (a)rod-like (b)worm-like micellar orientation.

In non-equilibrium simulations, the system was kept at 300K. The flow direction underwent uniaxial extension at predefined extensional rates while the compression directions were maintained at 1 atm. In constructing the simulation system, the principal orientation axis of the self-assembled structure was the X direction such that uniaxial extension applied in the X and Y directions will be parallel and normal to the principal orientation axis of the

structure. Extensional deformations were carried out in X and Y directions at $Wi \sim 0.3, 0.9, 3, 9, 30, 90$ until an accumulated strain of 10 units. Care was specifically taken to ensure the box dimensions were large enough to prevent interactions between particles and their periodic image during the course of the simulation. After accumulated strains values of 1, 3, and 5; the coordinates of the particles in these systems were extracted and equilibrium simulations were performed to observe stress and structural relaxation following uniaxial extensional deformation.

3.3   Results and Discussion

3.3.1   Effect of Deformation Rate on Dynamics of Cylindrical Micelle

The dynamics and stress response of this system was observed to depend on the deformation rate. When the deformation rate was such that $Wi \sim 0.3$, the micelle was observed to undergo flow-induced translational diffusion as its relaxation mechanism. However, unlike the spherical vesicle that had non-observable perturbations to its aspect ratio, this rod-like micelle underwent perturbations in the axial direction while drifting in the direction of flow. Since the time-scale for deformation at this rate was much longer than the relaxation time, the structure was able to effectively relax whilst under

extensional flow field, resulting in the dissipation of applied energy, easing of stress, insignificant distortion to its micro-structure, mitigation of unfavourable polar-apolar interactions, and low stress response as seen in figs. 3.2 to 3.4.

(a)

(b)
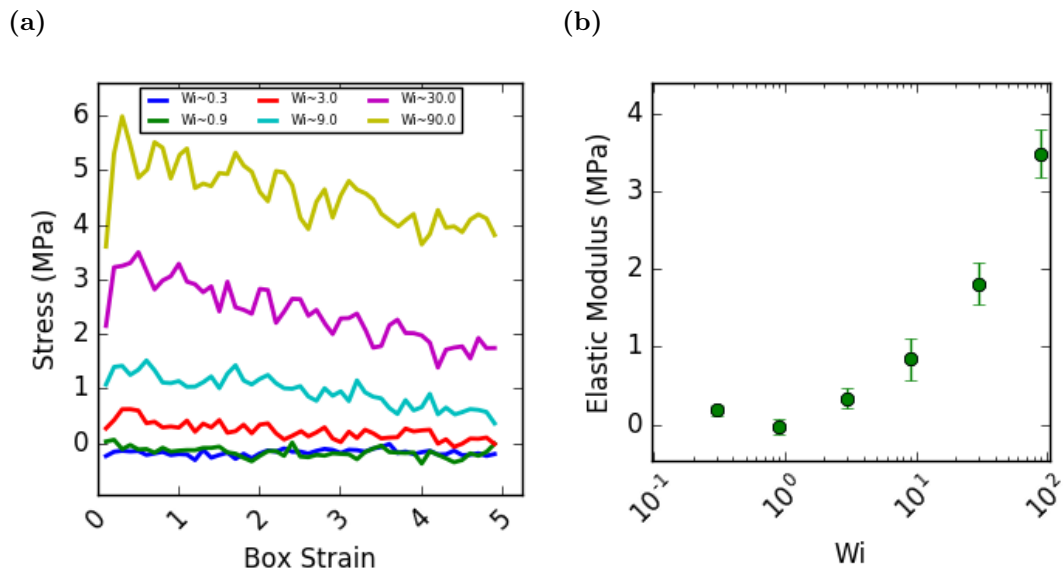
Figure 3.2: Effect of Wi on (a)stress and (b)elastic modulus of rod-like micelle.

(a)

(b)
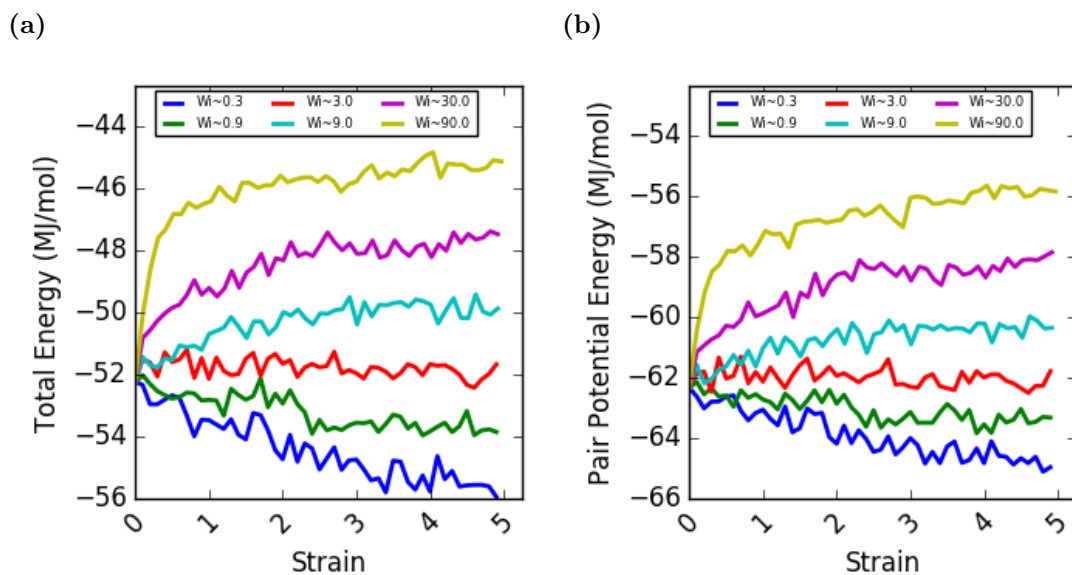
Figure 3.3: Effect of Wi on (a)total and (b)pair-wise potential energy of rod-like micelle.
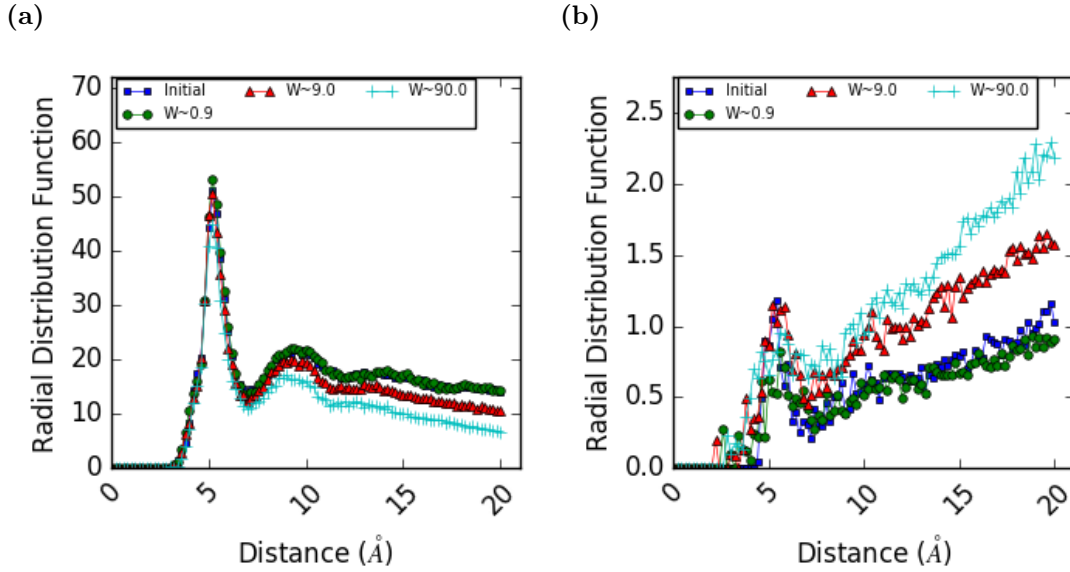
Figure 3.4: Effect of Wi on g(r) of (a)apolar-apolar and (b)apolar-polar rod-like micellar moieties after accumulated strain of 5 at equilibrium ($\square$), $Wi \sim 0.9$ (O), $Wi \sim 9$ ($\triangle$), and $Wi \sim 90$ (+).

Worm-like micelles showed similar dynamics as rod-like micelles. When the deformation rate was low and $Wi \sim 0.3$, flow-induced translational diffusion and axial perturbations were observed. These axial and contour length perturbations are proposed to be responsible for stress distribution that result in neutralisation of local high energy regions along the micellar contour length. Since local high energy regions were neutralised, the likelihood of micellar scission at this deformation rate was significantly lowered as seen in figs. 3.6 to 3.8.

When the deformation rate was increased, at $Wi \sim 3$, such that its time-scale was comparable to that of relaxation, significant micellar distortion began to occur in addition to micellar drift in the direction of flow. This distortion to the micro-structure is caused by the diminished micellar ability to relax during deformation, and resulted in development of unfavourable polar-
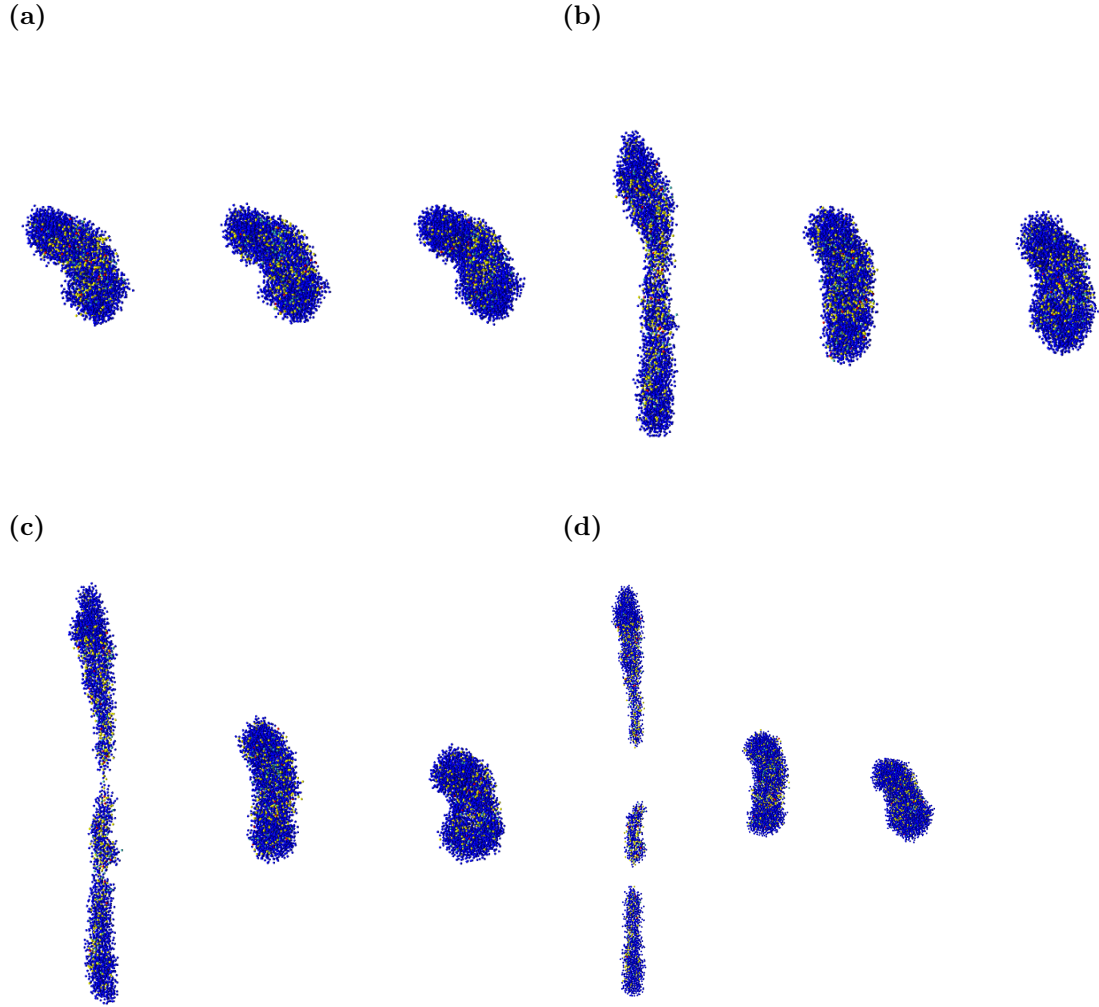
Figure 3.5: Rod-like micelle structures at accumulated strain of (a)0, (b)3, (c)6, and (d)9. In each image, the structure at $Wi \sim 30$ is depicted at the left; $Wi \sim 3$ in the middle; $Wi \sim 0.3$ at the right.

apolar interactions. The development of unfavourable interactions resulted in decreased system entropy, that in turn caused increased stress response, as seen in figs. 3.2 to 3.5.

Micellar scission is thought to result from relatively non-homogeneous counterion translation during deformation that cause local ion depletion and high-energy regions within the micellar contour length, resulting in increased susceptibility to scission.[68] At Wi $\geq O(1)$, the less effective micellar stress relaxation is proposed to permit the persistence of uneven stress distribu-
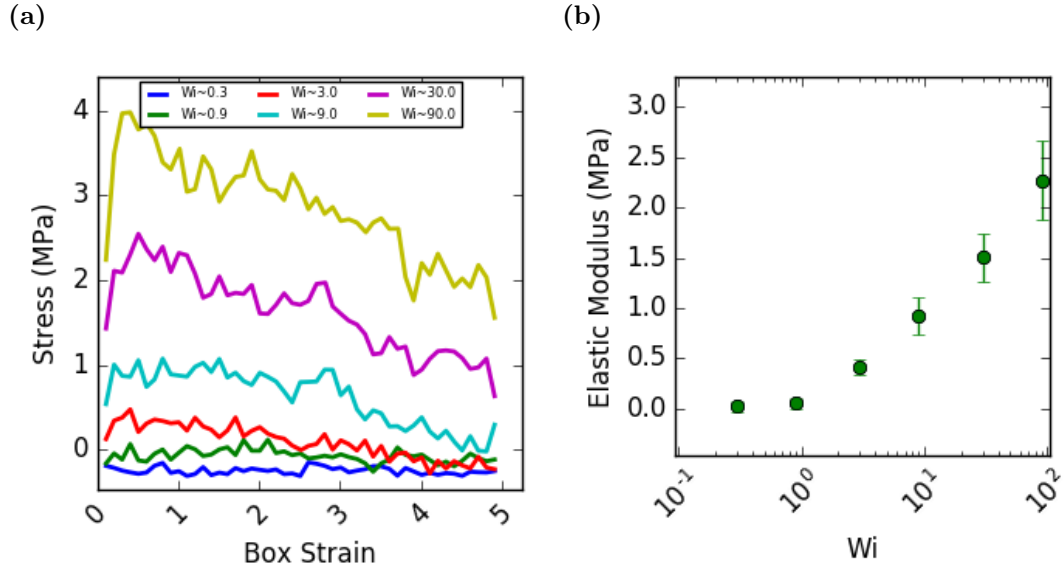
Figure 3.6: Effect of Wi on (a)stress and (b)elastic modulus of worm-like micelle.

tion along the surface of the structure. This in turn resulted in local regions of high energy that caused micellar scission, as observed in figs 3.5 and 3.9. Micellar scission occurred at different points on the contour length, and the child-micelles of this worm-like micelles had different lengths. This finding is in agreement with mean field theory. After micellar scission, the child-micelles continued to undergo flow-induced translation. Though further scission of the child-micelles were not observed in this experiment, they are theoretically possible if the child-micelles develop local high-energy regions that make micellar scission energetically favourable.

The elastic modulus, shown in figs 3.2 and 3.6, showed similar variation to deformation rate as stress. When the deformation rate was low and the micelle had sufficient time to relax during the deformation, a more solid-like response was observed. However, increasing deformation rate till its time-
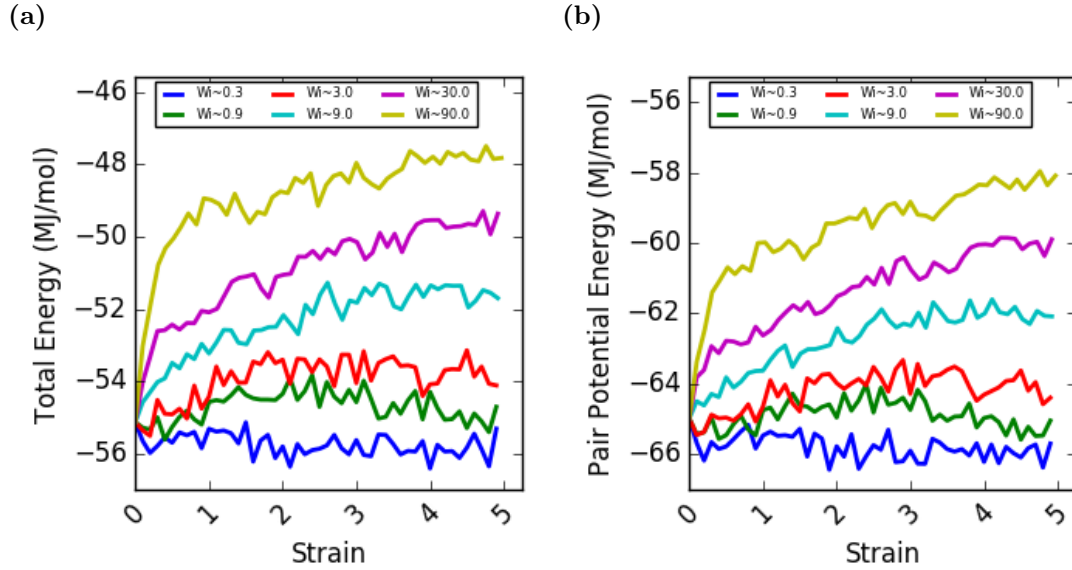
Figure 3.7: Effect of Wi on (a)total and (b)pair-wise potential energy of worm-like micelle.

scale becomes comparable with the time-scale of relaxation caused a more liquid response from these micellar systems, as is typical for these kinds of materials.

3.3.2 Effect of Orientation on Dynamics

Cylindrical micelles are structurally anisotropic with potentially vastly different aspect ratios. Thus the direction of deformation relative to the orientation of the micelle may potentially influence the micellar structure and stress response in uniaxial deformation.

Structural response to normal-direction deformation flow (i.e. flow in a direction normal to the micellar orientation) was observed to be similar to its response to parallel-direction flow (i.e flow in a direction parallel to the micellar orientation). At low deformation rate, the micelle was observed
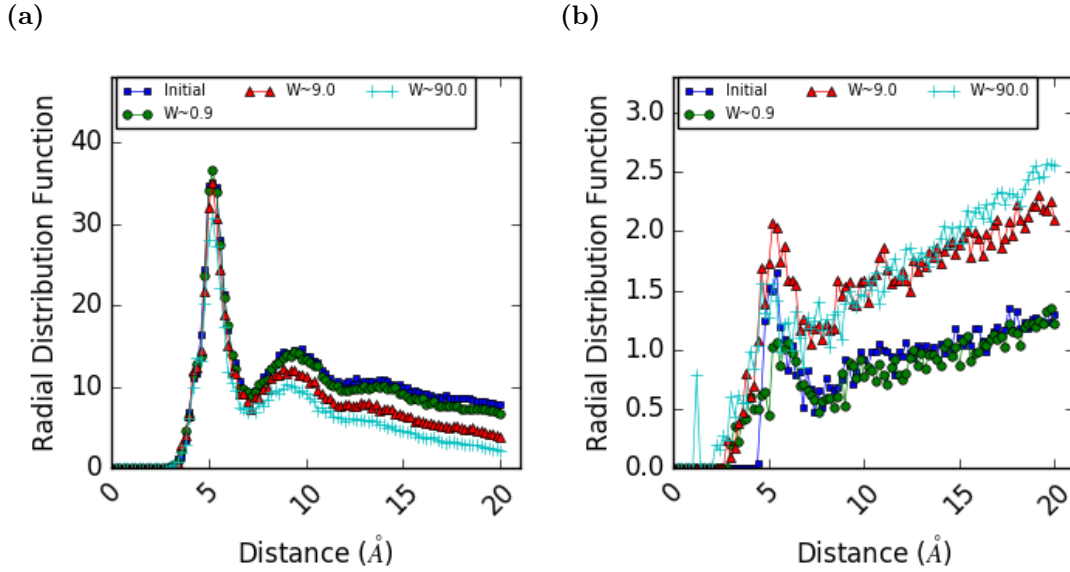
Figure 3.8: Effect of Wi on g(r) of (a)apolar-apolar and (b)apolar-polar worm-like micelle moieties after accumulated strain of 5 at equilibrium ($\square$), $Wi \sim 0.9$ (O), $Wi \sim 9$ ($\triangle$), and $Wi \sim 90$ (+).

to undergo flow-induced translation. Though uniaxial deformation lacks a rotational component, during the course of this flow, the micelle gradually re-aligned itself such that its orientation was parallel to the deformation direction. Though it was not observed, it is expected that given sufficient time, these cylindrical micelles will completely align itself to the flow direction. This flow alignment was possible because the time-scale for relaxation was shorter than the time-scale for deformation, affording the micelle the opportunity to relieve some stress on its structure by re-aligning itself to the flow direction. At moderate and high deformation rate, flow induced translation, alignment were diminished, and micro-structure distortion were observed.

Analysis of the stress showed some variations in the stress response in normal- and parallel-direction flow for both types of cylindrical micelles explored.

61
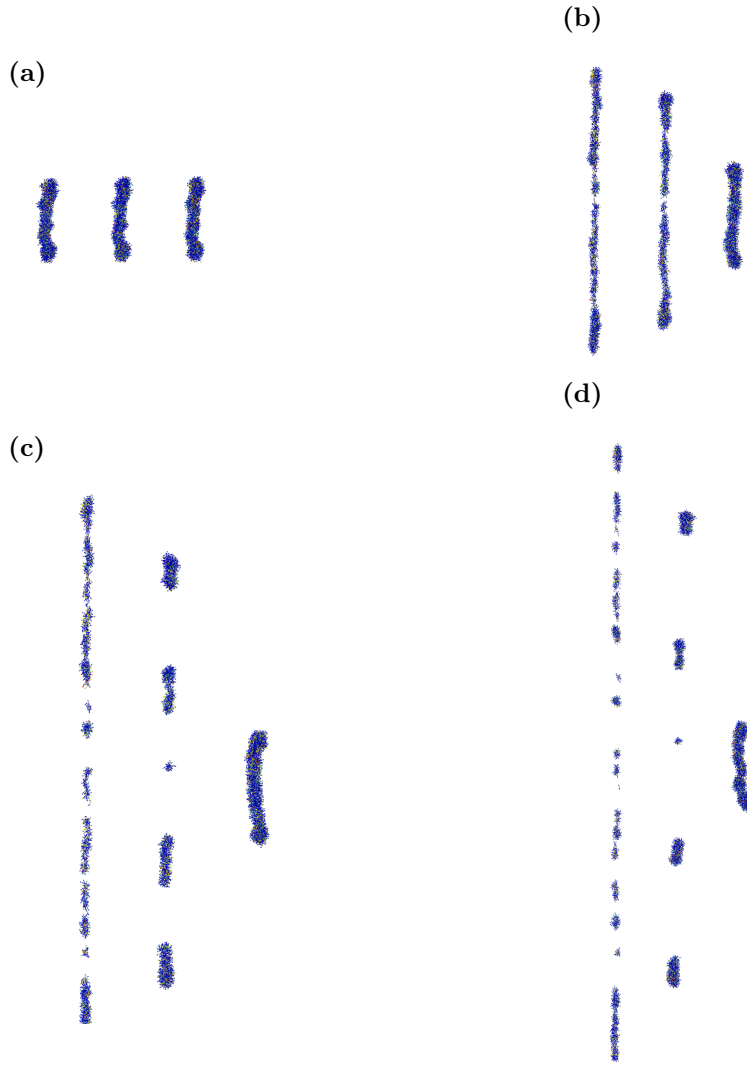
Figure 3.9: Worm-like micelle structures at accumulated strain of (a)0, (b)3, (c)6, and (d)9. In each image, the structure at $Wi \sim 30$ is depicted at the left; $Wi \sim 3$ in the middle; $Wi \sim 0.3$ at the right.

This disparity was more significant for moderate deformation rate and less significant in low and higher deformation rate. Analysis of the energy, presented in figs 3.11 and 3.15, obtained from normal- and parallel-direction flow revealed that the disparity in energy was primarily observed in the pair-wise potential energy as seen in figs 3.11 and 3.15. Furthermore, analysis of the radial distribution function showed disparity in the spatial distribution of polar and apolar micellar moieties. Essentially, parallel-direction flow resulted
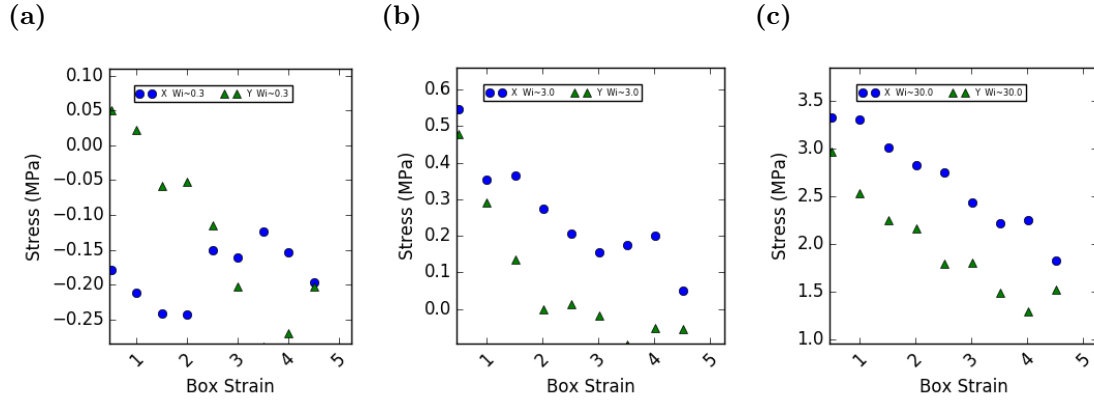
Figure 3.10: Effect of rod-like micellar orientation on stress response at (a)$Wi \sim 0.3$ (b)$Wi \sim 3$ (c)$Wi \sim 30$ in parallel (O) and normal ($\triangle$) direction deformation field with respect to micellar principal orientation.
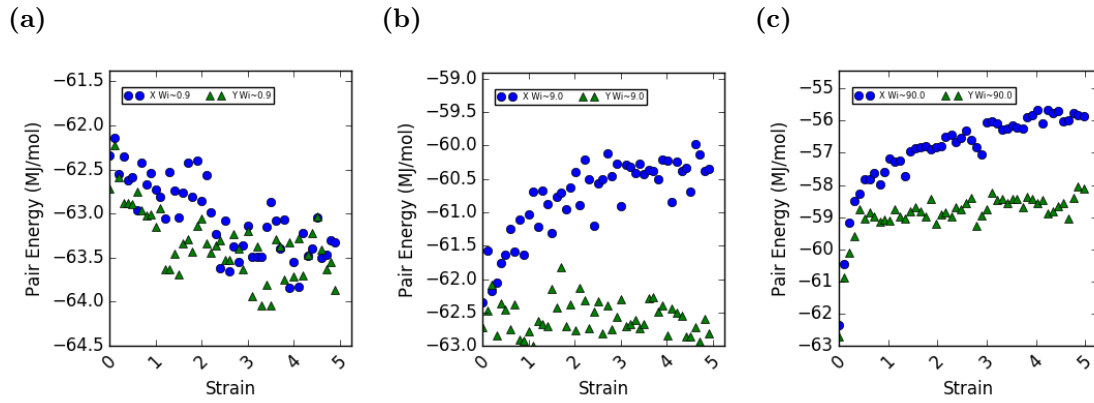
Figure 3.11: Effect of rod-like micellar orientation on pair-wise micellar energy at (a)$Wi \sim 0.3$ (b)$Wi \sim 3$ (c)$Wi \sim 30$ in parallel (O) and normal ($\triangle$) direction deformation field with respect to micellar principal orientation.

in greater development of non-favourable polar-apolar interactions compared with normal-direction flow as seen in figs. 3.13 to 3.12 and figs. 3.16 to 3.17. Since this disparity in stress and pair potential energy was absent in spherical micelles, it is proposed that the shape anisotropy is responsible for this. Specifically, in anisotropic structures, the micelle expends some added energy in performing flow-alignment. Thus whilst flow-alignment occurs, it is proposed that the parallel-and normal direction flow will show disparity and after flow alignment, this disparity will diminish. It is noteworthy that the

(a) **(b)** **(c)**
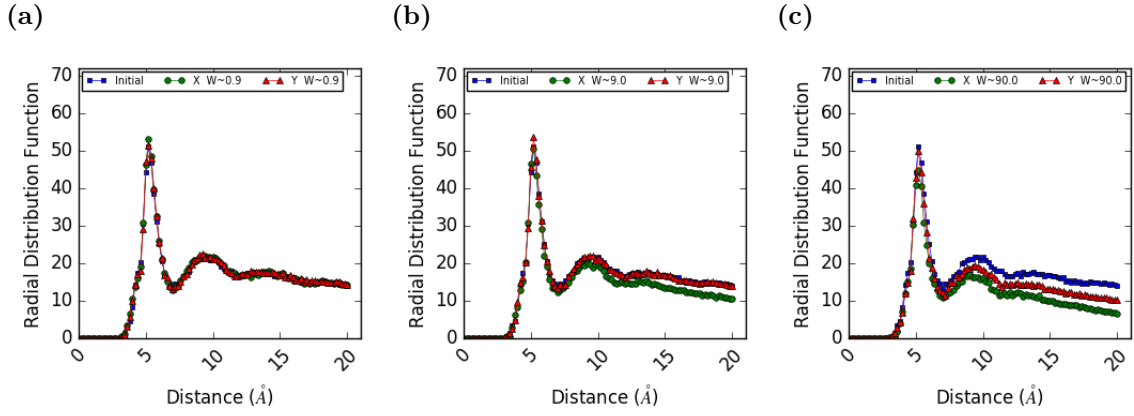
Figure 3.12: Effect of rod-like micellar orientation on apolar-apolar spatial distribution at (a)$Wi \sim 0.9$ (b)$Wi \sim 9$ (c)$Wi \sim 90$ in parallel (O) and normal ($\triangle$) direction deformation field with respect to micellar principal orientation.

(a) **(b)** **(c)**
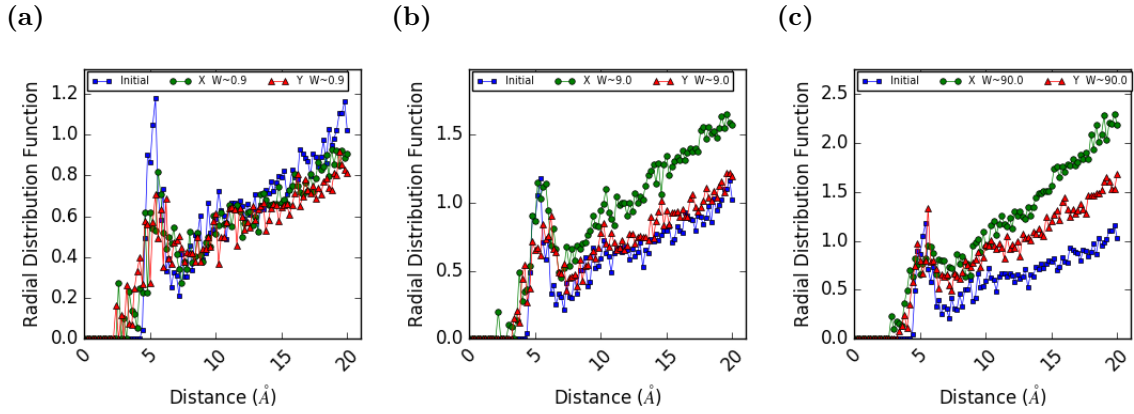
Figure 3.13: Effect of rod-like micellar orientation on apolar-polar spatial distribution at (a)$Wi \sim 0.9$ (b)$Wi \sim 9$ (c)$Wi \sim 90$ in parallel (O) and normal ($\triangle$) direction deformation field with respect to micellar principal orientation.

less significant disparity found in low deformation rate is thought to be due to effective relaxation that dissipates practically all excess applied energy to the system at that deformation rate. Similarly, the less significant disparity in stress at high deformation rate was a result of micellar ineffective relaxation before severe distortion to the micro-structure. Hypothetically, if the simulation is continued after complete alignment of the micelle to the direction of flow, similar distortions to the micro-structure should occur as was found in parallel-direction flow.
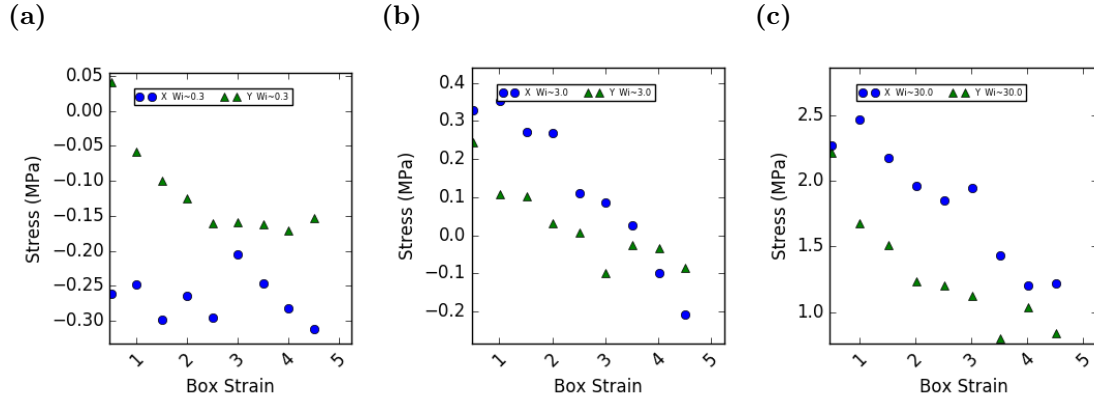
Figure 3.14: Effect of worm-like micellar orientation on stress response at (a)$Wi \sim 0.3$ (b)$Wi \sim 3$ (c)$Wi \sim 30$ in parallel (O) and normal ($\triangle$) direction deformation field with respect to micellar principal orientation.
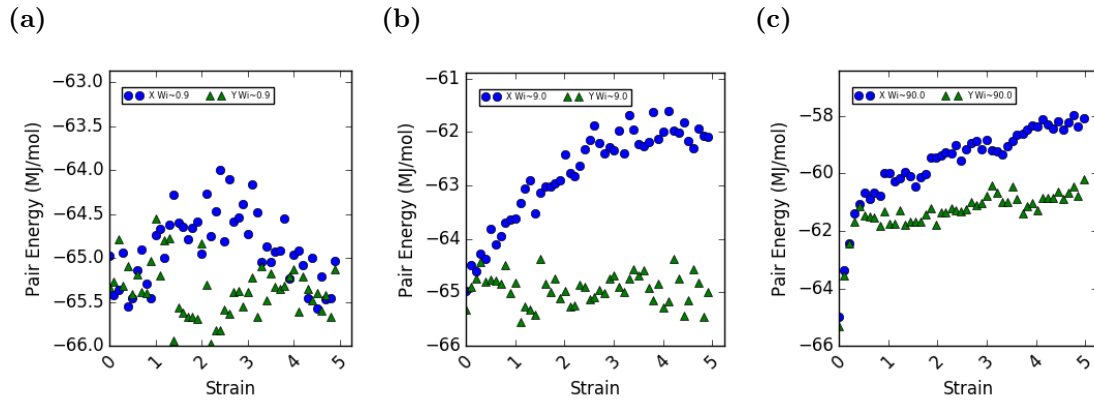
Figure 3.15: Effect of worm-like micellar orientation on pair-wise micellar energy at (a)$Wi \sim 0.3$ (b)$Wi \sim 3$ (c)$Wi \sim 30$ in parallel (O) and normal ($\triangle$) direction deformation field with respect to micellar principal orientation.

3.3.3 Stress and Structural Relaxation

The first observable difference in the micellar structure upon cessation of uniaxial deformation is the immediate re-orientation of surfactant molecules such that hydrophobic groups were shielded from entropically unfavourable interactions with the aqueous solution. Subsequently, micellar configuration was observed to be a function of the deformation rate and the total subjected strain. When the deformation rate was such that $Wi \sim 0.3$, no structural distortion was observed in the rod-like or worm-like micelle during uniaxial

65

(b) (c)
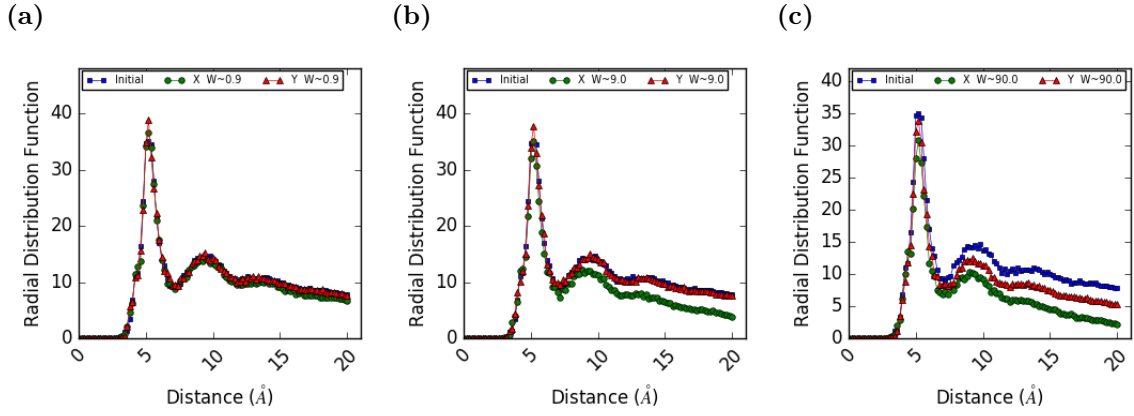
Figure 3.16: Effect of worm-like micellar orientation on apolar-apolar spatial distribution at (a)$Wi \sim 0.9$ (b)$Wi \sim 9$ (c)$Wi \sim 90$ in parallel (O) and normal ($\triangle$) direction deformation field with respect to micellar principal orientation.

(a) (b) (c)
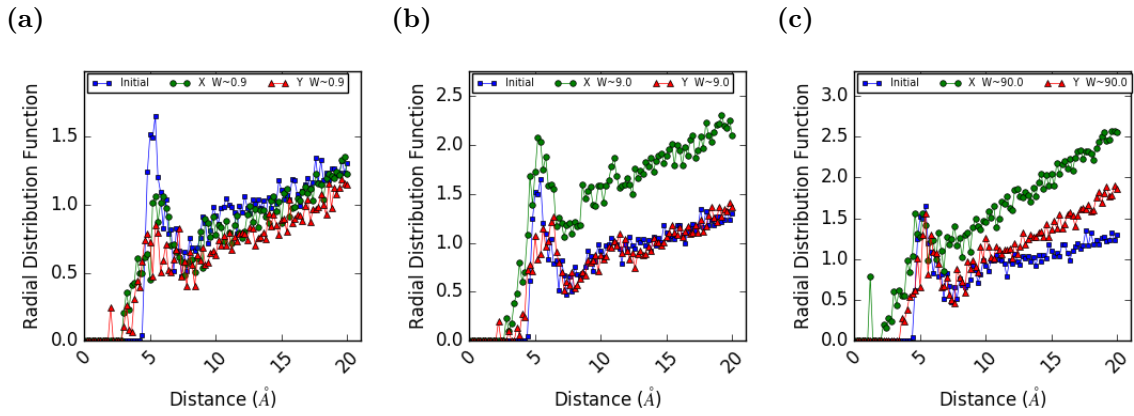
Figure 3.17: Effect of worm-like micellar orientation on apolar-polar spatial distribution at (a)$Wi \sim 0.9$ (b)$Wi \sim 9$ (c)$Wi \sim 90$ in parallel (O) and normal ($\triangle$) direction deformation field with respect to micellar principal orientation.

extensional flow, thus no recovery was evident.

When the deformation rate was comparable to the relaxation time, such that $Wi \sim 3$, rod-like micelle structural recovery was observed within ~ 8, ~ 30, and $\gg 50\lambda$ at accumulated strain values of 1, 3, and 5 respectively. In these cases, structural recovery was akin to elastic recovery after relief from strain. In case of an accumulated strain value of 5, rod-like micellar scission began was not concluded during uniaxial extension. When extension was discontinued, micellar scission continued and two child spherical micelles

were formed. Given sufficient time, it is theoretically possible for these child-micelles to recombine in a structure similar to the parent rod-like micelle. However, during the time frame of this experiment, the child-micelles did not recombine.

When the time-scale for deformation was shorter than the relaxation time such that $Wi \sim 30$, rod-like micelle structural recovery was observed within $\sim 15\lambda$ after being subjected to an accumulated strain of unity. After being subjected to an accumulated strain values of 3 and 5 at this deformation rate, rod-like micelle, (that was stretched but did not undergo scission during uniaxial deformation) underwent spontaneous micellar scission during relaxation and the number of resulting child micelles increased with accumulated strain. In this case, as before, it is theoretically possible for these child-micelles to recombine to form a structure similar to the parent-micelle. However, during the course of this experiment, these child-micelles did not undergo recombination.

The relaxation of worm-like micelles in parallel-direction flow bore several similarities with that of rod-like micelles. When non-severe micro-structure distortions and no micellar scission occurred, the micelle underwent elastic recovery. When more severe micro-structure distortion occurred, worm-like micelles were observed to undergo spontaneous scission (even when the structures did not undergo scission during extensional flow) and the number of

child-micelles increased with deformation rate and total subjected strain.

The relaxation of the rod-like micelle in normal-direction flow was similar to its response in parallel-direction flow. However, none of the structures obtained from normal-direction flow underwent spontaneous micellar scission during equilibrium simulation after deformation. This is thought to be due to the less severe micro-structure distortion done in normal-direction flow compared with parallel-direction flow.

Interestingly, worm-like micelle exposed to normal-direction flow relaxed into a structure similar to the initial structure at $Wi \leq 1$ and relaxed into a branched worm-like micelle at $Wi \sim 30$. This difference in the relaxed structure is possibly due to the differences in deformation pattern that occurred during uniaxial extensional. It is theoretically possible for the branched worm-like micelle to undergo structural transition to worm-like micelle similar to the parent micelle. However this did not occur during the time frame of this investigation.

Abrupt stress relaxation was observed in these cylindrical micellar systems upon cessation uniaxial extensional deformation. This stress decay was fitted to an exponential decay function with a relaxation time larger than the longest relaxation time of the micellar structure, presented in figs. 3.18 to 3.19. The exponential stress decay is proposed to be a result of the immediate re-alignment of deformed micellar structure to shield hydrophobic
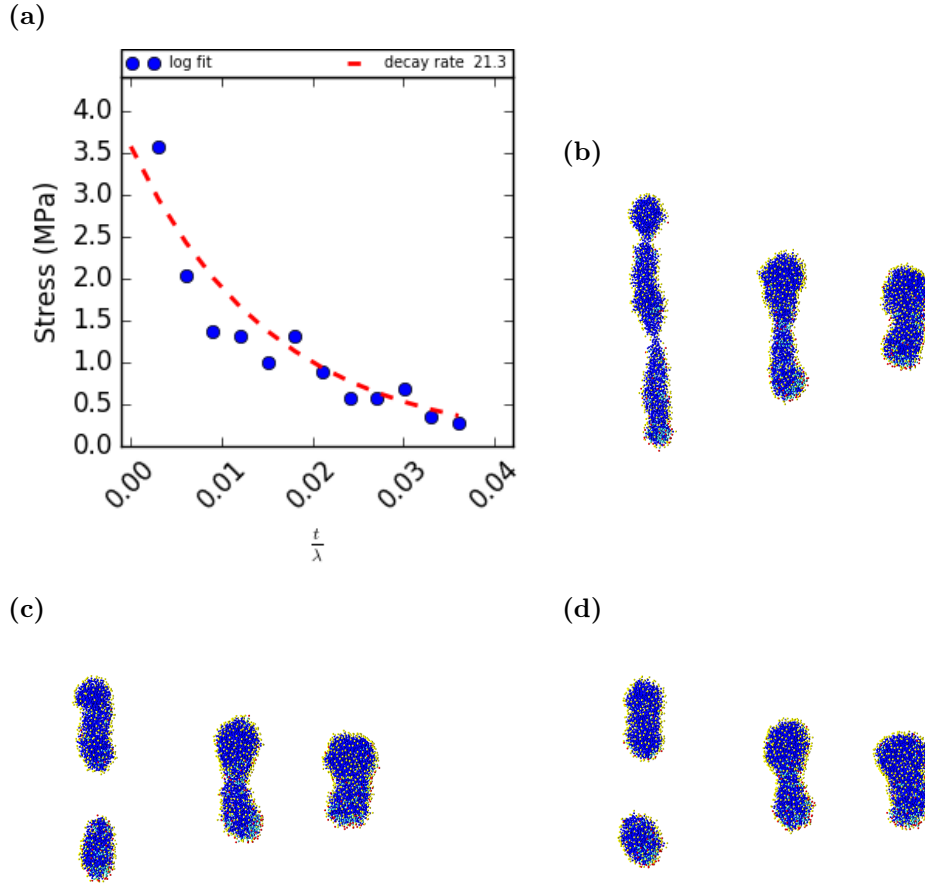
Figure 3.18: Rod-like micelle (a)stress and structure at (b)1λ (c)3λ (d)5λ upon cessation of uniaxial extensional deformation. In each image, the structure at $Wi \sim 30$ is depicted at the left; $Wi \sim 3$ in the middle; $Wi \sim 0.3$ at the right.

beads from solvent interactions. Experiments and Brownian dynamics simulations conducted in dilute polymer solutions also observed fast decay rate compared with the relaxation time.[80–83] This fast decay rate resulted in stress relaxation within fractions of the longest relaxation time of these micellar structures. This observation of a faster stress relaxation time agrees with the vast number of multi-mode stress relaxation models for soft matter. Analysis of the loading stress (i.e. the stress response when uniaxial extensional deformation was applied) and the unloading stress (i.e. the stress response in relaxation following uniaxial deformation) revealed a stress hys-

69
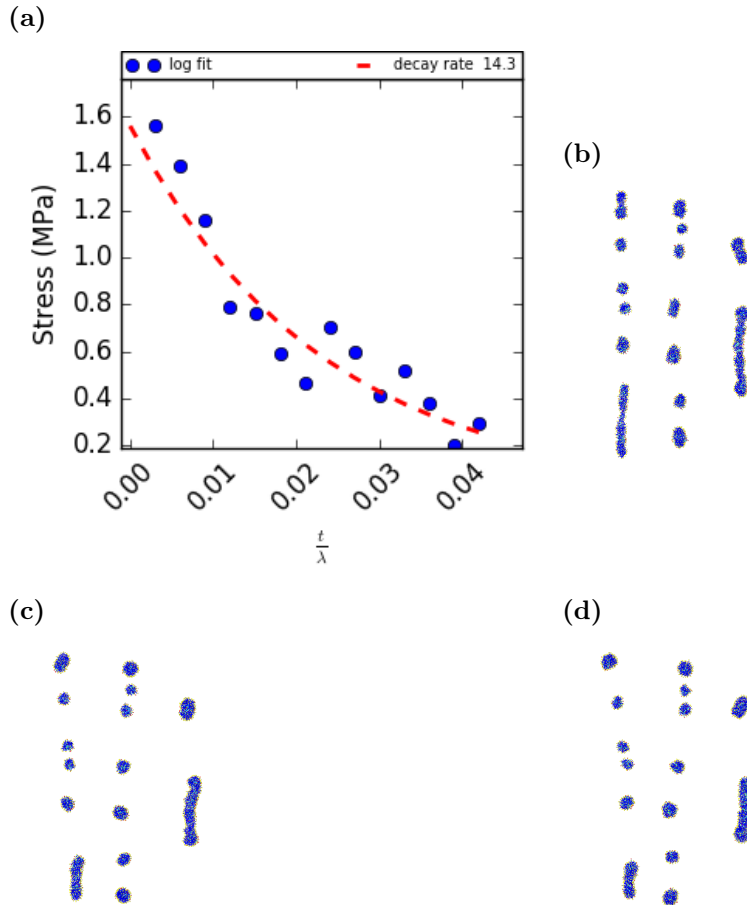
Figure 3.19: Worm-like micelle (a)stress and structure at (b)1λ (c)3λ (d)5λ upon cessation of uniaxial extensional deformation. In each image, the structure at $Wi \sim 30$ is depicted at the left; $Wi \sim 3$ in the middle; $Wi \sim 0.3$ at the right.

teresis that is analogous to the stress-birefringence hysteresis observed in dilute polymer solutions.[80–83] However, unlike polymer solutions, this hysteresis is proposed to be a result of the development of unfavourable interactions between polar and apolar moieties in the system. Specifically, abrupt stress decrease was observed in the systems at time-scales much shorter than the time required for structural recovery, as seen in figs. 3.18 to 3.19, because apolar moieties were abruptly shielded from unfavourable interactions with polar moieties.

This stress hysteresis appeared to grow with accumulated strain and the

deformation rate of the previous uniaxial extensional simulation as seen in figs. 3.20 to 3.21 in congruence with the finite extensible non-linear elastic (FENE) model. Loading and unloading stress hysteresis is thought to be a measure of the absorbed energy in the system. This increase in hysteresis with deformation rate and accumulated strain can be understood within this theory. At higher deformation rate, effective relaxation of the micelles whilst undergoing uniaxial deformation ensures that a significant fraction of the excess energy in the system is dissipated. Increasing deformation rate implies less effective stress relaxation. Therefore increasing deformation rate also implies less significant excess energy dissipation. This being the case, it is logical for a measure of the absorbed energy in the system, i.e. hysteresis, to increase with deformation rate. Along similar lines, we can explain the increase of hysteresis with accumulated strain. Larger values of accumulated strain implies larger time frame for uniaxial deformation and introduction of excess energy into the system. Thus, it is logical for hysteresis to increase with accumulated strain.

3.4   Conclusion

Uniaxial extension deformation was imposed on a system of solvated cylindrical micelles in directions parallel and normal to the micellar orientation. At

certain predefined deformation rates and accumulated strain, the structures were extracted, analysed and subjected to equilibrium simulation.

At low deformation rate and parallel-direction flow, these micelles underwent flow-induced translation, and axial perturbations as stress release mechanisms. As the time-scale of deformation shortened, these relaxation mechanisms became inefficient at relaxing the stress on the micelle causing microstructure distortions, micellar scission, decrease in entropy and increase in stress response. The child-micelles formed from the scission of worm-like micelles were of different lengths suggesting that micellar scission occurs randomly on the micellar contour length, as predicted by the mean field theory.

When the micelle was exposed to normal-direction flow, flow-alignment occurred as a potentially additional source of stress relaxation. On average, the stress response from normal-direction flow was lower than parallel-direction flow due to energy expended in undergo flow alignment. When complete flow alignment is achieved, it is proposed that the stress disparity in parallel- and normal deformation will be eliminated.

Micellar scission was observed to readily happen in relaxation following parallel-direction flow, unlike in normal-direction flow. When normal-direction flow was applied to the worm-like micelle system, structural transition to branched worm-like micelle occurred in relaxation after deformation at high

deformation rate. These child-micelles obtained can theoretically recombine to form a structure similar to the parent micelles, though this was not observed during the time frame of this investigation.

Micellar stress was observed to exponentially relax in these systems, similar to previous studies of dilute polymer solutions. The decay rate of this exponential function was found to be larger than the longest relaxation time of this micelle, enabling the micelle to relax in a fraction of its relaxation time. Hysteresis in the loading and unloading stress was observed to increase with deformation rate and accumulated strain.

Figure 3.20: Loading (O) and unloading (△) stress hysteresis at (a)$Wi \sim 0.9$, (b)$Wi \sim 9$, and (c)$Wi \sim 90$. (d)Area under the loading-unloading curve of rod-like micelle as a function of accumulated strain.

74

(a)

(b)

(c)

(d)
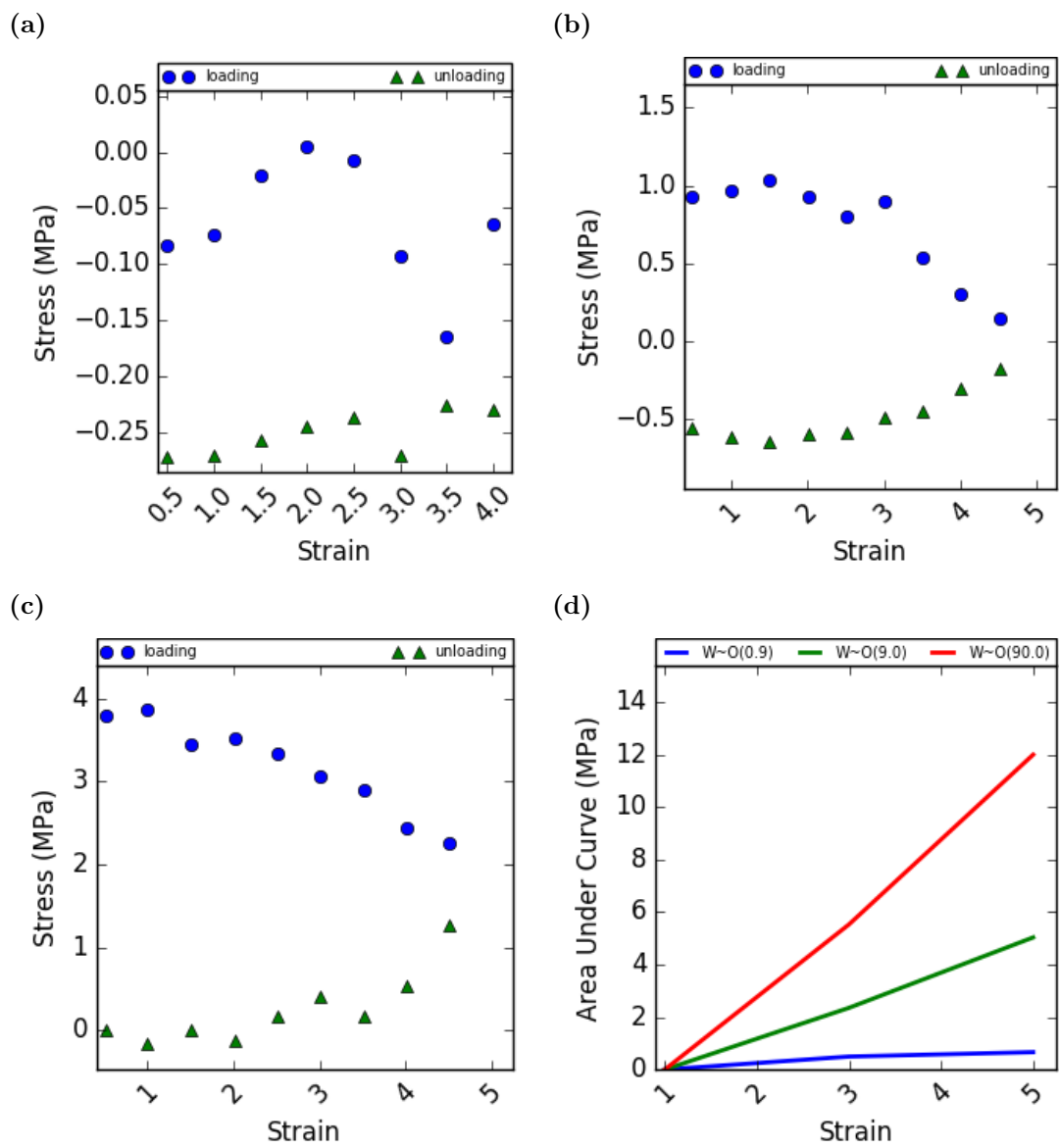
Figure 3.21: Loading (O) and unloading ($\triangle$) stress hysteresis at (a)$Wi \sim 0.9$, (b)$Wi \sim 9$, and (c)$Wi \sim 90$. (d)Area under the loading-unloading curve of worm-like micelle as a function of accumulated strain.

Chapter 4

Dynamics of a Branched Micelle

4.1   Introduction

Structures formed by the spontaneous self-assembly of surfactant molecules have garnered significant interest in the scientific community because of their vast potential industrial and commercial applications. Worm-like micellar structures are of particular interest to the scientific community because of their ability to introduce significant viscoelasticity to solutions.[2,19,21] Analogy has been found between worm-like micellar and polymer solutions in that reptation is a significant stress release mechanism in both systems. However, unlike polymers, worm-like micelles exist in a dynamic equilibrium of continuous scission and recombination that introduces an additional stress release mechanism. Essentially, reptation dominates in worm-like micellar solutions when its time-scale is shorter than that of scission, while scission dominates when the converse is true. Systems of branched worm-like micelles have been observed to be more fluid than entangled worm-like micellar solutions and this has been theorised to result from branch sliding, or ghost-like crossings along the contour length of the micelle. These differences in stress relaxation

is manifested in solutions of ionic surfactants with binding counter-ion salts where non-monotonic dependence and double viscosity peaks were observed as salt concentration was changed. The first viscosity peak was associated with worm-like micellar growth, the first trough was associated with branching of the worm-like micelles that introduced additional fluidity to the system, and the second peak was associated with the formation of entangled multi-connected networks of worm-like micelles. These results have also been confirmed using coarse-grained molecular dynamics simulations.[68]

Though extensive work has been done in understanding micellar dynamics in viscoelastic solutions,[99,105,118–129,129–136] there exists a gap in the understanding of micellar dynamics in dilute solutions where viscoelasticity is non-applicable. Experimental methods can be limited by their inability to observe and quantify interactions between atoms at significant length- and time-scale that can bring clarity to the structure and consequent dynamics of micellar systems. To this effect, molecular dynamics simulation methods have been developed to take a closer look and complement the insight obtained from experimental studies on molecular systems. Recently, coarse-grained molecular dynamics (CGMD) systems have been used to model aqueous solutions of Cetyl trimethyl ammonium chloride (CTAC) and Sodium Salicylate (NaSal) and it has quite reliably modelled: the phenomenon of micellization;[4] micellar growth, transition, scission, and recombi-

nation;[9] changes in CTAC micellar structure with increase in NaSal concentration and the consequent non-monotonic dependence of solution zero-shear viscosity on mole ratio of NaSal to CTAC;[11] relationship between shear rate, tumbling frequency and orientation dynamics in simple shear flow that is in good agreement with mesoscopic theories;[67] and micellar mid-plane thinning and scission in solutions of rod-like micelles that are in good agreement with elastocapillary thinning of a viscoelastic fluid.[68] Using the insightful CGMD tool, this work investigates the dynamics and stress relaxation mechanisms of systems consisting of a single branched worm-like micelle in aqueous solution under uniaxial extensional flow field.

4.2 Simulation Details

In this study, self-assembled solutions were formed by solvating previously formed branched worm-like micelle[137–143] in water. The pre-formed branched worm-like were molecular models of salicylate anion and cetyltrimethylammonium cation according to the Martini forcefield formalism.[76] In line with the Martini force field formalism, water was modelled as bead type P4; with additional 10% of bead type BP4 to prevent unnatural freezing of water at room temperature and pressure. BP4 and P4 bead types have same interaction parameter values, save the P4-BP4 interaction. Sodium ion was

modelled as bead type Qd, chloride ion was modelled as bead type Qa; salicylate anion was modelled as a chain with 1 hydrophilic bead and 3-ring hydrophobic beads, making a total of 4 beads. The hydrophilic bead was modelled as Martini bead type Qd, while the hydrophobes were modelled as bead type SC4. Cetyltrimethylammonium cation was modelled as a 5-bead chain with 1 hydrophilic bead and 4 hydrophobic beads. The hydrophilic bead was modelled as Martini bead type Q0, while the hydrophobic beads where modelled as bead types C1, and C2. Other details of the particle definition are presented in table tables 4.1 to 4.5.

Table 4.1: Branched worm-like micelle particle types.

Index	Martini Bead Type	Atoms	Charge
Cetyltrimethylammonium cation			
1	Q0	CH_2-CH_2-N^+-C_3H_9	1
2	C2	C_3H_6	0
3	C2	C_3H_6	0
3	C2	C_4H_8	0
3	C2	C_4H_9	0
Salicylate anion			
1	Qa	C-OO^-	-1

Index	Martini Bead Type	Atoms	Charge
Continuation of Table 4.1			
2	SC4	C_2-OH	0
3	SC4	C_2H_2	0
4	SC4	C_2H_2	0
Sodium ion			
1	Qd	Na^+	1
Chloride ion			
1	Qa	Cl^-	-1
Water			
1	P4	$4H_2O$	0
Anti-freeze water			
1	BP4	$4H_2O$	0

Table 4.2: Branched worm-like micelle angle interaction parameters.

i	j	k	Angle(degrees)	Force Constant($kJ/_{mol \cdot nm^2}$)
Cetyltrimethylammonium cation				

i	j	k	Angle(degrees)	Force Constant($kJ/mol \cdot nm^2$)
			Continuation of Table 4.2	
1	2	3	180	25
2	3	4	180	25
3	4	5	180	25
4	5	6	180	25
			Salicylate anion	
1	2	3	150	25
1	2	4	150	25
2	3	4	60	25
3	4	2	60	25
4	2	3	60	25

Table 4.3: Branched worm-like micelle bond interaction parameters.

i	j	Bond length(nm)	Force Constant(kJ/mol)
		Cetyltrimethylammonium cation	
1	2	0.47	1250

		Continuation of Table 4.3	
i	j	Bond length(nm)	Force Constant(kJ/mol)
2	3	0.47	1250
3	4	0.47	1250
4	5	0.47	1250
		Salicylate anion	
1	2	0.47	1250
2	3	0.33	20000
2	4	0.33	20000
3	4	0.33	20000

Table 4.4: Branched worm-like micelle Lennard Jones pair-wise interaction parameters.

Interacting pair	$\epsilon_{ij}(kJ/mol)$	$\sigma_{ij}(nm)$
P4 - BP4	5.6	0.57
P4 - P4	5.0	0.47
P4 - Qa	5.6	0.47
P4 - Q0	5.6	0.47
P4 - Qd	5.6	0.47

Continuation of Table 4.4		
Interacting pair	$\epsilon_{ij}(^{kJ}/_{mol})$	$\sigma_{ij}(nm)$
P4 - C1	2.0	0.47
P4 - C2	2.3	0.47
P4 - SC4	2.7	0.47
Qa - Qa	5.0	0.47
Qa - Q0	4.5	0.47
Qa - Qd	5.6	0.47
Qa - C1	2.0	0.62
Qa - C2	2.0	0.62
Qa - SC4	2.7	0.47
Q0 - Q0	3.5	0.47
Q0 - Qd	4.5	0.47
Q0 - C1	2.0	0.62
Q0 - C2	2.0	0.62
Q0 - SC4	2.7	0.47
Qd - Qd	5.0	0.47

Continuation of Table 4.4		
Interacting pair	$\epsilon_{ij}(kJ/mol)$	$\sigma_{ij}(nm)$
Qd - C1	2.0	0.62
Qd - C2	2.0	0.62
Qd - SC4	2.7	0.47
C1 - C1	3.5	0.47
C1 - C2	3.5	0.47
C1 - SC4	3.1	0.47
C2 - C2	3.5	0.47
C2 - SC4	3.1	0.47
SC4 - SC4	3.5	0.43

Table 4.5: Branched worm-like micelle simulation box details.

System Information	Value
Water beads	675000
Anti-freeze water beads	67500
Salicylate beads	882
Sodium beads	882

Continuation of Table 4.5	
System Information	Value
Cetyltrimethylammonium beads	242
Chloride beads	242
Micelle dimension	33.7nm $\times$ 17.5nm $\times$ 8.7nm
Box size	36.4nm $\times$ 75.3nm $\times$ 43.2nm

Equilibrium and extensional molecular dynamics simulations were carried out using the LAMMPS[77–79] package. During equilibrium simulations, NPT ensemble at 300K and 1 atm was obtained using the Nose Hoover thermostat and barostat. The gyration tensor $\underline{\underline{G}}$ was calculated from the coordinates obtained during equilibrium simulations, such that

$$G_{i,j} = \frac{1}{N} \sum_{k=1}^{N} (r_i^k - r_i^{cm})(r_j^k - r_j^{cm}), \tag{4.1}$$

where N is the number of particles in the self-assembled structures, r_i is the x, y, or z coordinate of a particle in the self-assembled structures, and r_i^{cm} is the centre of mass of the x, y or z coordinate. A characteristic time-scale for this structure is obtained from the autocorrelation of the eigen vector of the largest eigen value of the gyration tensor. This characteristic time was

estimated to be 4ns as seen in fig 4.1.

(a)
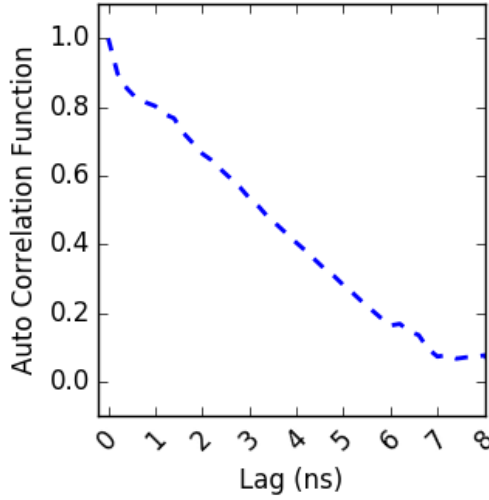
Figure 4.1: Autocorrelation function of (a)branched worm-like micellar orientation.

In non-equilibrium simulations, the system was kept at 300K. The flow direction underwent uniaxial extension at predefined extensional rates while the compression directions were maintained at 1 atm. In constructing the simulation system, the principal orientation axis of the self-assembled structure was the X direction such that uniaxial extension applied in the X and Y directions will be parallel and normal to the principal orientation axis of the structure. Extensional deformations were carried out in X and Y directions at $Wi \sim 0.3, 0.9, 3, 9, 30, 90$ until an accumulated strain of 10 units. Care was specifically taken to ensure the box dimensions were large enough to prevent interactions between particles and their periodic image during the course of the simulation. After accumulated strains values of 1, 3, and 5; the coordinates of the particles in these systems were extracted and equilib-

rium simulations were performed to observe stress and structural relaxation following uniaxial extensional deformation.

4.3   Results and Discussion

4.3.1   Effect of Deformation Rate on Dynamics of Branched Worm-like Micelle

The dynamics and stress response of this system was observed to depend on the deformation rate. When the deformation rate was such that $Wi \sim 0.3$, branch sliding was observed. This is in agreement with theories,[2] and other computer simulations.[11,144]   During the course of this investigation, flow induced branch sliding caused structural transition from branched to simple worm-like micelle. Axial perturbation and flow-induced translation was also observed in this micellar dynamics. At this low deformation rate, sufficient micellar relaxation can occur during deformation to prevent significant distortion of micellar micro-structure and the development of unfavourable polar-apolar interactions that decreases entropy of the system, as seen in figs. 4.2 to 4.4.

Micellar scission is thought to result from relatively non-homogeneous counter-ion translation during deformation that cause local ion depletion in regions and local high-energy regions within the micellar contour length, resulting in

increased susceptibility to scission.[68] Micellar axial and contour length perturbations are proposed to be responsible for stress distribution along the micellar contour that neutralised local high energy regions along the micellar contour length, hence reducing the incidence of micellar scission at this deformation rate.

(a) (b)
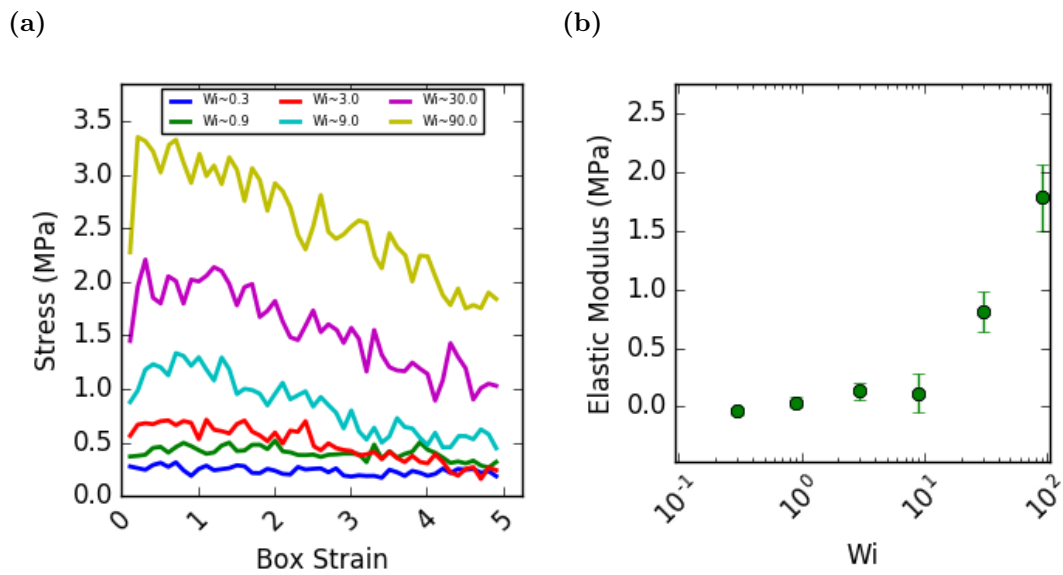
Figure 4.2: Effect of Wi on (a)stress and (b)elastic modulus of branched worm-like micelle.

(a) (b)
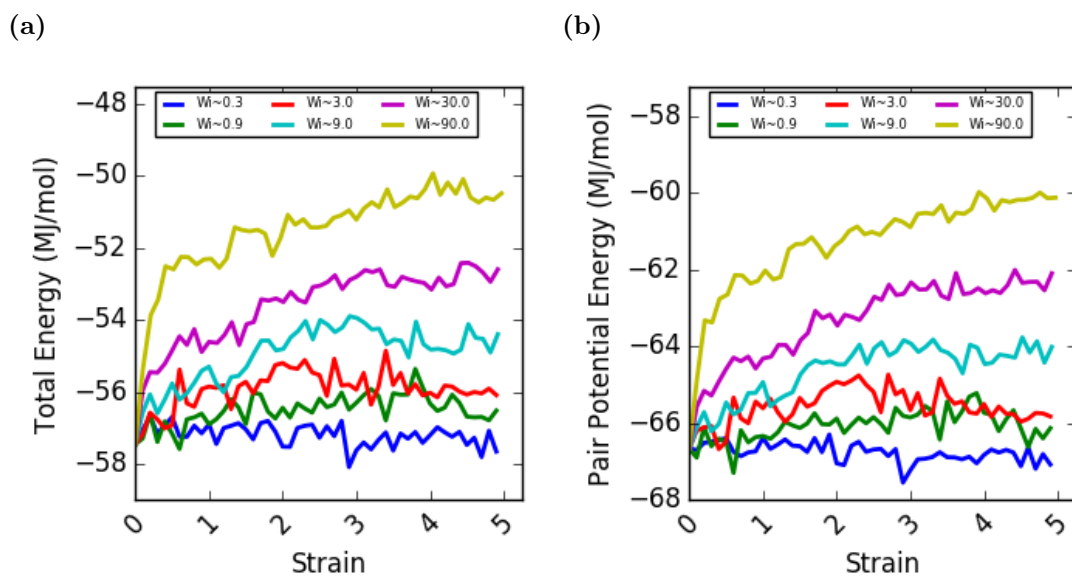
Figure 4.3: Effect of Wi on (a)total and (b)pair-wise potential energy of branched worm-like micelle.
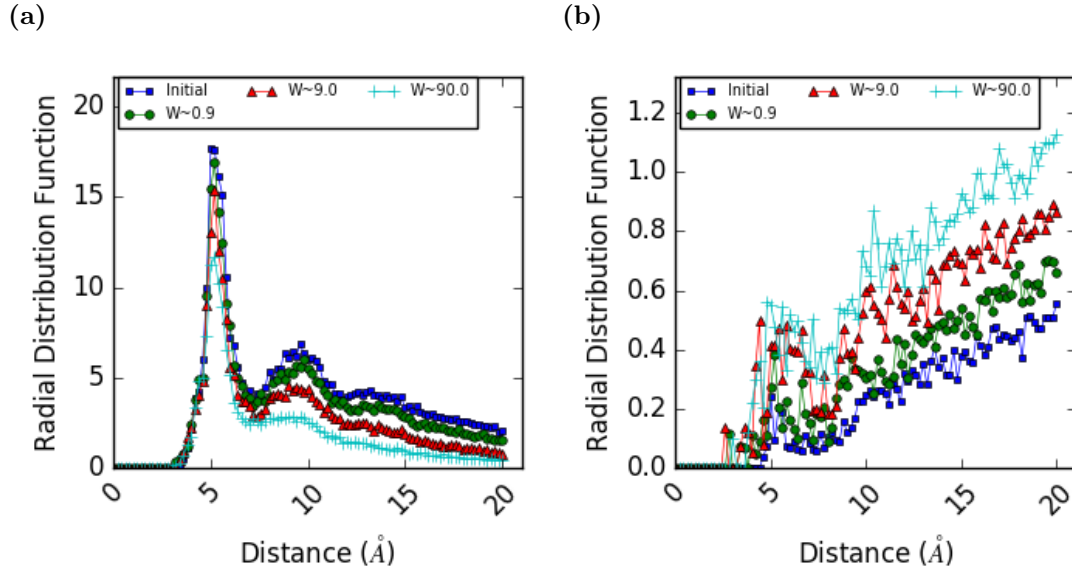
Figure 4.4: Effect of Wi on g(r) of (a)apolar-apolar and (b)apolar-polar branched worm-like micelle moieties after accumulated strain of 5 at equilibrium ($\square$), $Wi \sim 0.9$ (O), $Wi \sim 9$ ($\triangle$), and $Wi \sim 90$ (+).

When the time scale of deformation rate was on the same order as the micellar longest relaxation time (i.e. $Wi \sim 3$), this branched micelle was stretched in the direction of flow. This is because the heightened rate of deformation did not afford the micelle sufficient time to relax whilst undergoing uniaxial deformation. This diminished ability to relax caused significant distortion in the micro-structure that led to the development of unfavourable polar-apolar interactions. Development of unfavourable interactions caused decrease in the entropy of the system and increased stress response as seen in fig 4.5. Particularly, the ineffectiveness of axial perturbations, resulted in development of local regions of high energy that encouraged micellar scission along the micellar contour. After micellar scission, the child-micelles continued to undergo flow-induced translation. Though further scission of the child-micelles

were not observed in this experiment, they are theoretically possible if the child-micelles develop local high-energy regions that make micellar scission energetically favourable.
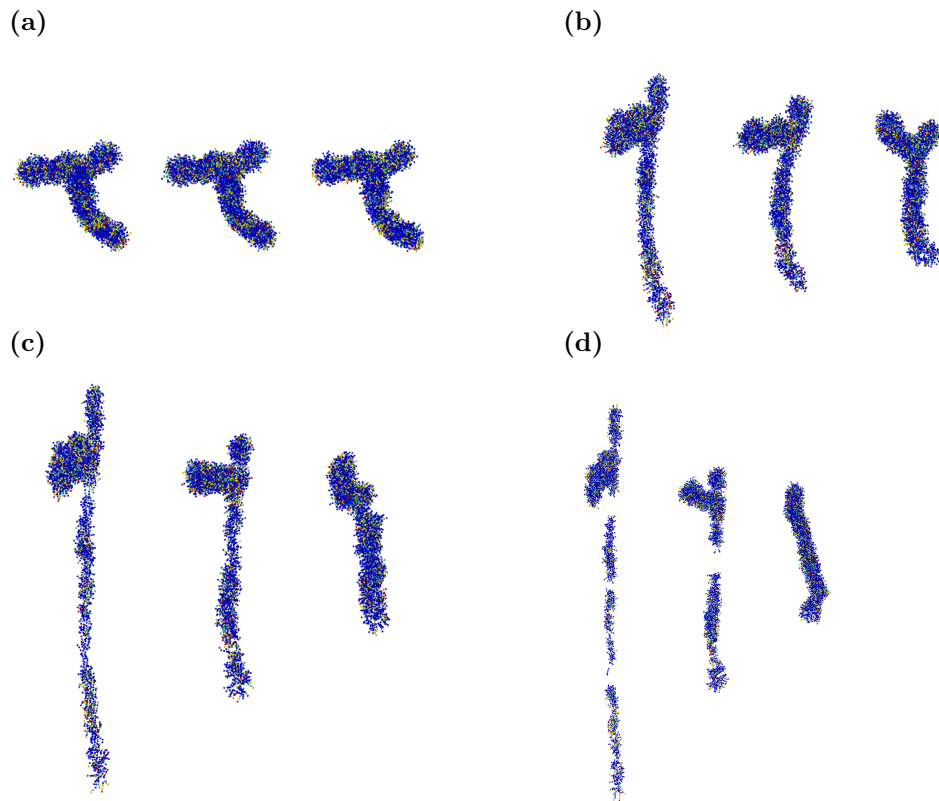
Figure 4.5: Branched worm-like micelle structures at accumulated strain of (a)0, (b)2, (c)4, and (d)6. In each image, the structure at $Wi \sim 30$ is depicted at the left; $Wi \sim 3$ in the middle; $Wi \sim 0.3$ at the right.

When the deformation rate occurred at a time-scale that was shorter than the relaxation time, (i.e. $Wi \sim 30$), severe distortions were done to the micellar structure, resulting in development of interactions between incompatible pairs, and the consequent decrease in micellar entropy. This decrease in entropy is manifested in the significantly higher stress response presented in fig 4.2.

The analysis of the elastic modulus, shown in fig 4.2, typifies the trend of stress response as a function of deformation rate. When the deformation rate was low and the micelle had sufficient time to relax during the deformation, a more solid-like response was observed. However, increasing deformation rate till its time-scale becomes comparable with the time-scale of relaxation caused a more liquid response from these micellar systems.

4.3.2   Effect of Orientation on Dynamics

Branched worm-like are anisotropic in shape. Thus, significant differences between the structural and stress response were expected between flow parallel (henceforth called parallel-direction flow) and normal (henceforth called normal-direction flow) to the micellar orientation. The findings obtained from this investigation were generally in agreement with this presumption. At low deformation rate, branch sliding, flow-induced translation, and axial perturbations were observed in these systems. However, unlike parallel-direction flow, flow-alignment was also observed in these systems. As a result of the efficient stress release mechanisms at this deformation rate, excess energy applied to these systems at this deformation rate were neutralised, thereby preventing micro-structure distortion and micellar scission. As the deformation rate was increased, the branched worm-like micelle was less efficient at neutralising excess energy, resulting in more significant micro-

structure distortions and micellar scission.
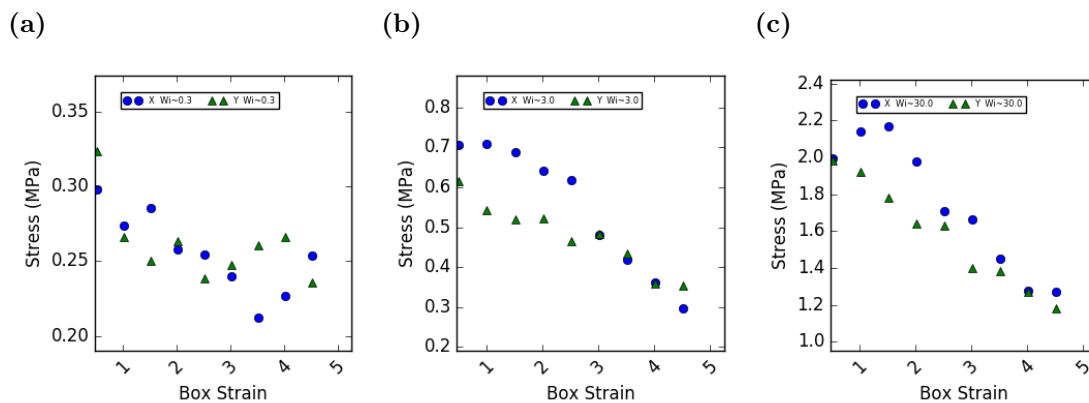
Figure 4.6: Effect of branched worm-like micellar orientation on stress response at (a)$Wi \sim 0.3$ (b)$Wi \sim 3$ (c)$Wi \sim 30$ in parallel (O) and normal ($\triangle$) direction deformation field with respect to micellar principal orientation.
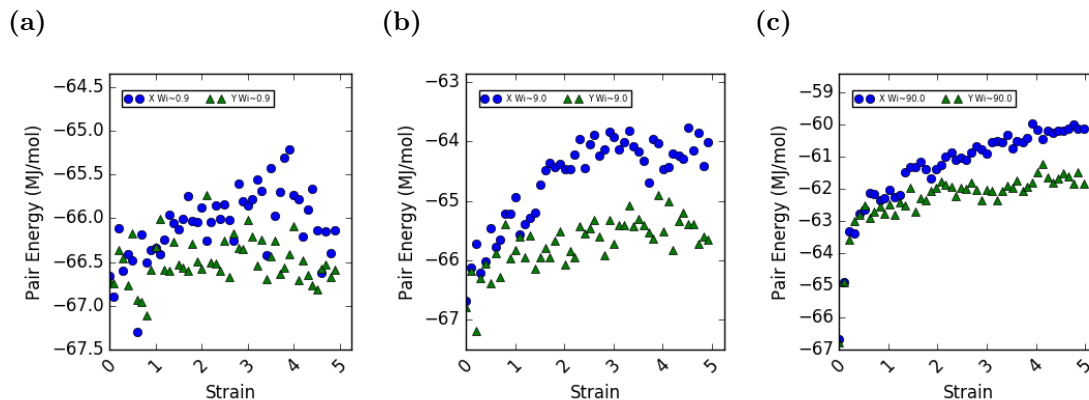
Figure 4.7: Effect of branched worm-like micellar orientation on pair-wise micellar energy at (a)$Wi \sim 0.3$ (b)$Wi \sim 3$ (c)$Wi \sim 30$ in parallel (O) and normal ($\triangle$) direction deformation field with respect to micellar principal orientation.

The analysis of the stress response showed some variations between normal-direction and parallel-direction flow, as shown in 4.6. In normal-direction flow, low and high deformation rate showed less disparity in stress while moderate deformation rate showed larger stress disparity. Similar disparity with deformation direction were also observed in total and pair-wise interaction potential energy as well as the spatial distribution of the micellar

92
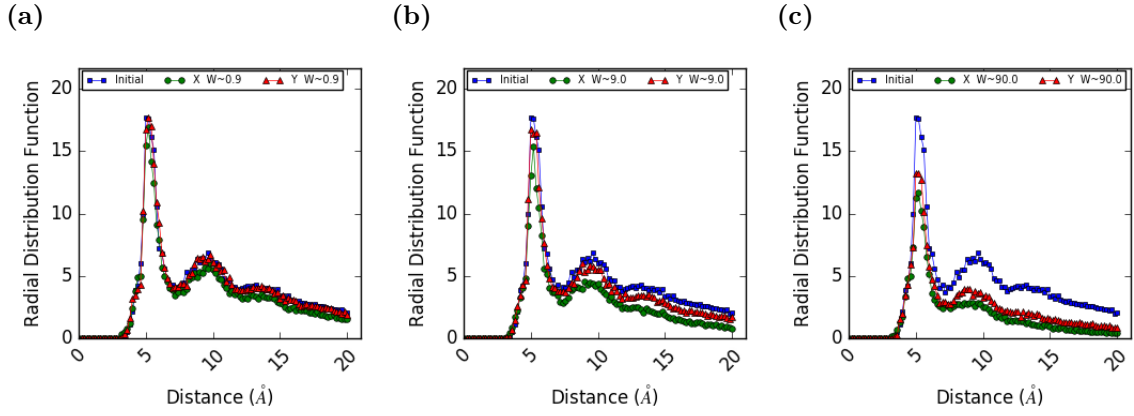
Figure 4.8: Effect of branched worm-like micellar orientation on apolar-apolar spatial distribution at (a)$Wi \sim 0.9$ (b)$Wi \sim 9$ (c)$Wi \sim 90$ in parallel (O) and normal ($\triangle$) direction deformation field with respect to micellar principal orientation.
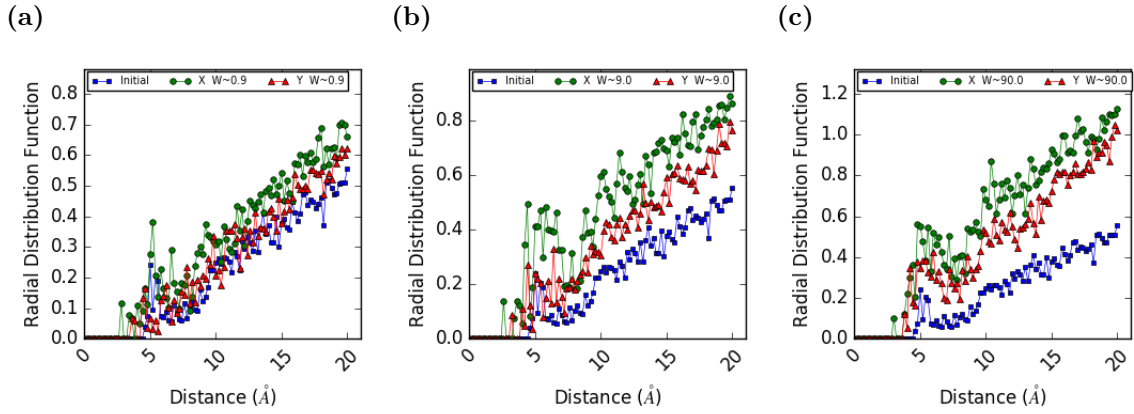
Figure 4.9: Effect of branched worm-like micellar orientation on apolar-polar spatial distribution at (a)$Wi \sim 0.9$ (b)$Wi \sim 9$ (c)$Wi \sim 90$ in parallel (O) and normal ($\triangle$) direction deformation field with respect to micellar principal orientation.

moieties, as seen in figs. 4.8 to 4.9.

This disparity can be explained by the fact that at moderate deformation rate, flow alignment occurs in normal-direction flow unlike parallel-direction flow. This flow alignment dissipates some of the excess energy added into the system by uniaxial deformation. Thus, for the same deformation rate, less significant distortion occurs in normal-direction flow compared with parallel-direction flow. The unobservable disparity at low deformation rate is proposed to be due to very effective stress and excess energy dissipation by the

stress release mechanisms. Whilst the reduced disparity in high deformation rate is proposed to be due to fast deformation that prevents effective relaxation and flow-alignment before significant micro-structure distortion. When complete flow alignment occurs in moderate deformation rates, elimination of the observed disparity is anticipated.

4.3.3 Stress and Structural Relaxation

Upon cessation of uniaxial extensional deformation, abrupt re-orientation of hydrophobic beads, such that they were shielded from unfavourable interactions with water, occurred. Furthermore, when the structure had not undergone scission or transition to simple worm-like micelle, structure recoverability was possible during relaxation after extensional flow in all extensional rates investigated.

When $Wi \sim 0.3$ and sufficient accumulated strain has elapsed for structural transition to occur, the newly formed simple worm-like micelle persisted during equilibrium following extensional flow. When $Wi \geq O(1)$ and sufficient time had elapsed for micellar scission to occur, the resulting child-micelles relaxed into spherical and short worm-like micelles. The number of child-micelles obtained from the relaxation of the parent micelle in grew with the deformation rate and the accumulated strain at the time of observation. Excluding the situation where uniaxial extension were discontinued before
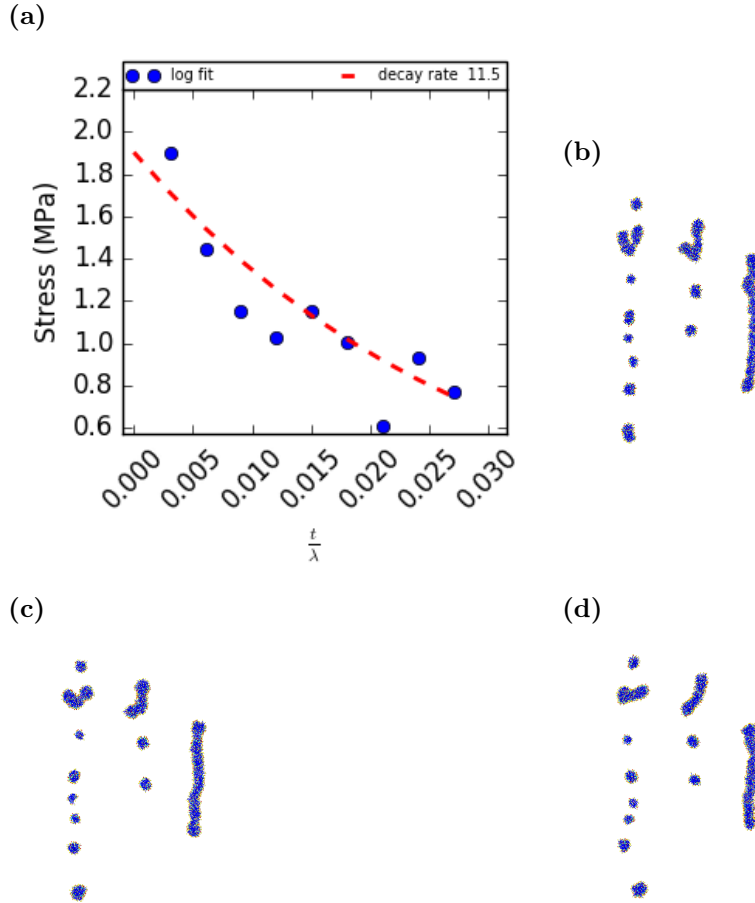
Figure 4.10: Branched worm-like micelle (a)stress and structure at (b)1λ (c)3λ (d)5λ upon cessation of uniaxial extensional deformation. In each image, the structure at $Wi \sim 30$ is depicted at the left; $Wi \sim 3$ in the middle; $Wi \sim 0.3$ at the right.

scission or structural transition, recovery of the initial structure was not observed in the time frame of investigation, though it is theoretical possible given sufficient time. Similar results were also obtained for normal-direction flow as well.

Similar to dilute polymer solutions,[80–83] Stress relaxation following uniaxial extensional flow was found to undergo exponential decay as seen in fig 4.10. The decay rate was larger than the longest relaxation time of this micellar structure. This resulted in the stress relaxation fractions of the micellar longest relaxation time. This observation agrees with multi-mode

stress relaxation models of complex fluids.
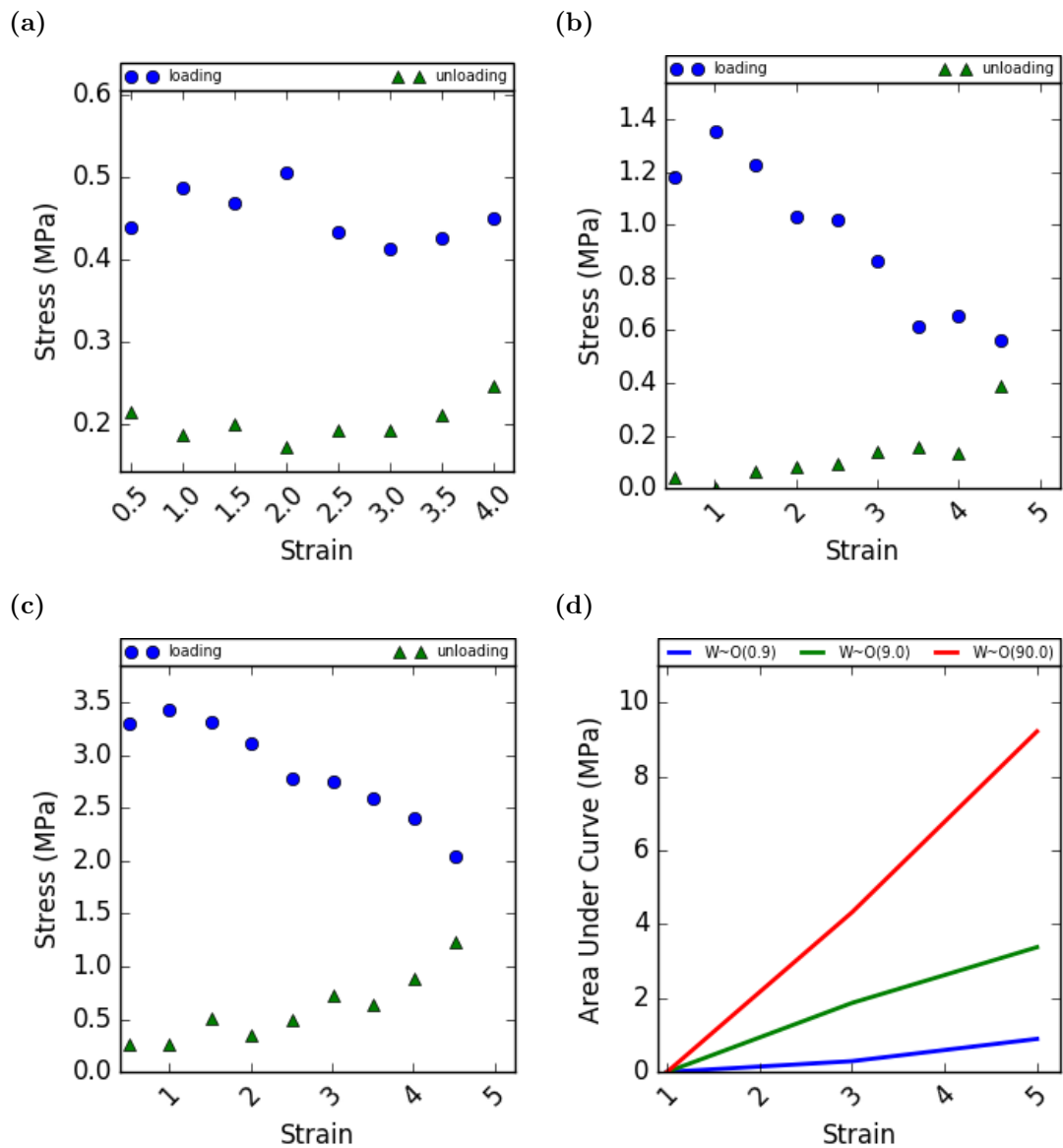
Figure 4.11: Loading (O) and unloading ($\triangle$) stress hysteresis at (a)$Wi \sim 0.9$, (b)$Wi \sim 9$, and (c)$Wi \sim 90$. (d)Area under the loading-unloading curve of branched worm-like micelle as a function of accumulated strain.

In congruence with the predictions of the finite extensible non-linear elastic (FENE) model, and the observations of dilute polymer solutions,[80–83] hysteresis was noticed in the loading stress (i.e. the stress response when uniaxial extensional deformation was applied) and the unloading stress (i.e. the

96

stress response in relaxation following uniaxial deformation) was observed. In this solution, the hysteresis is thought to be a caused by the development of unfavourable interactions between polar and apolar moieties. The abrupt stress relaxation that occurred before structural recovery, as seen in fig 4.10, supports this hypothesis that hysteresis in micellar systems are linked to particle interactions as opposed to structural evolution during loading and unloading.

Furthermore, stress hysteresis was observed to grow with accumulated strain and deformation rate as seen in fig 4.11. Stress hysteresis is thought to be related to the energy absorbed by the complex fluid. Along the lines of this hypothesis, increase of hysteresis with rate of deformation and total accumulated strain can be explained. Increased accumulated strain implies a greater time frame for addition of excess energy via uniaxial extension. Similarly, the increase of stress hysteresis with deformation rate can be understood to be due to less effective micellar stress relaxation and energy dissipation whilst undergoing uniaxial extensional deformation.

4.4 Conclusion

Branched micellar systems were subjected to uniaxial extensional deformation in directions normal and parallel to its orientation. In both normal- and

97

parallel-direction flow, branch sliding, micellar drift in flow direction, flow alignment and axial perturbations were observed at low deformation rate. These stress relaxation mechanisms effectively neutralised the stress along the micellar contour length such that micellar scission was not observed. The sliding of branches resulted in structural transition from branched to simple worm-like micelles.

As deformation rate increased, the stress relaxation mechanisms became less effective at neutralising the excess applied energy to the system and micellar scission occurred. At even higher deformation rates, severe micro-structure distortion occurred that encouraged interactions between incompatible moieties in the system, giving rise to lower entropy and higher stress response. Some excess energy applied to the system during normal-direction flow was expended in flow-alignment. Thus, the distortion of the micro-structure was less severe and caused decreased development of solvent-solvophobic interactions, lower entropy change, and lower stress response compared with parallel-direction flow.

When the simple micelle formed from branch sliding was relaxed after deformation, it persisted during the time frame of this investigation. When the child-micelles formed from the scission were relaxed, they also persisted. These structures could potentially undergo recombination and transformation into structures similar to the parent micelle, given sufficient time.

Stress was observed to exponentially relax with a deformation rate that was greater than the micellar relaxation time; causing stress relaxation within a time frame shorter than the longest relaxation time of the micelle. Hysteresis in the loading and unloading stress was observed to increase with accumulated strain and deformation rate.

Chapter 5

Summary and Future Outlook

5.1   Introduction

Surfactants are surface active molecules that promote miscibility; and reduce excess energy at interfaces of otherwise immiscible fluids.[3–11]   They are characterised by solvophilic and solvophobic moieties that spontaneously self-assemble at a surfactant-specific concentration, called the critical micellar concentration, into structures that are generally called micelles. This self-assembly process is entropically driven and aimed at mitigating unfavourable solvent-solvophobic interactions, while simultaneously minimizing steric and/or electrostatic intra-micellar repulsions. Micellar structures consist of a solvophobic core and a solvophilic crown that encompasses the core.

In aqueous/polar solutions, micellar structures are typically characterised by non-ionic, cationic, anionic, or zwitterionic hydrophilic/lipophobic crowns and hydrophobic/lipophilic cores. In apolar solutions, micellar structures, typically called reverse micelles, consist of lipophilic crowns and lipophobic cores. Micellar structures have found applications in hydrotropy, biomimet-

ics, dispersion and emulsification, enhanced oil recovery,[12] detergency, templating, drug delivery, personal care products, drag reduction,[13] nanoscale reaction vessels, therapeutic gene delivery, bio-catalysis and so on.

Despite the tremendous progress in understanding the underlying mechanisms behind micellar dynamics and kinetics, experimental methods can be limited by their inability probe, observe and quantify interactions in molecular systems with accuracy at the length and time scale of molecular processes. To this effect, several molecular dynamics simulation methods have been developed to complement the insight obtained from experimental studies on molecular systems. Utilising coarse-grained molecular dynamics, this study is aimed at simulating different micellar systems with the purpose of understanding the dynamics, stress and structural response to uniaxial extensional flow field.

5.2   Dynamics Of a Spherical Vesicle

In Chapter 2, uniaxial extension deformation was imposed on a system consisting of solvated spherical vesicle. At certain predefined deformation rates and accumulated strain, the structures were extracted, analysed and subjected to equilibrium simulation for the observation of stress and structural relaxation.

At low deformation rate, this vesicle was observed to undergo flow-induced translation (with no observable perturbations to its aspect ratio) as its predominant stress release mechanism. At deformation occurring at a time-scale comparable to the relaxation time, distortions to the aspect ratio were observed. At deformation rates with time-scale much shorter than relaxation time, significant distortions were observed in the vesicular micro-structure. The vesicle was observed to be particularly "resistant" to scission and it was suggested that its shape isotropy aided in the distribution of stress across the vesicular surface area, making it easy to neutralise local build up of stress that has been known to cause vesicular scission. The orientation of deformation was observed to have insignificant impact to vesicular stress, dynamics and structural response to uniaxial deformation. This is proposed to be due to the uniformity of its aspect ratio.

Spherical vesicles were also found to readily relax with the initial decay matching an exponential function. The exponential decay rate was found to be greater than the longest relaxation time of the vesicle, resulting in stress relaxation in fractions of the longest relaxation time. Hysteresis in the loading and unloading stress was observed to increase with the rate of deformation and total accumulated strain.

In all investigated deformation rates and accumulated strain, structural recovery in relaxation following uniaxial extensional deformation was achieved.

These characteristics of spherical vesicles make them particularly suited for nano-carrier applications, such as in drug delivery.

5.3 Dynamics Of Cylindrical Micelles

In Chapter 3, uniaxial extension deformation was imposed on a system of solvated cylindrical micelles in directions parallel and normal to the micellar orientation. At certain predefined deformation rates and accumulated strain, the structures were extracted, analysed and subjected to equilibrium simulation.

At low deformation rate and parallel-direction flow, these micelles underwent flow-induced translation, and axial perturbations as stress release mechanisms. As the time-scale of deformation shortened, these relaxation mechanisms became inefficient at relaxing the stress on the micelle causing microstructure distortions, micellar scission, decrease in entropy and increase in stress response. The child-micelles formed from the scission of worm-like micelles were of different lengths suggesting that micellar scission occurs randomly on the micellar contour length, as predicted by the mean field theory.

When the micelle was exposed to normal-direction flow, flow-alignment occurred as a potentially additional source of stress relaxation. On average, the

stress response from normal-direction flow was lower than parallel-direction flow due to energy expended in undergo flow alignment. When complete flow alignment is achieved, it is proposed that the stress disparity in parallel- and normal deformation will be eliminated.

Micellar scission was observed to readily happen in relaxation following parallel-direction flow, unlike in normal-direction flow. When normal-direction flow was applied to the worm-like micelle system, structural transition to branched worm-like micelle occurred in relaxation after deformation at high deformation rate. These child-micelles obtained can theoretically recombine to form a structure similar to the parent micelles, though this was not observed during the time frame of this investigation.

Micellar stress was observed to exponentially relax in these systems, similar to previous studies of dilute polymer solutions. The decay rate of this exponential function was found to be larger than the longest relaxation time of this micelle, enabling the micelle to relax in a fraction of its relaxation time. Hysteresis in the loading and unloading stress was observed to increase with deformation rate and accumulated strain.

5.4 Dynamics Of a Branched Worm-like Micelle

In Chapter 4, branched micellar systems were subjected to uniaxial extensional deformation in directions normal and parallel to its orientation. In both normal- and parallel-direction flow, branch sliding, micellar drift in flow direction, flow alignment and axial perturbations were observed at low deformation rate. These stress relaxation mechanisms effectively neutralised the stress along the micellar contour length such that micellar scission was not observed. The sliding of branches resulted in structural transition from branched to simple worm-like micelles.

As deformation rate increased, the stress relaxation mechanisms became less effective at neutralising the excess applied energy to the system and micellar scission occurred. At even higher deformation rates, severe micro-structure distortion occurred that encouraged interactions between incompatible moieties in the system, giving rise to lower entropy and higher stress response. Some excess energy applied to the system during normal-direction flow was expended in flow-alignment. Thus, the distortion of the micro-structure was less severe and caused decreased development of solvent-solvophobic interactions, lower entropy change, and lower stress response compared with parallel-direction flow.

When the simple micelle formed from branch sliding was relaxed after de-

formation, it persisted during the time frame of this investigation. When the child-micelles formed from the scission were relaxed, they also persisted. These structures could potentially undergo recombination and transformation into structures similar to the parent micelle, given sufficient time. Stress was observed to exponentially relax with a deformation rate that was greater than the micellar relaxation time; causing stress relaxation within a time frame shorter than the longest relaxation time of the micelle. Hysteresis in the loading and unloading stress was observed to increase with accumulated strain and deformation rate.

5.5   Future Outlook

In this dissertation, the response of a spherical vesicle was simulated in aqueous solution because nano-carriers for targeted drug delivery is an emerging use for spherical vesicles. As a simplistic first step, the vesicle was simulated in water since blood contains a high volume fraction of water. However, in the nano-scale, blood contains several dissolved solids, electrolytes and nano-particles. These blood constituents may potentially interact with the spherical vesicle and affect its dynamics, structure and stress response under uniaxial extensional flow. In order to have a more realistic understanding of micellar dynamics and structural configuration under uniaxial extensional

106

flow, more realistic systems than the simplistic systems found in this study could be done.

Furthermore, this dissertation studied the dynamics of cylindrical and branched worm-like micelles under extensional flow applied in a direction parallel (parallel-direction flow) and normal (normal-direction flow) to the orientation of each micellar structure. However, these simulations were done in infinitely dilute systems. To further improve this body of knowledge, the changes in structure, dynamics and stress release mechanisms could be investigated as a function of increasing concentration.

In these cylindrical systems, flow-induced translation and axial perturbations were observed to be a dominant stress release mechanism. However normal-direction flow was observed to have a stress and structural disparity compared with parallel-direction flow. The dependence of the orientation on micellar rheological and structural characteristics has not been fully explored. Though it is proposed that the disparity in stress, energy and spatial distribution will be eliminated once flow alignment is completed, this can potentially be further studied and confirmed.

Finally, for completeness, the structural and rheological characteristics of each micelle under tangential deformation can be explored and compared with the characteristics under extensional deformation.

Bibliography

[1] Malinda Salim, Hiroyuki Minamikawa, Akihiko Sugimura, and Rauzah Hashim. Amphiphilic designer nano-carriers for controlled release: from drug delivery to diagnostics. *Med. Chem. Commun.*, 5:1602–1618, 2014.

[2] H. Rehage and H. Hoffmann. Rheological properties of viscoelastic surfactant systems. *The Journal of Physical Chemistry*, 92(16):4712–4719, 1988.

[3] P. Debye and E. Anacker. Micelle shape from dissymmetry measurements. *J. Phys. Chem.*, 55:644, 1951.

[4] Ashish V. Sangwai and Radhakrishna Sureshkumar. Binary interactions and salt-induced coalescence of spherical micelles of cationic surfactants from molecular dynamics simulations. *Langmuir*, 28(2):1127–1135, 2012. PMID: 22149605.

[5] X. Tang, P. H. Koenig, and R. G. Larson. Molecular dynamics simulations of sodium dodecyl sulfate micelles in water- the effect of the force field. *J. Phys. Chem. B*, 118:3864, 2014.

[6] A. Sambasivam, A. V. Sangwai, and R. Sureshkumar. Dynamics and

scission of rodlike cationic surfactant micelles in shear flow. *Phys. Rev. Lett.*, 114:158302, 2015.

[7] D. Gaudino, R. Pasquino, and N. Grizzuti. Adding salt to a surfactant solution: Linear rheological response of the resulting morphologies. *J. Rheol. (Melville, NY, U. S.)*, 59:1363, 2015.

[8] M. A. Calabrese, S. A. Rogers, R. P. Murphy, and N. J. Wagner. The rheology and microstructure of branched micelles under shear. *J. Rheol. (Melville, NY, U. S.)*, 59:1299, 2015.

[9] Ashish V. Sangwai and Radhakrishna Sureshkumar. Coarse-grained molecular dynamics simulations of the sphere to rod transition in surfactant micelles. *Langmuir*, 27(11):6628–6638, 2011. PMID: 21524093.

[10] D. Danino, Y. Talmon, H. Levy, G. Beinert, and R. Zana. Branched threadlike micelles in an aqueous solution of a trimeric surfactant. *Science*, 269:1420, 1995.

[11] S. Dhakal and R. Sureshkumar. Topology, length scales and energetics of surfactant micelles. *J. Chem. Phys.*, 143:024905, 2015.

[12] E. S. Boek, A. Jusufi, H. Lowen, and G. C. Maitland. *J. Phys.: Condens. Matter*, 14:9413, 2002.

[13] R. K. Rodrigues, M. A. da Silva, and E. Sabadini. *Langmuir*, 24:13875, 2008.

[14] Charles Tanford. *The hydrophobic effect: formation of micelles and biological membranes.* New York: John Wiley Sons, 1973.

[15] R. Nagarajan. Molecular packing parameter and surfactant self-assembly: the neglected role of the surfactant tail. *Langmuir*, 18(1):31–38, 2002.

[16] J. Israelachvili, D. J. Mitchell, and B. W. Ninham. *J. Chem. Soc., Faraday Trans. 2*, 72:1525, 1976.

[17] M.E. Cates. Dynamics of living polymers and flexible surfactant micelles : scaling laws for dilution. *J. Phys. France*, 49(9):1593–1600, 1988.

[18] Safran, S.A., Pincus, P.A., Cates, M. E., and MacKintosh, F.C. Growth of charged micelles. *J. Phys. France*, 51(6):503–510, 1990.

[19] Koos Bijma and Jan B. F. N. Engberts. Effect of counterions on properties of micelles formed by alkylpyridinium surfactants. 1. conductometry and 1h-nmr chemical shifts. *Langmuir*, 13(18):4843–4849, 1997.

[20] Zuowei Wang and Ronald G. Larson. Molecular dynamics simulations of threadlike cetyltrimethylammonium chloride micelles: Effects of sodium chloride and sodium salicylate salts. *The Journal of Physical Chemistry B*, 113(42):13697–13710, 2009. PMID: 19476369.

[21] A. Khatory, F. Kern, F. Lequeux, J. Appell, G. Porte, N. Morie, A. Ott, and W. Urbach. Entangled versus multiconnected network of wormlike micelles. *Langmuir*, 9(4):933–939, 1993.

[22] Bernard J. Meister. Uniting molecular network theory and reptation theory to predict the rheological behavior of entangled linear polymers. *Macromolecules*, 22(9):3611–3619, 1989.

[23] Arkady L. Kholodenko. Reptation theory: geometrical and topological aspects. *Macromolecular Theory and Simulations*, 5(6):1031–1064.

[24] F. Lequeux. Reptation of connected wormlike micelles. *EPL (Europhysics Letters)*, 19(8):675, 1992.

[25] Ya Zhao, Simon J. Haward, and Amy Q. Shen. Rheological characterizations of wormlike micellar solutions containing cationic surfactant and anionic hydrotropic salt. *Journal of Rheology*, 59(5):1229–1259, 2015.

[26] P. Debye and E. Anacker. *J. Phys. Chem.*, 55:644, 1951.

[27] D. Danino, Y. Talmon, H. Levy, G. Beinert, and R. Zana. *Science*, 269:1420, 1995.

[28] F. Lequeux. *Curr. Opin. Colloid Interface Sci.*, 1:341, 1996.

[29] M. E. Cates and S. J. Candau. *J. Phys.: Condens. Matter*, 2:6869, 1990.

[30] P. A. Vasquez, G. H. McKinley, and L. P. Cook. *J. Non-Newtonian Fluid Mech.*, 144:122, 2007.

[31] V. Entov and E. Hinch. *J. Non-Newtonian Fluid Mech.*, 72:31, 1997.

[32] H. Sim, B. Khomami, and R. Sureshkumar. *J. Rheol. (Melville, NY, U. S.)*, 51:1223, 2007.

[33] A. Groisman and V. Steinberg. *Nature*, 405:53, 2000.

[34] S. J. Haward, T. J. Ober, M. S. Oliveira, M. A. Alves, and G. H. McKinley. *Soft Matter*, 8:536, 2012.

[35] D. Sachsenheimer, C. Oelschlaeger, S. Müller, J. Küstner, S. Bindgen, and N. Willenbacher. *J. Rheol.*, 58:2017, 2014.

[36] A. Bhardwaj, E. Miller, and J. P. Rothstein. *J. Rheol. (Melville, NY, U. S.)*, 51:693, 2007.

[37] P. S. Doyle, E. S. Shaqfeh, G. H. McKinley, and S. H. Spiegelberg. *J. Non-Newtonian Fluid Mech.*, 76:79, 1998.

[38] A. Noy and R. Golestanian. *Phys. Rev. Lett.*, 109:228101, 2012.

[39] E. Hinch. *J. Non-Newtonian Fluid Mech.*, 54:209, 1994.

[40] P. De Gennes. *J. Chem. Phys.*, 60:5030, 1974.

[41] D. E. Smith and S. Chu. *Science*, 281:1335, 1998.

[42] R. Larson, H. Hu, D. Smith, and S. Chu. *J. Rheol. (Melville, NY, U. S.)*, 43:267, 1999.

[43] C. M. Schroeder, H. P. Babcock, E. S. Shaqfeh, and S. Chu. *Science*, 301:1515, 2003.

[44] C. M. Schroeder, E. S. Shaqfeh, and S. Chu. *Macromolecules*, 37:9242, 2004.

[45] T. Sridhar, D. Nguyen, R. Prabhakar, and J. R. Prakash. *Phys. Rev. Lett.*, 98:167801, 2007.

[46] T. T. Perkins, D. E. Smith, and S. Chu. *Science*, 276:2016, 1997.

[47] R. M. Elder and A. Jayaraman. *Mol. Simul.*, 38:793, 2012.

[48] T. Odijk. *Macromolecules*, 28:7016, 1995.

[49] J. F. Marko and E. D. Siggia. *Macromolecules*, 28:8759, 1995.

[50] Annika Vogt, Christian Wischke, Axel T. Neffe, Nan Ma, Ulrike Alexiev, and Andreas Lendlein. Nanocarriers for drug delivery into and through the skin — do existing technologies match clinical challenges? *Journal of Controlled Release*, 242:3 – 15, 2016. International Conference on Dermal Drug Delivery by Nanocarriers, Berlin 14-16 March.

[51] Svetlana Gelperina. *Nanocarriers and Drug Delivery*, pages 163–179. Humana Press, Totowa, NJ, 2007.

[52] Mengrui Liu, Hongliang Du, Wenjia Zhang, and Guangxi Zhai. Internal stimuli-responsive nanocarriers for drug delivery: Design strategies and applications. *Materials Science and Engineering: C*, 71:1267 – 1280, 2017.

[53] Srinivas Ganta, Harikrishna Devalapally, Aliasgar Shahiwala, and Mansoor Amiji. A review of stimuli-responsive nanocarriers for drug and gene delivery. *Journal of Controlled Release*, 126(3):187 – 204, 2008.

[54] Doungporn Yiamsawas, Sebastian J. Beckers, Hao Lu, Katharina Landfester, and Frederik R. Wurm. Morphology-controlled synthesis of lignin nanocarriers for drug delivery and carbon materials. *ACS Biomaterials Science & Engineering*, 3(10):2375–2383, 2017.

[55] Wei Cui, Junbai Li, and Gero Decher. Selfassembled smart nanocarriers for targeted drug delivery. *Advanced Materials*, 28(6):1302–1311.

[56] Nobuhiro Nishiyama and Kazunori Kataoka. Current state, achievements, and future prospects of polymeric micelles as nanocarriers for drug and gene delivery. *Pharmacology Therapeutics*, 112(3):630 – 648, 2006.

[57] V. P. Torchilin. Micellar nanocarriers: Pharmaceutical perspectives. *Pharmaceutical Research*, 24(1):1, Nov 2006.

[58] Dan Peer, Jeffrey M. Karp, Seungpyo Hong, Omid C. Farokhzad, Rimona Margalit, and Robert Langer. Nanocarriers as an emerging platform for cancer therapy. *Nature Nanotechnology*, 2(12):751–760, 12 2007.

[59] Yasuhiro Matsumura. Poly (amino acid) micelle nanocarriers in preclinical and clinical studies. *Advanced Drug Delivery Reviews*, 60(8):899 – 914, 2008. Clinical Developments in Drug Delivery Nanotechnology.

[60] Xiaoqiang Yang, Jamison J. Grailer, Srikanth Pilla, Douglas A. Steeber, and Shaoqin Gong. Tumor-targeting, ph-responsive, and stable unimolecular micelles as drug nanocarriers for targeted cancer therapy. *Bioconjugate Chemistry*, 21(3):496–504, 2010. PMID: 20163170.

[61] Yan Lee, Takehiko Ishii, Horacio Cabral, HyunJin Kim, JiHun Seo, Nobuhiro Nishiyama, Hiroki Oshima, Kensuke Osada, and Kazunori Kataoka. Chargeconversional polyionic complex micelles—efficient nanocarriers for protein delivery into cytoplasm. *Angewandte Chemie*, 121(29):5413–5416.

[62] Zhonggao Gao, Anatoly N. Lukyanov, Anurag Singhal, and Vladimir P. Torchilin. Diacyllipid-polymer micelles as nanocarriers for poorly soluble anticancer drugs. *Nano Letters*, 2(9):979–982, 2002.

[63] Ludmila O. Cinteza, Tymish Y. Ohulchanskyy, Yudhisthira Sahoo, Earl J.

Bergey, Ravindra K. Pandey, and Paras N. Prasad. Diacyllipid micelle-based nanocarrier for magnetically guided delivery of drugs in photodynamic therapy. *Molecular Pharmaceutics*, 3(4):415–423, 2006. PMID: 16889435.

[64] Elena V. Batrakova and Alexander V. Kabanov. Pluronic block copolymers: Evolution of drug delivery concept from inert nanocarriers to biological response modifiers. *Journal of Controlled Release*, 130(2):98 – 106, 2008.

[65] MARY P. WIEDEMAN. Dimensions of blood vessels from distributing artery to collecting vein. *Circulation Research*, 12(4):375–378, 1963.

[66] Mukund Vasudevan, Eric Buse, Donglai Lu, Hare Krishna, Ramki Kalyanaraman, Amy Q. Shen, Bamin Khomami, and Radhakrishna Sureshkumar. Irreversible nanogel formation in surfactant solutions by microporous flow. *Nature Materials*, 9:436, 2010.

[67] Abhinanden Sambasivam, Ashish. V. Sangwai, and Radhakrishna Sureshkumar. Self-assembly of nanoparticle–surfactant complexes with rodlike micelles: A molecular dynamics study. *Langmuir*, 32(5):1214–1219, 2016. PMID: 26760445.

[68] Subas Dhakal and Radhakrishna Sureshkumar. Uniaxial extension of sur-

factant micelles: Counterion mediated chain stiffening and a mechanism of rupture by flow-induced energy redistribution. *ACS Macro Letters*, 5(1):108–111, 2016.

[69] H. J. C. Berendsen, D. Van Der Spoel, and R. Van Drunen. Gromacs: A message-passing parallel molecular dynamics implementation. *Comp. Phys. Comm*, 91:43–56, 1995.

[70] Mark James Abraham, Teemu Murtola, Roland Schulz, Szilard Pall, Jeremy C. Smith, Berk Hess, and Erik Lindahl. Gromacs: High performance molecular simulations through multi-level parallelism from laptops to supercomputers. *SoftwareX*, 1-2:19 – 25, 2015.

[71] Szilard Pall, Mark James Abraham, Carsten Kutzner, Berk Hess, and Erik Lindahl. Tackling exascale software challenges in molecular dynamics simulations with GROMACS. *CoRR*, abs/1506.00716, 2015.

[72] Pronk S.and Pall S., Schulz R., Larsson P., Bjelkmar P., Apostolov R., Shirts M. R., Smith J. C., Kasson P. M., van der Spoel D., Hess B., and Lindahl E. Gromacs 4.5: A high-throughput and highly parallel open source molecular simulation toolkit. *Bioinformatics*, 29:845, 2013.

[73] Berk Hess, Carsten Kutzner, David van der Spoel, and Erik Lindahl. Gromacs 4: algorithms for highly efficient, load-balanced, and scalable

molecular simulation. *Journal of Chemical Theory and Computation*, 4(3):435–447, 2008. PMID: 26620784.

[74] David Van Der Spoel, Erik Lindahl, Berk Hess, Gerrit Groenhof, Alan E. Mark, and Herman J. C. Berendsen. Gromacs: Fast, flexible, and free. *Journal of Computational Chemistry*, 26(16):1701–1718, 2005.

[75] E Lindahl, B Hess, and D van der Spoel. Gromacs 3.0: a package for molecular simulation and trajectory analysis. *JOURNAL OF MOLECULAR MODELING*, 7(8):306–317, 2001. Addresses: van der Spoel D, Uppsala Univ, Dept Biochem, Husargatan 3, Box 576, S-75123 Uppsala, Sweden. Uppsala Univ, Dept Biochem, S-75123 Uppsala, Sweden. KTH, S-10044 Stockholm, Sweden. Univ Groningen, Dept Biophys Chem, NL-9747 AG Groningen, Netherlan.

[76] Siewert J. Marrink, H. Jelger Risselada, Serge Yefimov, D. Peter Tieleman, and Alex H. de Vries. The martini force field: coarse grained model for biomolecular simulations. *The Journal of Physical Chemistry B*, 111(27):7812–7824, 2007. PMID: 17569554.

[77] W. M. Brown, P. Wang, S. J. Plimpton, and A. N. Tharrington. Implementing molecular dynamics on hybrid high performance computers - short range forces. *Comp. Phys. Comm.*, 182:898–911, 2011.

[78] W. M. Brown, P. Wang, S. J. Plimpton, A. N. Tharrington, and A. Kohlmeyer. Implementing molecular dynamics on hybrid high performance computers - particle-particle particle-mesh. *Comp. Phys. Comm.*, 183:449–459, 2012.

[79] W. M. Brown and Y. Masako. Implementing molecular dynamics on hybrid high performance computers – three-body potentials. *Comp. Phys. Comm.*, 184:2785–2793, 2013.

[80] Patrick S. Doyle, Eric S.G. Shaqfeh, Gareth H. McKinley, and Stephen H. Spiegelberg. Relaxation of dilute polymer solutions following extensional flow1dedicated to the memory of professor gianni astarita.1. *Journal of Non-Newtonian Fluid Mechanics*, 76(1):79 – 110, 1998.

[81] P. Grassia and E. J. Hinch. Computer simulations of polymer chain relaxation via brownian motion. *Journal of Fluid Mechanics*, 308:255–288, 1996.

[82] PATRICK S. DOYLE, ERIC S. G. SHAQFEH, and ALICE P. GAST. Dynamic simulation of freely draining flexible polymers in steady linear flows. *Journal of Fluid Mechanics*, 334:251–291, 1997.

[83] J.M. Rallison. Dissipative stresses in dilute polymer solutions. *Journal of Non-Newtonian Fluid Mechanics*, 68(1):61 – 83, 1997.

[84] P.-G. de Gennes. Entangled polymers. *Physics Today*, 36:33–47, June 1983.

[85] P. G. de Gennes. Reptation of a Polymer Chain in the Presence of Fixed Obstacles. , 55:572–579, July 1971.

[86] Masao Doi and S. F. Edwards. Dynamics of concentrated polymer systems. part 1.-brownian motion in the equilibrium state. *J. Chem. Soc., Faraday Trans. 2*, 74:1789–1801, 1978.

[87] S F Edwards. The statistical mechanics of polymerized material. *Proceedings of the Physical Society*, 92(1):9, 1967.

[88] N. Spenley, X. Yuan, and M. Cates. Nonmonotonic Constitutive Laws and the Formation of Shear-Banded Flows. *Journal de Physique II*, 6(4):551–571, 1996.

[89] Jonathan P. Rothstein and Gareth H. McKinley. Inhomogeneous transient uniaxial extensional rheometry. *Journal of Rheology*, 46(6):1419–1443, 2002.

[90] Jonathan P. Rothstein. Transient extensional rheology of wormlike micelle solutions. *Journal of Rheology*, 47(5):1227–1247, 2003.

[91] P. A. Vasquez, G. H. McKinley, and L. P. Cook. A network scission model

for wormlike micellar solutions: I. model formulation and viscometric flow predictions. *J. Non-Newtonian Fluid Mech.*, 144:122, 2007.

[92] V. Entov and E. Hinch. Effect of a spectrum of relaxation times on the capillary thinning of a filament of elastic liquid. *J. Non-Newtonian Fluid Mech.*, 72:31, 1997.

[93] H. Sim, B. Khomami, and R. Sureshkumar. Flow-induced chain scission in dilute polymer solutions: Algorithm development and results for scission dynamics in elongational flow. *J. Rheol. (Melville, NY, U. S.)*, 51:1223, 2007.

[94] A. Groisman and V. Steinberg. Elastic turbulence in a polymer solution flow. *Nature*, 405:53, 2000.

[95] S. J. Haward, T. J. Ober, M. S. Oliveira, M. A. Alves, and G. H. McKinley. Extensional rheology and elastic instabilities of a wormlike micellar solution in a microfluidic cross-slot device. *Soft Matter*, 8:536, 2012.

[96] D. Sachsenheimer, C. Oelschlaeger, S. Müller, J. Küstner, S. Bindgen, and N. Willenbacher. Elongational deformation of wormlike micellar solutions. *J. Rheol.*, 58:2017, 2014.

[97] A. Bhardwaj, E. Miller, and J. P. Rothstein. Filament stretching and cap-

illary breakup extensional rheometry measurements of viscoelastic worm-like micelle solutions. *J. Rheol. (Melville, NY, U. S.)*, 51:693, 2007.

[98] P. S. Doyle, E. S. Shaqfeh, G. H. McKinley, and S. H. Spiegelberg. Relaxation of dilute polymer solutions following extensional flow. *J. Non-Newtonian Fluid Mech.*, 76:79, 1998.

[99] A. Noy and R. Golestanian. Length scale dependence of dna mechanical properties. *Phys. Rev. Lett.*, 109:228101, 2012.

[100] E. Hinch. Uncoiling a polymer molecule in a strong extensional flow. *J. Non-Newtonian Fluid Mech.*, 54:209, 1994.

[101] P. De Gennes. Coil-stretch transition of dilute flexible polymers under ultrahigh velocity gradients. *J. Chem. Phys.*, 60:5030, 1974.

[102] D. E. Smith and S. Chu. Response of flexible polymers to a sudden elongational flow. *Science*, 281:1335, 1998.

[103] R. Larson, H. Hu, D. Smith, and S. Chu. Brownian dynamics simulations of a dna molecule in an extensional flow field. *J. Rheol. (Melville, NY, U. S.)*, 43:267, 1999.

[104] C. M. Schroeder, H. P. Babcock, E. S. Shaqfeh, and S. Chu. Observation of polymer conformation hysteresis in extensional flow. *Science*, 301:1515, 2003.

[105] C. M. Schroeder, E. S. Shaqfeh, and S. Chu. Effect of hydrodynamic interactions on dna dynamics in extensional flow: Simulation and single molecule experiment. *Macromolecules*, 37:9242, 2004.

[106] T. Sridhar, D. Nguyen, R. Prabhakar, and J. R. Prakash. Rheological observation of glassy dynamics of dilute polymer solutions near the coil-stretch transition in elongational flows. *Phys. Rev. Lett.*, 98:167801, 2007.

[107] T. T. Perkins, D. E. Smith, and S. Chu. Single polymer dynamics in an elongational flow. *Science*, 276:2016, 1997.

[108] R. M. Elder and A. Jayaraman. Role of structure and dynamics of dna with cisplatin and oxaliplatin adducts in various sequence contexts on binding of hmgb1a. *Mol. Simul.*, 38:793, 2012.

[109] T. Odijk. Stiff chains and filaments under tension. *Macromolecules*, 28:7016, 1995.

[110] J. F. Marko and E. D. Siggia. Stretching dna. *Macromolecules*, 28:8759, 1995.

[111] H. J. C. Berendsen, D. Van Der Spoel, and R. Van Drunen. *Comp. Phys. Comm*, 91:43–56, 1995.

[112] Mark James Abraham, Teemu Murtola, Roland Schulz, Szilard Pall,

Jeremy C. Smith, Berk Hess, and Erik Lindahl. *SoftwareX*, 1-2:19 – 25, 2015.

[113] Szilard Pall, Mark James Abraham, Carsten Kutzner, Berk Hess, and Erik Lindahl. *CoRR*, abs/1506.00716, 2015.

[114] Pronk S.and Pall S., Schulz R., Larsson P., Bjelkmar P., Apostolov R., Shirts M. R., Smith J. C., Kasson P. M., van der Spoel D., Hess B., and Lindahl E. *Bioinformatics*, 29:845, 2013.

[115] Berk Hess, Carsten Kutzner, David van der Spoel, and Erik Lindahl. *Journal of Chemical Theory and Computation*, 4(3):435–447, 2008. PMID: 26620784.

[116] David Van Der Spoel, Erik Lindahl, Berk Hess, Gerrit Groenhof, Alan E. Mark, and Herman J. C. Berendsen. *Journal of Computational Chemistry*, 26(16):1701–1718, 2005.

[117] E Lindahl, B Hess, and D van der Spoel. *JOURNAL OF MOLECULAR MODELING*, 7(8):306–317, 2001. Addresses: van der Spoel D, Uppsala Univ, Dept Biochem, Husargatan 3, Box 576, S-75123 Uppsala, Sweden. Uppsala Univ, Dept Biochem, S-75123 Uppsala, Sweden. KTH, S-10044 Stockholm, Sweden. Univ Groningen, Dept Biophys Chem, NL-9747 AG Groningen, Netherlan.

[118] P. A. Vasquez, G. H. McKinley, and L. P. Cook. *J. Non-Newtonian Fluid Mech.*, 144:122, 2007.

[119] V. Entov and E. Hinch. *J. Non-Newtonian Fluid Mech.*, 72:31, 1997.

[120] H. Sim, B. Khomami, and R. Sureshkumar. *J. Rheol. (Melville, NY, U. S.)*, 51:1223, 2007.

[121] A. Groisman and V. Steinberg. *Nature*, 405:53, 2000.

[122] S. J. Haward, T. J. Ober, M. S. Oliveira, M. A. Alves, and G. H. McKinley. *Soft Matter*, 8:536, 2012.

[123] D. Sachsenheimer, C. Oelschlaeger, S. Müller, J. Küstner, S. Bindgen, and N. Willenbacher. *J. Rheol.*, 58:2017, 2014.

[124] A. Bhardwaj, E. Miller, and J. P. Rothstein. *J. Rheol. (Melville, NY, U. S.)*, 51:693, 2007.

[125] P. S. Doyle, E. S. Shaqfeh, G. H. McKinley, and S. H. Spiegelberg. *J. Non-Newtonian Fluid Mech.*, 76:79, 1998.

[126] E. Hinch. *J. Non-Newtonian Fluid Mech.*, 54:209, 1994.

[127] P. De Gennes. *J. Chem. Phys.*, 60:5030, 1974.

[128] D. E. Smith and S. Chu. *Science*, 281:1335, 1998.

[129] R. Larson, H. Hu, D. Smith, and S. Chu. *J. Rheol. (Melville, NY, U. S.)*, 43:267, 1999.

[130] C. M. Schroeder, H. P. Babcock, E. S. Shaqfeh, and S. Chu. *Science*, 301:1515, 2003.

[131] T. Sridhar, D. Nguyen, R. Prabhakar, and J. R. Prakash. *Phys. Rev. Lett.*, 98:167801, 2007.

[132] T. T. Perkins, D. E. Smith, and S. Chu. *Science*, 276:2016, 1997.

[133] R. M. Elder and A. Jayaraman. *Mol. Simul.*, 38:793, 2012.

[134] T. Odijk. *Macromolecules*, 28:7016, 1995.

[135] J. F. Marko and E. D. Siggia. *Macromolecules*, 28:8759, 1995.

[136] D. Danino, Y. Talmon, H. Levy, G. Beinert, and R. Zana. *Science*, 269:1420, 1995.

[137] H. J. C. Berendsen, D. Van Der Spoel, and R. Van Drunen. *Comp. Phys. Comm*, 91:43–56, 1995.

[138] Mark James Abraham, Teemu Murtola, Roland Schulz, Szilard Pall, Jeremy C. Smith, Berk Hess, and Erik Lindahl. *SoftwareX*, 1-2:19 – 25, 2015.

[139] Szilard Pall, Mark James Abraham, Carsten Kutzner, Berk Hess, and Erik Lindahl. *CoRR*, abs/1506.00716, 2015.

[140] Pronk S.and Pall S., Schulz R., Larsson P., Bjelkmar P., Apostolov R., Shirts M. R., Smith J. C., Kasson P. M., van der Spoel D., Hess B., and Lindahl E. *Bioinformatics*, 29:845, 2013.

[141] Berk Hess, Carsten Kutzner, David van der Spoel, and Erik Lindahl. *Journal of Chemical Theory and Computation*, 4(3):435–447, 2008. PMID: 26620784.

[142] David Van Der Spoel, Erik Lindahl, Berk Hess, Gerrit Groenhof, Alan E. Mark, and Herman J. C. Berendsen. *Journal of Computational Chemistry*, 26(16):1701–1718, 2005.

[143] E Lindahl, B Hess, and D van der Spoel. *JOURNAL OF MOLECULAR MODELING*, 7(8):306–317, 2001. Addresses: van der Spoel D, Uppsala Univ, Dept Biochem, Husargatan 3, Box 576, S-75123 Uppsala, Sweden. Uppsala Univ, Dept Biochem, S-75123 Uppsala, Sweden. KTH, S-10044 Stockholm, Sweden. Univ Groningen, Dept Biophys Chem, NL-9747 AG Groningen, Netherlan.

[144] Subas Dhakal and Radhakrishna Sureshkumar. Anomalous diffusion and stress relaxation in surfactant micelles. *Phys. Rev. E*, 96:012605, Jul 2017.

Kelechi Berquist

Washington DC Metro Area | 267-243-6341 | kelechi@berquist.tech | https://github.com/KelechiBerquist |
http://evimeria.tk/ | https://www.linkedin.com/in/kelechi-okoroafor/

Skills & Competences

Javascript, MongoDB, Node.JS, Express.JS, HTML5, CSS3, Mongoose, C++, Python, Git, Cloud Computing (AWS, Digital Ocean), Bootstrap, Semantic UI, Linux OS, Matlab, Teaching, Data Analysis, Mentorship, Leadership, Objectivity and Big-picture thinking.

Experience

Complex Fluids Research Assistant   **August 2014 – August 2018**
Department of Biomedical and Chemical Engineering   *SYRACUSE UNIVERSITY*

- Conceived project to obtain data-driven recommendations for micellar structure in nanocarrier drug delivery application
- Identified molecular models and simulation packages that most efficiently used available computational resources
- Utilized Ubuntu Linux based Infrastructure-as-a-service (IaaS) and Platform-as-a-service (PaaS) cloud computing instances with GPU, CPU and multi-processing (OpenMP) capabilities
- Used C++ and Python to develop simulation scripts for LAMMPS and GROMACS molecular dynamics simulation packages
- Modelled and simulated nanoscale surfactant systems to investigate their structural and dynamic response to uniaxial extensional flow
- Generated hundreds of gigabytes of simulation data using molecular simulations then processed the data and performed scientific analysis and calculations to compute rheological properties using self-developed C++ and Python programs
- Analysis of micellar structures identified an optimal structure that minimized risk of constriction-induced premature drug release by ~87% on average
- Presented data and conclusions using self-developed Python scripts through libraries such as SciPy, Numpy and Matplotlib

Fluid Mechanics Teaching Assistant   **Fall 2015, Fall 2017**
Department of Biomedical and Chemical Engineering   *SYRACUSE UNIVERSITY*

- Assisted and facilitated the instruction of courses with class sizes of approximately 80 students
- Hosted over 6hrs of weekly office hours with average attendance of over 80%
- Graded and evaluated student performance and understanding of the subject matter
- Kept track of student attendance and participation and reached out to under-performing students
- Rendered additional assistance to boost student performance and mitigate risk of college drop-out
- Went above and beyond job description to hold office hours and exam review on demand to better support and assist students

Research Assistant   **August 2013 – August 2014**
Department of Chemical Engineering   *UNIVERSITY OF PENNSYLVANIA*

- Studied oxygen conductivity in Yttria-stabilised-Zirconia (YSZ) perovskite membranes with the aim of developing an environmentally friendly method of producing hydrogen gas for fuel cell applications
- Synthesized YSZ perovskite fuel cell membranes
- Performed oxygen-conductivity tests on the synthesized membranes
- Analysed data for observable trends in oxygen conductivity with variation in composition and synthesis
- Presented graphical visualization of trends from analysis using Octave

Auditor   **November 2011 – October 2012**
Operations Support Department   *Exxon Mobil*
- Monitored daily records of company production, expenditure and assets worth over $1M at off-shore and on-shore platforms
- Identified individual platform threshold beyond which discrepancies in production records were flagged as potentially erroneous or fraudulent
- Performed quarterly reconciliation of production records

Operations Manager   *October 2010 – October 2011*
Ackinu Services
- Coordinated daily activities of the organization
- Planned and executed humanitarian projects to generate optimal results with available resources
- Assisted under-privileged students in successfully completing mandatory regional examinations by providing educational and financial resources
- Identified methods and developed programs that optimised resources and reduced redundancy in project time and resources

Project
HTTP://EVIMERIA.TK/
- Registered domain name and configured a Platform-as-a-service cloud computing instance on amazon web service.
- Photo blog, to-do list, weather and stock market web applications were developed and hosted using front-end (Javascript, HTML5, CSS3, jquery, Bootstrap) and back end (Javascript, Mongodb, Mongoose, Express.js, Node.js) tools.
- Get, post, put, delete routes for creating, viewing, editing and deleting documents on the database were done in compliance with RESTful web routing
- Express.JS web development framework was used. Node.JS was used for JavaScript runtime execution. Node package manager (NPM) was used to install and track packages used in the deployment of this project.

Education
- **PHD Chemical Engineering**   Syracuse University, Syracuse NY   August 2018
- **Masters Chemical Engineering**   University of Pennsylvania, Philadelphia, PA   August 2014
- **Bachelors Petroleum Engineering**   Federal Unitech Owerri   August 2010

Courses and Certification
- **Algorithms and Data Structures**   Ongoing
- **Machine Learning**   Ongoing
- **DAT101x: Data Science Orientation**   Completed
- **DAT201x: Querying with Transact-SQL**   Completed
- **The Web Developer Bootcamp**   Completed

Awards
- **Phi Beta Delta International Scholarship Award**   2015-2018
- **President's Fellowship**   2014-2016
- **Exxon/Esso Scholarship**   2012-2014
- **Shell National Merit Award**   2006-2010